



**INTEGRATION OF GROUND PENETRATING RADAR,
2D ELECTRICAL RESISTIVITY AND MAGNETICS
METHODS FOR MAPPING BURIED UTILITIES.**

A BSc. PROJECT

BY

BIODUN-HERBERT ADEYEMI

MATRICULATION NUMBER:

16010401008

IN PARTIAL FULFILLMENT FOR THE AWARD
OF BSc. DEGREE IN GEOPHYSICS
DEPARTMENT OF GEOSCIENCE
MOUNTAIN TOP UNIVERSITY.

CERTIFICATION

I hereby certify that this project titled, **INTEGRATION OF GROUND PENETRATING RADAR, 2D ELECTRICAL RESISTIVITY AND MAGNETIC METHODS FOR MAPPING BURIED UTILITIES**, was prepared and submitted by **BIODUN-HERBERT ADEYEMI** with matriculation number, **16010401008** in partial fulfilment for the award of **BACHELOR OF SCIENCE IN GEOPHYSICS**, Department of Geosciences is hereby accepted by

PROF. E.A. AYOLABI

Supervisor 1

(Signature and Date)

MR R.P. AKINWALE

Supervisor 2

(Signature and Date)

DR. O.B. BALOGUN

Head of Department

(Signature and Date)

DEDICATION

This project is dedicated to God almighty and Mountain Top University.

ACKNOWLEDGEMENTS

I am most appreciative to almighty God for the gift of life and continuous strength for not only leading me through this project but also for the successful completion of my study. My profound gratitude to the Vice Chancellor Prof. E.A. Ayolabi for his immeasurable effort and support. I also acknowledge the effort of my supervisor, Mr. R.P. Akinwale for his constructive suggestions, understanding, and useful comments. My amiable lecturers, especially Dr. O. Balogun, Dr. J. Adeoye, Mr. M.O. Okunubi, and the technologist, Mr. E. Dayo of the department of Geoscience for the seed you have sown in my life through your lectures and words of wisdom which has helped me so far in my journey in this institution.

I am deeply indebted to many people for their immense contributions in diverse ways towards the successful completion of this research work. My appreciation goes to my irreplaceable parents, Mr. Ayodele Durowaiye & Mrs. Funmilayo Durowaiye, who sacrificed wealth and enjoyable moments of their lives for the sake of my success; I want to thank them for their relentless effort towards ensuring the best education for me and for their moral, financial, spiritual, physical and psychological support in my life. May you live long to eat the fruit of your labour. My gratitude also goes to my mentor, Mr. Diri Ibim, my aunty Mrs. Lola Onamusi, and my elder brother, Biodun – Herbert Olorunfemi for their prayers, understanding and support. Lastly, I would like to thank my friends and colleagues, especially Ezeamalu Chinecherem, Agbonjaru David, Onimsi ThankGod, Omishakin Solomon, Obike Emmanuel, Okunbi Favour, Akpan Enwongobong and every other who helped in making this research work a progress for their prayers and support, and help in one way or the other. God bless them all greatly.

ABSTRACT

Buried utilities of different shapes and sizes are characteristics of built-up areas and carry different materials such as gas, water, waste water, electrical cables and communication cables. This requires careful identification in order not to constitute danger to the life and property when further development is needed. This research was therefore carried out in three selected locations within Mountain Top University to provide information about the location, lateral extent and depth of buried utilities using Ground Penetrating Radar (GPR), 2D Electrical Resistivity Imaging (ERI) and Magnetic methods. Data was acquired at the locations to map four major buried pipes. GPR survey using monostatic antennas with frequencies of 450 Hz and 750 Hz were carried out along three traverses at location 1 and 3, and along six traverses at location 2. 2D ERI data using dipole-dipole array with electrode spacing of 0.1 m was collected along three traverses at all three locations, while magnetics survey at 0.1 m station spacing was carried out along three traverses at location 1 and 3, and along six traverses at location 2. Although, the magnetic response is subtle for the buried plastic pipes; magnetic survey at location 3 indicated a conspicuous magnetic low approximately 2 m wide. The conspicuous magnetic low was interpreted as a geologic structure relating to a buried stream/river channel. Integration of the 2D ERT model sections and radargram show that the depth to the top of the buried pipe in location 1 is approximately 0.2 m, and 0.2 m wide, at location 2, the depth of the buried pipe detected and its lateral extent is approximately 0.16 m and 0.28 m respectively, while, the results obtained at location 3 reveals that pipe 1 and pipe 2 are buried at the depth of 0.31 m and 0.2 m respectively with respective diameters of 0.28 m and 0.25 m. The result of this study further corroborates the fact that the integration of 2D ERT and GPR surveys allows for a better identification of buried utilities.

Keywords: Electrical Resistivity Imaging, GPR, Magnetics, Location, Lateral extent, Radargram.

TABLE OF CONTENTS

Title Page	
CERTIFICATION	i
DEDICATION	ii
ACKNOWLEDGEMENTS	iii
ABSTRACT	iv
LIST OF TABLES	vii
LIST OF FIGURES	viii
CHAPTER ONE	1
INTRODUCTION	1
1.0 Background of Study	1
1.1 Statement of the Problem	3
1.2 Aim and Objectives	4
1.3 Location and Accessibility	4
CHAPTER TWO	6
LITERATURE REVIEW	6
2.0 Review of Previous Works Done	6
2.1 Geology of the study area	8
2.1.1 Regional geology of Benin (Dahomey) Basin	8
2.2 Basic Theories	14
2.2.1 Electrical Resistivity (ER)	14
2.2.2 Ground Penetrating Radar (GPR)	26
2.2.3 Magnetic Methods	32
CHAPTER THREE	41
METHODOLOGY	41
3.1 Data Collection	41
3.1.1 Electrical Resistivity (ER)	41
3.1.2 Ground Penetrating Radar (GPR)	45
3.1.2 Magnetism Methods	48
3.2 Data Processing and Interpretation	51
CHAPTER FOUR	53
RESULTS AND DISCUSSION	53
4.1 Introduction	53

4.2 Electrical Resistivity (ER) Survey	53
4.2 Magnetics Method	63
4.3 Ground Penetrating Radar	73
4.4 Integration of methods	81
CHAPTER FIVE	84
CONCLUSION AND RECOMMENDATION	84
5.1 Conclusion.....	84
5.2 Recommendation.....	85
REFERENCES	86
APPENDIX.....	83

LIST OF TABLES

Table	Page
Table 2.1 Generalized stratigraphic column showing age, lithology, and sequence of the formations and tectonic stage of basin development in the Nigerian sector of the Benin (Dahomey) Basin.	26
Table 2.2 Relative permittivity and EM velocity for selected geologic materials (Daniels, 1995)	42
Table 2.3 Magnetic susceptibility of different materials (Telford, 1990)	52
Table 3.1 Table showing how traverse were established	61

LIST OF FIGURES

Figure	Page
Figure 1.1 Map showing the survey area (inset map of Nigeria showing location of Ogun state within Nigeria). Oyedepo et al, 2013.	20
Figure 2.1 Regional map of the Gulf of Guinea showing the location of Benin (Dahomey) Basin in relation to other basins Olabode et al (2016).	23
Figure 2.2 Geological map of Dahomey Basin in the Nigeria sector and the states located on the basin, Olabode et al (2016).	24
Figure 2.3: The parameters used in defining Resistivity (Reynolds, 2011)	31
Figure 2.4: Current Flow from a Single Surface Electrode (Reynolds, 2011)	32
Figure 2.5: Equipotential and Current lines for a pair of current electrodes A and B on a homogenous half-space (Reynolds, 2011)	32
Figure 2.6 The Generalized form of the Electrode Configuration (Reynolds, 2011)	33
Figure 2.7: Wenner Configuration Array Type (Reynolds, 2011)	36
Figure 2.8 Schlumberger Configuration Array Type (Reynolds, 2011)	36
Figure 2.9 Schematic drawing of a typical reflection ray path from the source (labeled “transmit”) to the receiver (labeled “receive”). The ray is shown reflecting off a horizontal subsurface interface. (Modified from Daniels, 1995)	43

Figure	Page
Figure 2.10 Schematic diagram showing wave behavior at a subsurface interface. Part of the wave is reflected back to the surface, whereas part of the wave is refracted. (Modified from Daniels, 1995)	44
Figure 2.11 Magnetic flux (Telford, 1990)	48
Figure 2.12 Induced and remanent magnetisation denoted by J_r and J_i respectively (Telford, 1990)	50
Figure 3.1 The setup of the SuperSting R8	57
Figure 3.2 Map showing 2D resistivity traverses at Location 1	57
Figure 3.3 Map showing 2D resistivity traverses at Location 2	58
Figure 3.4 Map showing 2D resistivity traverses at Location 3	59
Figure 3.5 MALA Ground Explorer	60
Figure 3.6 Map showing GPR traverses at Location 1	61
Figure 3.7 Map showing GPR traverses at Location 2	62
Figure 3.8 Map showing GPR traverses at Location 3	62
Figure 3.9 ENVI PRO	63
Figure 3.10 Map showing magnetic traverses at Location 1	64
Figure 3.11 Map showing magnetic traverses at Location 2	65

Figure	Page
Figure 3.12 Map showing magnetic traverses at Location 3	65
Figure 3.13: a.) Raw apparent resistivity data, b.) calculated apparent resistivity, and c.) Final resistivity model.	66
Figure 4.1a. Interpreted inverse model resistivity results for traverse 1	69
Figure 4.1b. Interpreted inverse model resistivity results for traverse 2	70
Figure 4.1c Augmented 3D view of the inverted 2D ERT sections at Location 1	70
Figure 4.2a. Interpreted inverse model resistivity results for traverse 1	72
Figure 4.2b. Interpreted inverse model resistivity results for traverse 2	72
Fig 4.2c Augmented 3D view of the inverted 2D ERT sections at Location 2	72
Figure 4.3 Interpreted inverse model resistivity results for traverse 2	74
Figure 4.4a. Interpreted inverse model resistivity results for traverse 2	75
Figure 4.4b. Interpreted inverse model resistivity results for traverse 3	75
Figure 4.4c. Augmented 3D view of the inverted 2D ERT sections for pipe 1 at Location 3.	75
Figure 4.5a. Interpreted inverted 2D ERT for traverse 2 at Pipe 2, Location 3.	76
Figure 4.5b. Interpreted inverted 2D ERT for traverse 3 at Pipe 2, Location 3.	76

Figure	Page
Figure 4.5c. Augmented 3D view of the inverted 2D ERT sections for pipe 2 at Location 3.	77
Figure 4.6(a)i. Total magnetic intensity (TMI) plot for profile 1.	79
Figure 4.6(a)ii. IGRF corrected TMI plot for profile 1.	79
Figure 4.6(b)i. Total magnetic intensity (TMI) plot for profile 2.	80
Figure 4.6(b)ii. IGRF corrected TMI plot for profile 2.	80
Figure 4.6(c)i. Total magnetic intensity (TMI) plot for profile 3.	81
Figure 4.6(c)ii. IGRF corrected TMI plot for profile 3.	81
Figure 4.7(a)i. Total magnetic intensity (TMI) plot for profile 1.	82
Figure 4.7(a)ii. IGRF corrected TMI plot for profile 1.	82
Figure 4.7(b)i. Total magnetic intensity (TMI) plot for profile 2	83
Figure 4.7(b)ii. IGRF corrected TMI plot for profile 2.	83
Figure 4.7(c)ii. IGRF corrected TMI plot for profile 4.	84
Figure 4.7(c)i. Total magnetic intensity (TMI) plot for profile 4	84
Figure 4.8(a)i. Total magnetic intensity (TMI) plot for profile 1	85
Figure 4.8(a)ii. IGRF corrected TMI plot for profile 1.	86
Figure 4.8(b)i. Total magnetic intensity (TMI) plot for profile 2	86

Figure	Page
Figure 4.8(b)ii. IGRF corrected TMI plot for profile 2.	87
Figure 4.9a Interpreted GPR radargram using the 450 MHz antenna along traverse 1 at Location 1.	89
Figure 4.9b Augmented 3D view of the GPR radargram for Location 1.	89
Figure 4.9c Interpreted 3D GPR (i) volume and (ii) dip lines at Location 1	90
Figure 4.9d 3D GPR Time slice for Location 1.	90
Figure 4.10a Interpreted GPR radargram using the 450 MHz antenna along traverse 1 at Location 2.	91
Figure 4.10b Augmented 3D view of the GPR radargram for Location 2	92
Figure 4.10c Interpreted 3D GPR (i) volume and (ii) dip lines at Location 2	92
Figure 4.10d 3D GPR Time slice for Location 2.	93
Figure 4.11a Interpreted GPR radargram using the 450 MHz antenna along traverse 1 at Location 3.	94
Figure 4.11b Augmented 3D view of the GPR radargram for Location 3	94
Figure 4.11c Interpreted 3D GPR (i) volume and (ii) dip lines at Location 2	95
Figure 4.11d 3D GPR Time slice for pipe 2, Location 2.	95

Figure	Page
Figure 4.12 A comparison of interpreted results of a.) the final resistivity model and b.) 450 MHz GPR antenna for traverse 1 at Location 1.	96
Figure 4.12 A comparison of interpreted results of a.) the final resistivity model and b.) 450 MHz GPR antenna for traverse 1 at Location 2.	97
Figure 4.13 A comparison of interpreted results of a.) the final resistivity model for pipe 1 b.) the final resistivity model for pipe 2 and c.) 450 MHz GPR antenna for traverse 1 at Location 3.	98

CHAPTER ONE

INTRODUCTION

1.0 Background of Study

The importance of identifying buried utilities cannot be over emphasized as its neglect can cause a lot of problems (Ganiyu et al 2020). Lives can be lost because of metal coming in contact with an electric cable. Utilities could be damaged during construction and renovation, which leads to unnecessary waste of time in repairing or replacing them. The preservation and maintenance of buried utilities in an urban landscape are fundamentally important if modern living is to be preserved. Failure to maintain these buried utilities can rapidly result in the breakdown of the service the utilities provide. This problem stems from the inability to precisely locate buried utilities within the earth subsurface without some form of excavation (Ganiyu et al 2020).

Excavation of land will be the ideal method to locate, repair, or replace damaged buried utilities. However, once the land is excavated, it cannot be returned back to its original state. Hence, this method of accessing buried utilities within the earth subsurface is environmentally unfriendly. This method aside from being environmentally unfriendly and not practicable in all sites are also tedious and suffer from different limitation due to waste of time and project cost efficiency (Hazreek et al. 2016).

Thus, there is a need to adopt a non-invasive alternative method to delineate buried utilities. Buried utilities must be located before repair and replacement work. The integration of geophysical methods in engineering site investigation is considered the best method of locating subsurface structures (Cardarelli et al. 2010, 2014; Bharti et al. 2016a; Ungureanu et al. 2017; Pazzi et al. 2018).

Geophysics is a branch of natural science which studies the physical processes and properties of the Earth and its surrounding, using quantitative methods for their analysis. Engineering Geophysics can be described as the application of geophysical methods to the investigation of subsurface materials. Geophysical methods respond to physical properties of the earth such as acoustic impedance (which is a measure of the product of density and velocity), magnetic susceptibility, electrical conductivity, permittivity etc. (Reynold, 2011). These properties when measured produce a recognizable anomaly, which helps to detect subsurface structures.

The successful adoption of geophysical method for detection of buried utilities depends on the ability to reach the target at a particular depth with the appropriate resolution (Cardarelli et al. 2009; Mahato 2018). Furthermore, the integration of more than one method to identify buried structures has resulted in a more precise definitions and interpretation (Cardarelli et al., 2014; Pueyo et al. 2013; Pazzi et al. 2018). The information about subsurface structures is derived through the measurement of contrasts in physical properties (Mochales et al. 2008).

Geophysical methods such as Electrical Resistivity Tomography (ERT) and Ground Penetrating Radar (GPR) provide a non-destructive and on-site method for detection of subsurface structures (Ramirez et al. 1996). The ERT detects and identifies buried structures with varying resistivity values relative to the surrounding soil (Sun et al. 2017); while GPR identifies subsurface electromagnetic properties based on varying dielectric properties of the subsurface structures (Rehman et al. 2016).

The electrical resistivity of a soil depends on several parameters such as soil structure, texture, porosity, mineral fluid contents, degree of water saturation in the rock and soil physical parameters depending on the level of soil solution, temperature, and soil moisture content (Michot 2003; Samouelian et al. 2005; Bharti et al. 2016a; Mishra et al. 2018). On the other hand, the calculated

parameters of GPR (travel time and amplitudes of reflected signals) depend on dielectric constant, magnetic permeability of the medium, and conductivity of the material (Xu et al. 2002) with dielectric constant as the most important subsurface property controlling the signal propagation velocity, the vertical and horizontal resolution, as well as the reflection coefficient (Metwaly 2013; Sagnard and Tarel 2016).

1.1 Statement of Problem

Mountain Top University is a growing private tertiary institution, which may require various renovations, constructions of structures over time. Loss of property, especially buried utilities such as internet fibre cables, water pipes, electrical cables, waste pipes during new construction and renovation are imminent if their locations and depth are not known. Buried electrical cables can also lead to loss of life during excavation besides the waste of time and unnecessary delay arising from damaged buried utilities. Other problems that are inherent when the locations of buried utilities are not known includes lack of plan for future maintenance and replacement and pollution of environment due to damage of waste pipes.

Ground Penetrating Radar, Electrical Resistivity and Magnetism methods are considered the best method in locating buried utility (Cardarelli et al. 2010, 2014; Bharti *et al.* 2016a; Ungureanu et al. 2017; Pazzi *et al.* 2018). This research therefore seeks to provide Mountain Top University with a quality information about some of her buried utilities using geophysical methods such as Ground Penetrating Radar, 2D Electrical Resistivity and Magnetic method. Precise information about the location, size and depth of these buried utilities present at the investigated part of the University will be provided.

1.2 Aim and Objectives

Aim

The aim of this project is to integrate Ground Penetrating Radar, 2D Electrical Resistivity and Magnetic method to provide information about the location, lateral extent and depth of buried utilities for selected part of Mountain Top University.

Objectives

The application of GPR, 2D ERT and Magnetics methods will help achieve the following objectives:

- i. Characterize the earth's subsurface based on the contrast in physical properties such as dielectric, resistivity and magnetic susceptibility within the earth subsurface, presented by the application of geophysical methods.
- ii. Identify the various types of buried utilities
- iii. Delineate the depth and diameter of these buried utilities
- iv. Interpret the various geophysical methods deployed and appraise its application in detecting buried utilities.

1.3 Location and Accessibility

The study area, Mountain Top University is located in Mountain of Fire and Miracle Ministries (MFM) Prayer City, at KM 12, Lagos – Ibadan express way, Ibafo, Ogun State Nigeria with geographic coordinates of Lat. 6° 43' 38.14" N to 6° 43' 52.72" N and Long. 3° 24' 51.89" to 3° 24' 39.35" E (Figure 1). The campus is accessible through the Lagos – Ibadan express way.

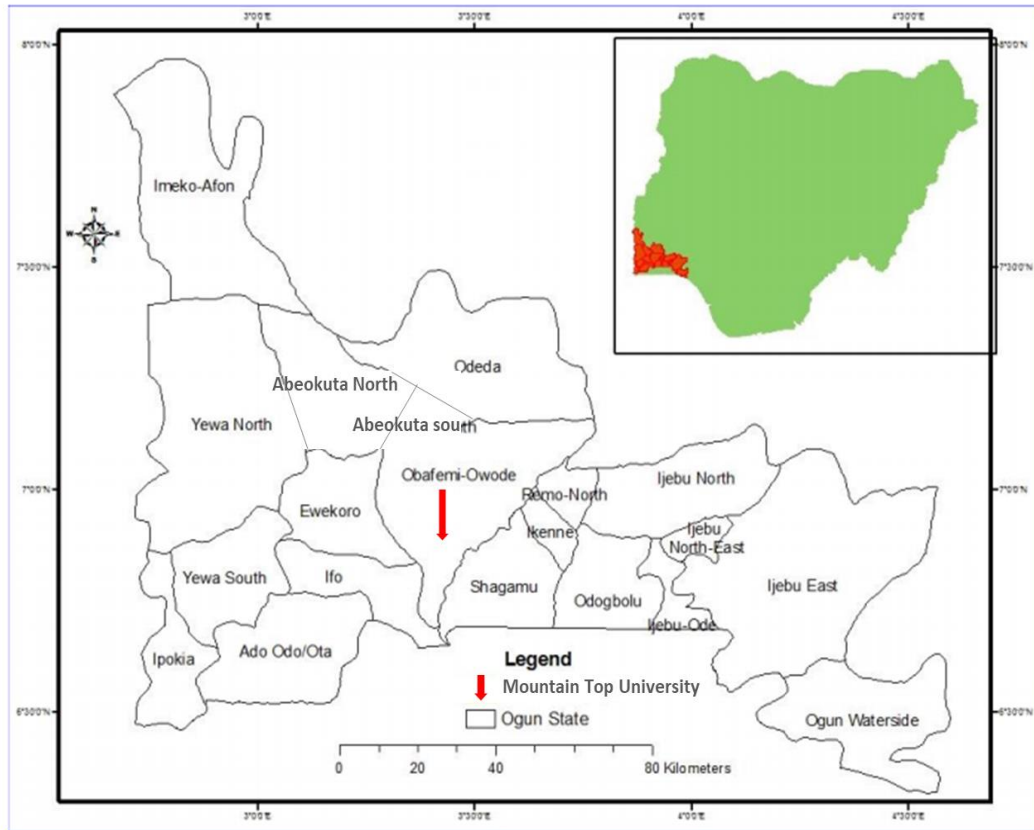


Figure 1.1 Map showing the survey area (inset map of Nigeria showing location of Ogun state within Nigeria). Modified after Oyedepo *et al.*, 2013.

CHAPTER TWO

LITERATURE REVIEW

2.0 Review of Previous Works Done

In the Detection of buried agricultural drainage pipe, Allred *et al.* 2004, tested the ability of four surface geophysical methods which include geomagnetic surveying, electromagnetic induction, resistivity, and ground penetrating radar (GPR). Of these four methods, only GPR was confirmed to be capable of finding agricultural drainage pipe. Consequently, although more research was certainly warranted, the use of ground penetrating radar method in the detection of the agricultural drainage pipe appears to have outstanding potential.

Neal, 2013 used three different Geophysical methods, including electrical resistivity, electromagnetic induction, and ground penetrating radar, to image a known buried stream channel in the Burn Run watershed near Shippensburg University campus in Pennsylvania. Interpretation of the data revealed layers of fill and alluvial deposits above underlying residual clay. When GPR and ER profiles were overlaid, the locations of anomalies were verified.

The study made by Hazreek *et al.*, 2016 was focused on the evaluation of electrical resistivity method (ERM) for buried object detection and its relationship due to the different stiffness of material. This study found that the Electrical Resistivity Value (ERV) of concrete cube for grade 20, 25 and 30 were 170 Ωm , 227 Ωm and 503 Ωm , respectively. Hence, this study shows that the ERV has a strong relationship with different stiffness of material thus applicable to be a useful alternative tool in underground structure detection.

A geophysical study was carried out in Indian Institute of Technology Kanpur, India by Malik *et al.*, 2019, for detecting accurate location, size, depth, and type of subsurface utilities using the ground penetrating radar (GPR) method. After processing and the analyzing the resulting data, it was concluded that there are various hyperbolic reflections due to the presence of underground bodies. The utility pipes are represented the hyperbolics signature which are at a depth of about 30-35 cm, and their orientation on the ground discussed briefly.

Ganiyu *et al.*, 2020, integrated 2D Electrical Resistivity Imaging and Ground Penetrating Radar in the detection of buried utilities in the Federal University of Agriculture, Abeokuta, Nigeria. The goals of the surveys were to determine the effectiveness of the applied methods in detection of buried utilities locations and their depths as well as verification of obtained depths to the top of target by excavation method. Integrated interpretation showed that GPR can effectively provide information about buried utilities compared to ERT.

The integration of more than one method to identify buried structures has resulted in a more precise definitions and interpretation (Cardarelli *et al.*, 2003, 2014; Pueyo *et al.* 2013; Pazzi *et al.* 2018). The information about subsurface structures is derived through the measurement of contrasts in physical variables such as density, soil resistivity, magnetic susceptibility, dielectric properties, etc. (Mochales *et al.*, 2008). Geophysical methods such as Electrical Resistivity Tomography (ERT) and Ground Penetrating Radar (GPR) provide a non-destructive and on-site methods for detection of subsurface structures (Ramirez *et al.*, 1996). The ERT detects and identifies buried structures with varying resistivity values relative to the surrounding soil (Sun *et al.*, 2017); while GPR identifies subsurface electromagnetic properties based on varying dielectric properties of the subsurface structures (Rehman *et al.*, 2016).

2.1 Geology of the study area

2.1.1 Regional geology of Benin (Dahomey) Basin

The Dahomey Basin is a combination of inland/ coastal/ offshore basin that stretches from southern Ghana through Togo and the Republic of Benin to southwestern Nigeria as shown in figure 2.1.

The Nigerian section of the Benin (Dahomey) Basin is located in the southwestern Nigeria covering three different states, namely; Lagos, Ogun and Ondo (Olabode *et al*, 2016) shown in figure 2.2. It is separated from the Niger delta by the Okitipupa ridge.

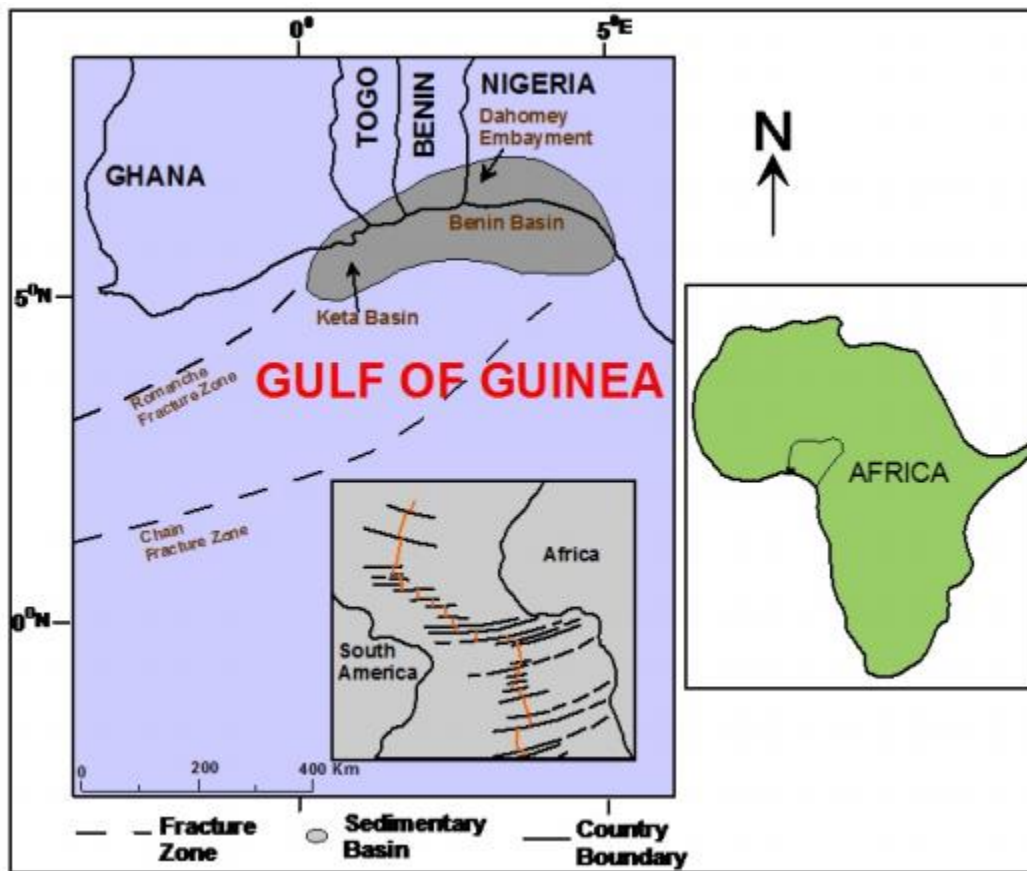


Figure 2.1 Regional map of the Gulf of Guinea showing the location of Benin (Dahomey) Basin in relation to other basins (Olabode *et al*, 2016).

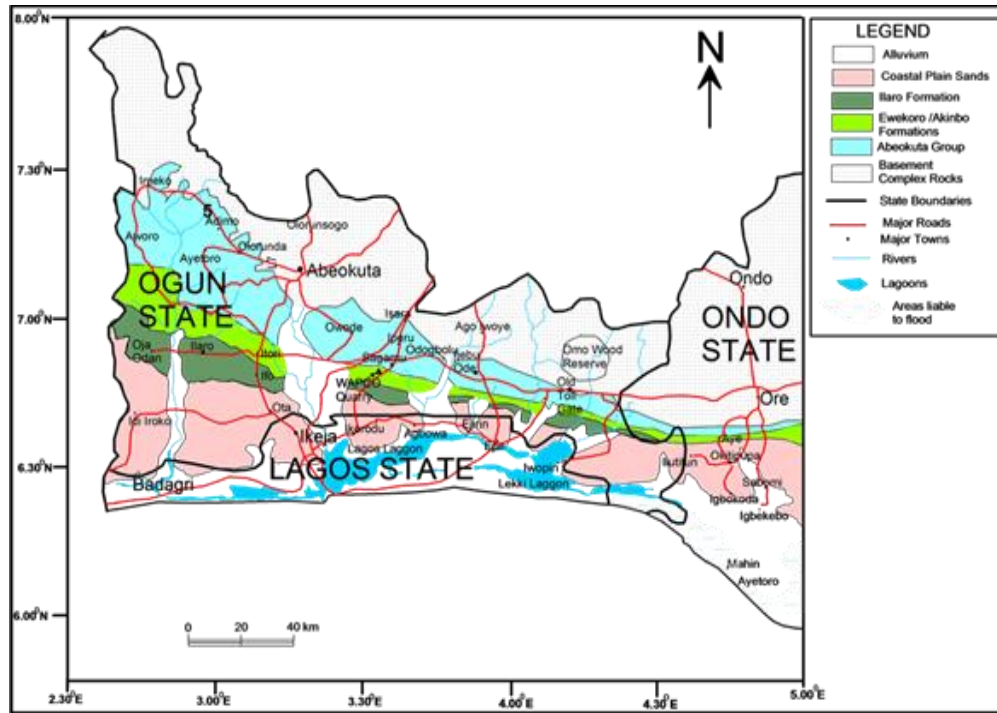


Figure 2.2 Geological map of Dahomey Basin in the Nigeria sector and the states located on the basin, (Olabode *et al*, 2016).

2.1.2 Stratigraphic setting of Benin (Dahomey) Basin

Early study on the basin stratigraphy by Jones & Hockey (1964) recognized both Cretaceous and Tertiary sediments. Other subsequent workers recognized three chronostratigraphic units:

- a) Pre-lower Cretaceous folded sequence,
- b) Cretaceous sequence and
- c) Tertiary sequence (Table 2.1).

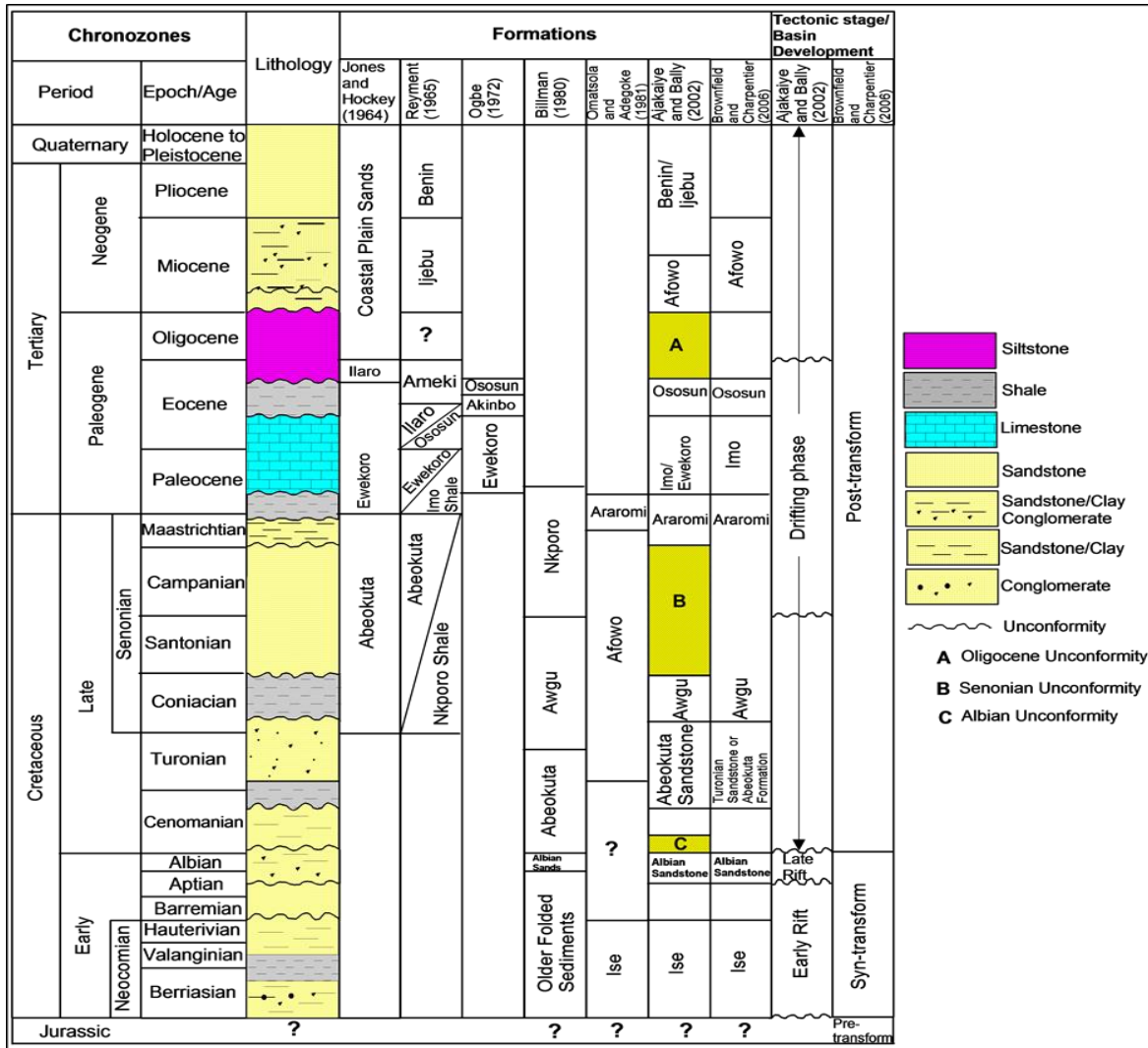
The Cretaceous stratigraphy as compiled from outcrop and borehole records consists Abeokuta Group sub-divided into three informal formational units namely Ise, Afowo and Araromi, Omatsola & Adegoke (1981). Olabode (2016) described the formations as follows; Ise Formation unconformably overlies the basement complex and comprises coarse conglomeratic sediments. Afowo Formation is composed of transitional to marine sands and sandstone with variable but thick interbedded shales and siltstone. Araromi is the uppermost formation and is made up of shales and siltstone with interbeds of limestone and sands (Table 2.1). The Tertiary sediments consist of Ewekoro, Akinbo, Oshosun, Ilaro and Benin (Coastal Plain Sands) Formations (Table 2.1).

The Ewekoro Formation is made up of fossiliferous well bedded limestone while Akinbo and Oshosun Formations are made up of flaggy grey and black shales. Glauconitic rock bands and phosphatic beds define the boundary between Ewekoro and Akinbo Formations. Ilaro and Benin Formations are predominantly coarse sandy estuarine, deltaic and continental beds.

A lot of controversy exists between the stratigraphy of the Cretaceous and Tertiary Formations in the Nigerian sector of the basin. This is due primarily to different stratigraphic names that have been proposed for the same Formation in different localities in the basin (Billman, 1992 & Coker,

2002). This situation can be fairly blamed on the lack of good borehole coverage and adequate outcrops for detailed stratigraphic studies.

Table 2.1 Generalized stratigraphic column showing age, lithology, and sequence of the formations and tectonic stage of basin development in the Nigerian sector of the Benin (Dahomey) Basin. (Olabode *et al*, 2016).



Jones & Hockey (1964) established the name Abeokuta Formation for the mainly arenaceous strata with mudstone, silt, clay and shale interbeds that crop out onshore. Billman (1976) subdivided the Abeokuta Formation into three lithostratigraphic units: The “Unnamed Older Folded Sediments”, “Unnamed Albian Sands” and Abeokuta Formation. On the basis of age equivalence, he referred

the remaining Cretaceous strata to the Awgu and Nkporo Shales. Omatsola & Adegoke (1981) disagreed with this nomenclature on two main grounds.

The first of these is that a rule of accepted stratigraphic practice is contravened because when the Abeokuta Formation was subdivided the same name was used for only one part of the succession. The second is that the application of the well-established Anambra Basin names: Nkporo and Awgu Shales to the Dahomey Basin solely on the basis of age is invalid. As a result, they proposed three new lithostratigraphic units, the Ise, Afowo and Araromi Formations, and referred these to the Abeokuta Group. In their classification, the Ise Formation is equivalent to the Unnamed Older Folded Sediments and the Unnamed Albian Sands, the Afowo Formation to the outcropping Abeokuta Formation, and the Araromi Formation to the Awgu and Nkporo Shales. The view that Anambra Basin lithostratigraphic names should not be used in the Dahomey Basin solely on the basis of age was supported by Okosun (1990). Furthermore, it is inappropriate to use the same names for lithostratigraphic units situated in different basins which are both widely separated from each other and have had different geologic history. This is also true if material for comparison of complex lithologic sequences is only present in deep well cores that are not readily available for study. Thus, the strata previously referred to as the Nkporo Shale were renamed Araromi Formation by Okosun (1990). The lithology of Ise and Afowo formations as defined by Omatsola & Adegoke (1981) show a high degree of similarity. Both are essentially sands and sandstones, but the latter contains thick interbeds of shale. This difference is not sufficient to warrant the establishment of separate lithostratigraphic units. The two formations were considered synonymous by Okosun (1990). In that study, it was observed that the Ise, Afowo and Abeokuta formations have similar lithologic and electric log characters.

The uppermost beds of Abeokuta Formation which crop out in the Ijebu-Ode area and in the shallow boreholes, at Itori, Wasimi and Ishaga onshore, consist mainly of fine- to coarsegrained sand and interbeds of shale, mudstone, limestone and silt, Okosun (1990). These lithofacies correlate well with the upper portion of the neostratotype in the Ojo-1 Borehole. studied by Okosun (1990). Although the Afowo Formation contains shale interbeds, Okosun (1990) emphasized that its essentially sandy character qualifies it along with the arenaceous Ise Formation, for inclusion in the Abeokuta Formation which also contains shale interbeds as demonstrated in the neostratotype described by him and as seen also in many surface outcrops. The use of the names Ise and Afowo. Formations was therefore discontinued and replaced by the Abeokuta Formation which has priority of publication and a wider accepted usage. The Abeokuta Formation was defined by Jones & Hockey (1964) to consist of grits, loose sand, sandstone, kaolinitic clay and shale. It was further characterized as usually having a basal conglomerate or a basal ferruginised sandstone, (Obaje, 2009).

2.2 Basic Theories

Various geophysical methods are applied to environmental site investigations. These methods use different principles of physics and mathematics to model geologic strata and subsurface features. Some methods are based on the injection of electrical current into the subsurface in order to observe the flow paths. Other methods use sound waves or propagate electromagnetic waves in the subsurface. All of the methods create anomalies (strong responses above or below the background levels) based on the differing ways that earth materials respond to the propagating signal. Popular geophysical methods used for environmental monitoring include electrical resistivity (transmission of an electrical current), seismic reflection and refraction (transmission of sound), ground penetrating radar (transmission of an electromagnetic signal), electromagnetic induction (transmission an electromagnetic signal), and gravity (measurement of density changes in the subsurface). The specific methods used in this study are discussed in more detail in the following sections.

2.2.1 Electrical Resistivity (ER)

Electrical resistivity is a fundamental and diagnostic physical property that can be determined by a wide variety of techniques, including electromagnetic induction (Kearey *et al*, 2002).

The resistance (R) is proportional to the length (L) of the resistive material and inversely proportional to the cross-sectional area (A); the constant of proportionality is the ‘true’ resistivity (ρ). According to Ohm’s law, the ratio of the potential drop to the applied current (V/I) also defines the resistance (R) of the cylinder and these two expressions can be combined to form the product of a resistance (Ω) and a distance (area/length; meters) as shown in equation (2.0); hence, the unit of resistivity is ohms-meter (Ωm).

$$\rho = \frac{VA}{IL} [\Omega m] \quad (2.0)$$

In the resistivity method, artificially generated electric currents are introduced into the ground and the resulting potential differences are measured at the surface. Deviations from the pattern of potential differences expected from homogenous ground provide information on the form and electrical properties of the subsurface inhomogeneities (Kearey *et al.*, 2002).

The resistivity of a material is defined as the resistance in ohms between the opposite faces of a unit cube of the material. For a conducting cylinder of resistance ∂R , length ∂L and cross-sectional area ∂A (Figure. 2.3), the resistivity (ρ) is given by equation (2.1).

$$\rho = \frac{\partial R \partial A}{\partial L} \quad (2.1)$$

The SI unit of resistivity is ohms-meter (Ωm) and the reciprocal of resistivity is termed conductivity (Siemens per meter ($S m^{-1}$)).

Consider the element of homogenous material shown in Figure 2.4, current (I) is passed through the cylinder causing a potential drop ∂V between the ends of the element. The potential gradient ($\partial V/\partial L$) associated with this current density (j) is represented in equation (2.2):

$$\frac{\partial V}{\partial L} = -\frac{\rho l}{\partial A} = -\rho j \quad (2.2)$$

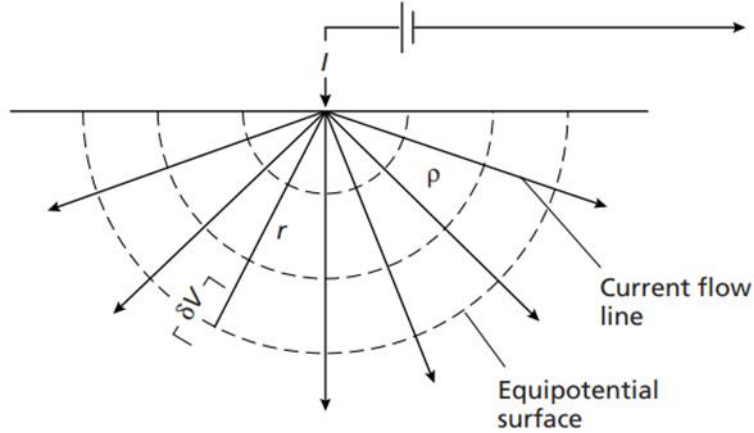


Figure 2.3: The parameters used in defining Resistivity (Kearey *et al.*, 2002)

Where $\partial V/\partial L$ represents the potential gradient through the element in voltm^{-1} and j the current density in Am^{-2} .

Now consider a single current electrode on the surface of a medium of uniform resistivity ρ (Figure 2.4). The circuit is completed by a current sink at a large distance from the electrode. The current flows radially away from the electrode so that the current distribution is uniform over hemispherical shells centred on the source. At a distance from the electrode the shell has a surface area of $2\pi r^2$, so the current density (j) is given by equation (2.3).

$$j = \frac{I}{2\pi r^2} \quad (2.3)$$

From equation (2.2), the potential gradient associated with this current density in equation (2.3) can be written as equation (2.4).

$$\frac{\partial V}{\partial r} = -\rho j = -\frac{\rho I}{2\pi r^2} \quad (2.4)$$

The potential V_r at distance r is then obtained by integration of equation (2.4).

$$V_r = \int \partial V = -\int \frac{\rho I \partial r}{2\pi r^2} = \frac{\rho I}{2\pi r^2} \quad (2.5)$$

The constant of integration is zero since $V_r = 0$ when $r = \infty$. Equation (2.5) allows the calculation of the potential at any point on or below the surface of a homogenous half-space. The hemispherical shells in Figure 2.3. mark surfaces of constant voltage and are termed equipotential surfaces (Kearey et al., 2002). Figure 2.4 shows the flow pattern of the current in a vertical section through ‘tubes’ in a uniform half-space.

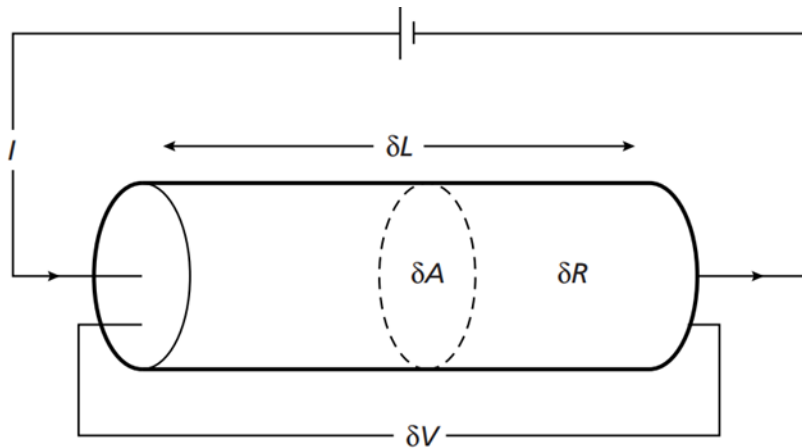


Figure 2.4: Current Flow from a Single Surface Electrode (Kearey *et al.*, 2002)

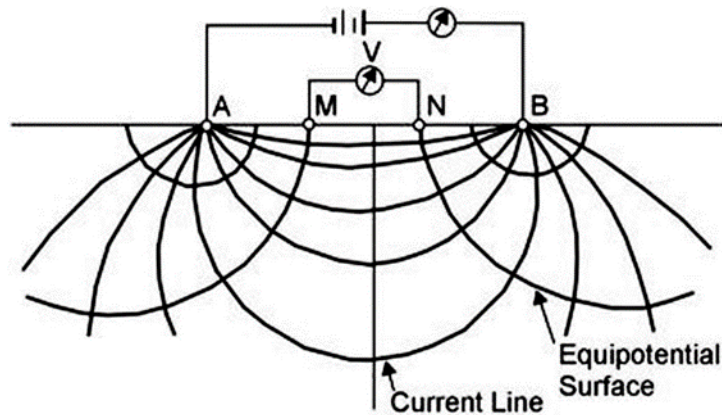


Figure 2.5: Equipotential and Current lines for a pair of current electrodes A and B on a homogenous half-space (Kearey *et al.*, 2002)

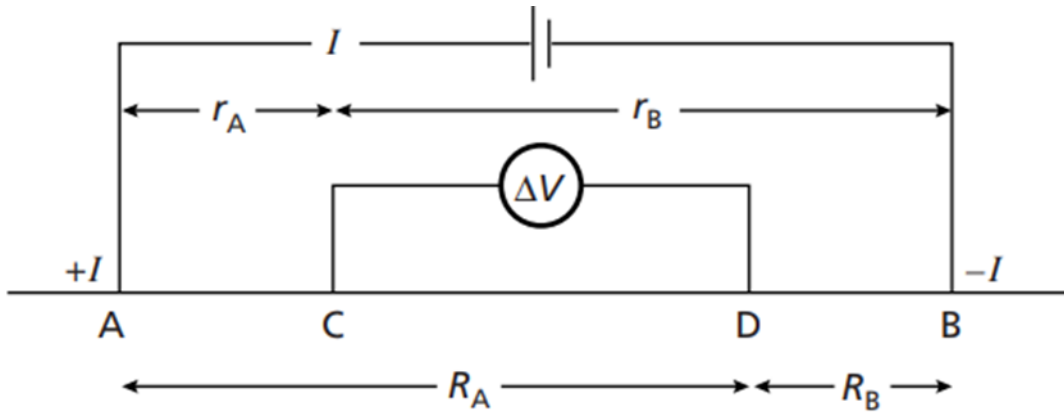


Figure 2.6: The Generalized form of the Electrode Configuration (Kearey *et al.*, 2002)

Geometric factors are not affected by interchanging current and voltage electrodes but voltage electrode spacing are normally kept small to minimize the effects of natural potential.

- i. A and B represents the current electrodes
- ii. C and D represents the potential electrodes
- iii. I represent current
- iv. ΔV represents Potential differences.

The generated form of the electrode configuration used in resistivity measurement was shown in Figure 2.6. V_C , at an internal electrode C, is the sum of the potential contributions V_A and V_B from the current source at A and the sink at B.

$$V_C = \frac{\rho I}{2\pi} \left[\frac{1}{r_A} - \frac{1}{r_B} \right] \quad (2.6)$$

Similarly, also V_D in equation (2.7) is also generated as:

$$V_D = \frac{\rho I}{2\pi} \left[\frac{1}{R_A} - \frac{1}{R_B} \right] \quad (2.7)$$

Absolutely potentials are difficult to monitor so the potential difference ΔV between electrodes C and D is measured as shown in equation (2.8),

$$\Delta V = V_C - V_D = \frac{\rho I}{2\pi} \left\{ \left[\frac{1}{r_A} - \frac{1}{r_B} \right] - \left[\frac{1}{R_A} - \frac{1}{R_B} \right] \right\} \quad (2.8)$$

Thus, equation (2.8) can be written for ρ as stated in equation (2.9),

$$\rho = \frac{2\pi\Delta V}{I \left[\left[\frac{1}{r_B} - \frac{1}{r_B} \right] - \left[\frac{1}{R_A} - \frac{1}{R_B} \right] \right]} \quad (2.9)$$

Where the ground is uniform, the resistivity calculated from equation (2.9) should constant and independent of both electrodes spacing and surface location. When subsurface inhomogeneities exist however, the resistivities will vary with the relative positions of the electrodes. Any computed value is then known as the apparent resistivity ρ_a and will be a function of the form of the inhomogeneity. In effect therefore, depth of current penetration increases with increase in current electrode separation in homogenous layers (Telford *et al.*, 1990).

Electrode Configuration

The electrical resistivity method utilizes different electrode configurations (or arrays) to probe the subsurface and, although several are occasionally employed in specialized surveys, only two are in common use (Kearey *et al.*, 2002). This configuration depends on the mode of arrangement of the current and potential electrodes relative to one another. The various types of electrode configurations include but not limited to Wenner, Schlumberger, Dipole-Dipole, Gradient and Square arrays (Reynolds, 2011).

i. Wenner Electrode Array

In the Wenner configuration (Figure 2.7), the current and potential electrode pairs have a common mid-point and the distances between adjacent electrodes are equal to “a”. Substituting this condition into equation (2.9) generates equation (2.10) as shown as:

$$\rho_a = 2\pi a \frac{\nabla V}{I} \quad (2.10)$$

During Vertical Electrical Sounding (VES), the spacing “a” is gradually increased about a fixed central point and in Constant-separation traversing (CST) the whole spread is moved along a profile with a fixed value of “a”.

- i. C1 and C2 – current electrodes
- ii. P1 and P2 – potential electrodes
- iii. k – Geometric factor
- iv. a – Electrode spacing.

ii. Schlumberger Electrode Array

In the Schlumberger configuration (Figure 2.8), the current and potential pairs of electrodes often also have a common mid-point, but the distances between adjacent electrodes differs. Let parameter “a” represents the distances between one of the current electrodes to the reference point while “b” denotes the distance between two potential electrodes. In substituting the parameter $\left[a - \frac{b}{2}\right]$ and $\left[a + \frac{b}{2}\right]$ into equation (2.9), yields ρ_a as expressed in equation (2.11),

$$\rho_a = \frac{\pi a^2}{b} \left[1 - \frac{b^2}{4a^2}\right] R; a \geq 5b \quad (2.11)$$

- i. C1 and C2 – current electrodes
- ii. P1 and P2 – potential electrodes
- iii. a – Distance of the current electrode spacing to the reference point
- iv. b – Distance between the two potential electrodes.
- v. x – Reference point.

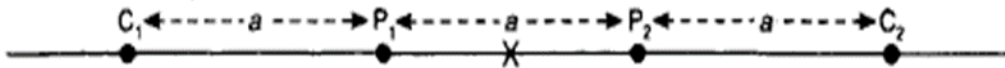


Figure 2.7: Wenner Configuration Array Type (Reynolds, 2011)

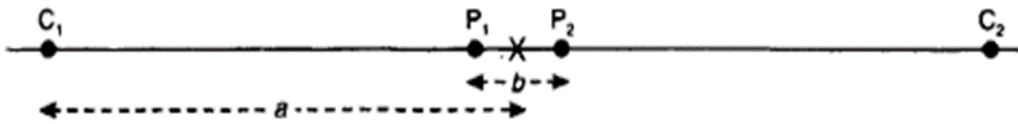


Figure 2.8: Schlumberger Configuration Array Type (Reynolds, 2011)

Factors Affecting Resistivity of Subsurface Materials

The factors affecting earth resistivity include the following:

- i. **Porosity:** The empirical formula developed by Archie (1942) in equation (2.12) for the effective resistivity of a rock formation which takes into account the porosity (ϕ), the fraction(s) of the pores containing water, and the resistivity of the water ρ_w is expressed as:

$$\rho = a\phi^{-m}s^{-n}\rho_w \quad (2.12)$$

Where ρ and ρ_w are the effective rock resistivity, and the resistivity of the pore water, respectively; ϕ is the porosity; s is the volume fraction of pores with water; a , m and n are constants where $0.5 \leq a \leq 2.5$, $1.3 \leq m \leq 2.5$, and $n \approx 2$.

The ratio $\frac{\rho}{\rho_w}$ is known as the Formation factor (F).

- ii. **Permeability:** Archie's relationship notwithstanding, a rock with a non-conducting matrix must be permeable as well as porous to conduct electricity. Permeability (k) has a direct relationship with porosity and logarithmic relationship as shown in equation (2.13) and (2.12) (Olorunfemi and Griffiths, 1985):

$$\phi = aK^b \quad (2.13)$$

$$\text{Log}\phi = \text{Log}a + \text{Log}K \quad (2.14)$$

ϕ = porosity, k = permeability, a and b are constants.

These relationships hold for clean sand and saline water saturated shaly sand. The clean sand shows that the resistivity decreases with increase in permeability while the shaly sand resistivity increases with permeability.

iii. Temperature: The mobility of ion and the viscosity of fluid are affected by temperature.

The lower the viscosity the more mobile the ions become which is caused by higher temperature. Hence, the resistivity becomes lower and the conductivity tend to be higher.

According to Keller and Frischknecht (1966), the resistivity of rock at temperature t is given by the equation (2.15).

$$\rho_t = \frac{\rho_{18}}{1+a(t-18)} \quad (2.15)$$

Where ρ_t = Resistivity of rock at temperature t

ρ_{18} = Resistivity of rock at 18°C

a = Temperature coefficient of resistivity

t = Temperature

iv. Volume and concentration of electrolyte: From the Archie equation Archie (1942) has expressed in equation (2.16),

$$\rho_r = a\varphi^{-m}S^{-n}\rho_w \quad (2.16)$$

S_w is the degree of fluid saturation and ρ_w is the resistivity of fluid.

As the concentration of ions in the electrolyte, ρ_w decreases causing the conductivity to increase in the medium.

- v. **Matrix Resistivity:** If the matrix resistive, the resistivity of the rock itself increases as shown by the equation (2.17) (Patnode and Wyllie, 1950),

$$\frac{1}{\rho_r} = \frac{1}{\rho_m} + \frac{1}{F\rho_w} \quad (2.17)$$

Where ρ_r is the resistivity of rock (bulk), ρ_m is the matrix resistivity, ρ_w is the saturated fluid resistivity and F is the formation factor.

The equation (2.17) is applicable to shaly sand or sandstone.

- vi. **Rock Type:** Resistivity of rocks varies with one rock type to another due to variation in textural type as well as variations in the geological processes that gave rise to the rock.

Vertical Electronic Sounding (VES)

Vertical Electronic Sounding (VES) which is also known as ‘electrical drilling’ or ‘expanding probe’ is one of the simplest and most widely used geophysical method used in mainly in the study of horizontal or near-horizontal interfaces. The current and potential electrodes are maintained at the same relative spacing and the whole spread is progressively expanded about a fixed point (Kearey *et al.*,2002). The technique is extensively used for various geophysical survey such as groundwater exploration by citing a borehole site, determining depth to bedrock, aquifer system, suitable site of landfill, assessing extent of leachate contamination at landfill site etc. (Keller and Frischknecht, 1966)

2D Electrical Resistivity Tomography (ERT)

Electrical Resistivity Tomography (ERT) is a well-established geophysical subsurface-imaging technique for environmental and engineering site investigation, and is routinely applied to the detection of pollution (Daily *et al.*, 1998; Goes and Meekes, 2004), the characterization of geological (Meads *et al.*, 2003) and engineered structure (Daily and Ramirez, 2000), and hydrogeological studies (Binley *et al.*, 2002; Sandberg *et al.*, 2002). This technique employs two current electrodes and potential electrode in measuring the differences in the resistivity of the sub-surface. The advantage of ERT is that it provides a relatively low cost, non-invasive and rapid means of generating spatial models of physical properties of the sub-surface.

Limitations of the Electrical Resistivity Method

- i.** Ambiguity in the interpretation. Thus, there is need for independent geophysical and geological controls to discriminate between valid alternative interpretations of the resistivity data (Kearey *et al.*, 2002).
- ii.** Limitation of interpretation to simple structural configurations. Any deviation from these simple situations may be impossible to interpret.
- iii.** Effects of near-surface resistivity and topography variations can mask the effects of deeper variations (Kearey *et al.*, 2002).
- iv.** Limitation of depth of penetration by the maximum electrical power that can be introduced into the ground and by the physical difficulties of laying out long length of cables (Kearey *et al.*, 2002).

2.2.2 Ground Penetrating Radar (GPR)

Ground penetrating radar (GPR) utilizes propagating electromagnetic (EM) waves that respond to changes in the electromagnetic properties of the shallow subsurface. The propagation velocity of EM waves, which is the principal controlling factor on the generation of reflections, is determined by the relative permittivity contrast between the background material and the target (or the contrast between layers). Relative permittivity is defined as the ability of a material to store and then permit the passage of EM energy when a field is imposed on the material and can be measured in the lab or in situ.

A typical GPR unit consists of a transmitting and receiving antenna, where the transmitting antenna generates an EM pulse that travels into the subsurface and then reflects off an interface or scatters off point sources (both caused by a contrast in relative permittivity). This reflected/scattered energy then travels back to the surface, where it is recorded by the receiving antenna. The time it takes for the wave to travel down to an interface and back up to the surface is called the travel time, and it is used to determine the in-situ propagation velocity of the subsurface material. The velocity (distance/travel time) for an EM wave in Earth's atmosphere at or near sea level is 0.33 m/ns. Because the relative permittivity of all earth materials is greater than the permittivity of air, the velocity of an EM wave in all earth materials will be less than the EM propagation velocity in air—typical materials range between 0.05 and 0.15 m/ns (e.g., Daniels *et al.*, 1995).

Although the propagation velocity of an EM wave is dependent on the relative permittivity of the material, the amplitude and attenuation of a propagating wave is dependent on the magnetic permeability and the electrical conductivity of the material. Magnetic permeability is the ability of the material to become magnetized when an EM field is imposed on the material. As magnetic permeability increases, amplitude attenuation increases; therefore, increased magnetic

permeability results in poorer data quality and/or penetration depth. Electrical conductivity also affects the propagation of EM waves. Materials with a high electrical conductivity tend to attenuate EM signals; therefore, highly conductive materials will produce poor GPR data and/or reduce penetration depth. Table 2.2 shows the expected value ranges of relative permittivity, magnetic susceptibility, and conductivity for different geological materials.

Table 2.2 Relative permittivity and EM velocity for selected geologic materials (Daniels *et al.*, 1995)

Material	ϵ_r ; Davis and Annan (1989)	ϵ_r ; Daniels (1996)	Velocity (m/ns)	Velocity (ft/ns)
Air	1	1	0.3	0.98
Distilled water	80		0.03	0.11
Fresh water	80	81	0.03	0.11
Sea water	80		0.03	0.49–0.57
Fresh water ice	3–4	4	0.15–0.17	0.35–0.49
Sea water ice		4–8	0.11–0.15	0.28–0.35
Snow		8–12	0.09–0.11	0.35–0.50
Permafrost		4–8	0.11–0.16	0.40–0.57
Sand, dry	3–5	4–6	0.12–0.17	0.18–0.31
Sand, wet	20–30	10–30	0.05–0.09	0.57–0.70
Sandstone, dry		2–3	0.17–0.21	0.31–0.44
Sandstone, wet		5–10	0.09–0.13	0.35–0.49
Limestones	4–8		0.11–0.15	0.37
Limestone, dry		7	0.11	0.35
Limestone, wet		8	0.11	0.25–0.44
Shales	5–15		0.08–0.13	0.33–0.40
Shale, wet		6–9	0.10–0.12	0.18–0.44
Silts	3–30		0.05–0.13	0.16–0.44
Clays	5–40		0.05–0.13	0.16–0.44
Clay, dry		2–6	0.12–0.21	0.40–0.70
Clay, wet		15–40	0.05–0.08	0.16–0.25
Soil, sandy dry		4–6	0.12–0.15	0.40–0.49
Soil, sandy wet		15–30	0.05–0.08	0.18–0.25
Soil, loamy dry		4–6	0.05–0.08	0.40–0.49
Soil, loamy wet		15–30	0.07–0.09	0.22–0.31
Soil clayey dry		4–6	0.12–0.15	0.40–0.49
Soil, clayey wet		10–15	0.08–0.09	0.25–0.31
Coal, dry		3.5	0.16	0.53
Coal, wet		8	0.11	0.35
Granites	4–6		0.12–0.15	0.40–0.49
Granite, dry		5	0.13	0.44
Granite, wet		7	0.11	0.37
Salt, dry	5–6	4–7	0.11–0.15	0.37–0.49

A typical reflection schematic is shown in Figure 2.9. The diagram shows a ray path that travels to the interface and reflects back to the surface at the incidence angle. When a wave traveling through the subsurface encounters an object with different electromagnetic properties than the surrounding material, the portion of the wave that hits the object will change direction by a process called scattering.

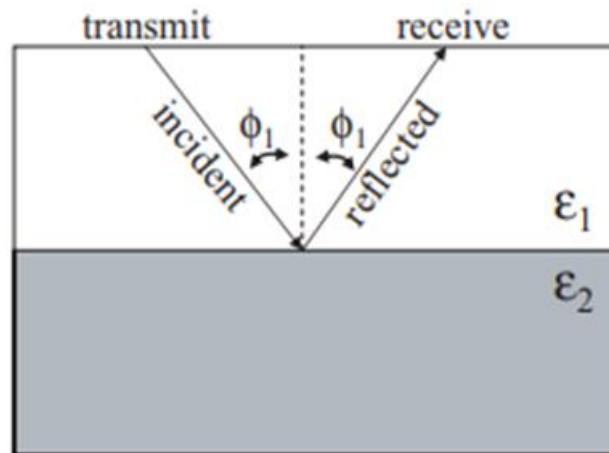


Figure 2.9 Schematic drawing of a typical reflection ray path from the source (labeled “transmit”) to the receiver (labeled “receive”). The ray is shown reflecting off a horizontal subsurface interface. (Modified from Daniels *et al.*, 1995)

There are four main types of scattering:

- i. spectral reflection scattering
- ii. diffraction scattering
- iii. resonant scattering, and
- iv. refraction scattering.

Figure 2.10 shows the basic principle of spectral reflection at a horizontal interface. Spectral reflection scattering is the primary type of scattering targeted in most surveys and is described below. For details on the other types of scattering, see Daniels *et al.*, (1995).

Spectral reflection scattering is based on the law of reflection, where the angle of incidence (angle at which the wave hits the interface) is equal to the angle of reflection (angle at which the wave reflects off the interface). Some energy will not reflect from the interface but will refract through the interface into the underlying medium (as seen in Fig. 2.10). This energy will then travel downward until it encounters another interface layer that has different electromagnetic properties.

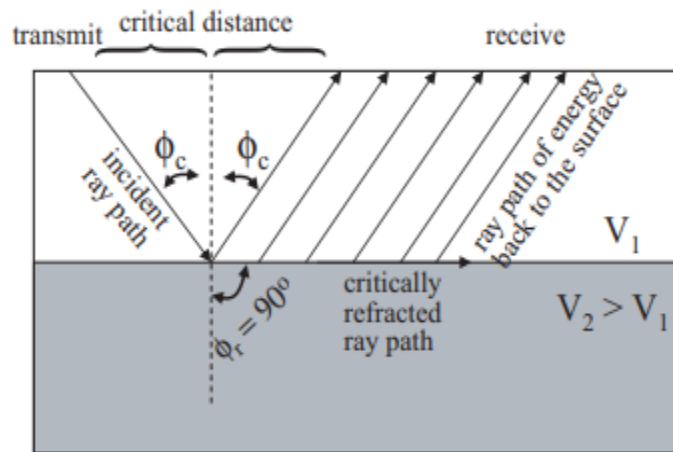


Figure 2.10 Schematic diagram showing wave behavior at a subsurface interface. Part of the wave is reflected back to the surface, whereas part of the wave is refracted. (Modified from Daniels, 1995)

At this second interface, some energy will reflect off the interface and travel back to the surface, and some energy will refract down into the third medium. In this multiple interface case, there will be several reflections in the GPR data as the down-going EM waves encounter each interface. The preceding overview represents the basic knowledge available to nearly all practitioners of GPR. What follows is a more detailed explanation of the critical variables, parameters, and principal equations that dictate how EM waves behave and respond to changes in subsurface electromagnetic properties.

Relative Permeability

The literature pertaining to GPR and EM theory invariably contains the terms dielectric constant (κ), relative permittivity (ϵ_r), dielectric permittivity ($\kappa\epsilon$), and permittivity (ϵ). Dielectric constant, relative permittivity, and dielectric permittivity are equivalent, relative, and dimensionless terms. Permittivity is not equivalent to the previous terms and has the dimensions of Farads per meter (F/m), as described above. A Farad is a measure of charge stored per unit of potential difference and is the Système International d'Unités (SI) unit of capacitance. The terms permittivity, relative permittivity, and dielectric constant are commonly found in physics and electrical engineering literature. The term dielectric permittivity is apparently unique to geophysical literature. Therefore, researchers requiring an indepth discussion of EM theory as it pertains to GPR may encounter some initial confusion regarding the use of these terms when reviewing papers from various other disciplines. To minimize confusion, the term relative permittivity (ϵ_r) rather than dielectric constant or dielectric permittivity will be used herein due to its explicitness and common usage in physics, electrical engineering, and some geophysics texts. Be aware, however, that dielectric permittivity is often the typical term used in GPR publications within geology- or geophysics-centered journals. The real and imaginary components of permittivity are related to relative permittivity via

$$\epsilon_r = \left(\frac{\epsilon'}{\epsilon_0} - i \frac{\epsilon''}{\epsilon_0} \right) \text{ [dimensionless]}, \quad (2.18)$$

Relative permittivity is a critical parameter in GPR studies in that it controls signal propagation velocity and thus wavelength, where wavelength is, of course, critical in determining resolution constraints. For example, material that has low relative permittivity will yield high GPR signal

propagation velocities and, thus, long wavelengths (allowing only lower resolution). This relationship is shown in equations (2.19) and (2.20) and is applicable only for materials with low conductivities and for high-frequency signals (as discussed in later sections):

$$v = \frac{c}{\sqrt{\epsilon_r}} \text{ [m/s]}, \tag{2.19}$$

$$\lambda = \frac{c}{\sqrt{\epsilon_r}} \cdot \frac{1}{f} \text{ [m]}, \tag{2.20}$$

where: v = velocity (m/s)

λ = wavelength (m)

c = speed of light in a vacuum (299,792,458 m/s)

f = frequency (hertz)

2.2.3 Magnetic Methods

Flux density, field strength and permeability

Around a bar magnet, a magnetic flux exists, as indicated by the flux lines in the Figure 2.9, and converges near the ends of the magnet, which are known as the magnetic poles. If such a bar magnet is suspended in free air, the magnet will align itself with the Earth's magnetic field with one pole (the positive north-seeking) pointing towards the Earth's north pole and the other (the negative south-seeking) towards the south magnetic pole. Magnetic poles always exist in pairs of opposite sense to form a dipole. When one pole is sufficiently far removed from the other so that it no longer affects it, the single pole is referred to as a monopole. If two magnetic poles of strength m_1 and m_2 are separated by a distance r , a force exists between them. If the poles are of the same type, the force will repel but will attract if they are of opposite polarity, and will draw the poles towards each other.

$$F = \frac{m_1 m_2}{4\pi\mu r^2} \quad (2.21)$$

The relationship is similar to gravitational or electrical fields i.e., inverse square law where μ is the magnetic permeability of the medium separating the poles; m_1 and m_2 are pole strengths and r the distance between them. The closeness of the flux lines shown in the Figure 2.9, the flux per unit area, is the flux density B (and is measured in weber/m² = teslas). B , which is also called the 'magnetic induction', is a vector quantity.

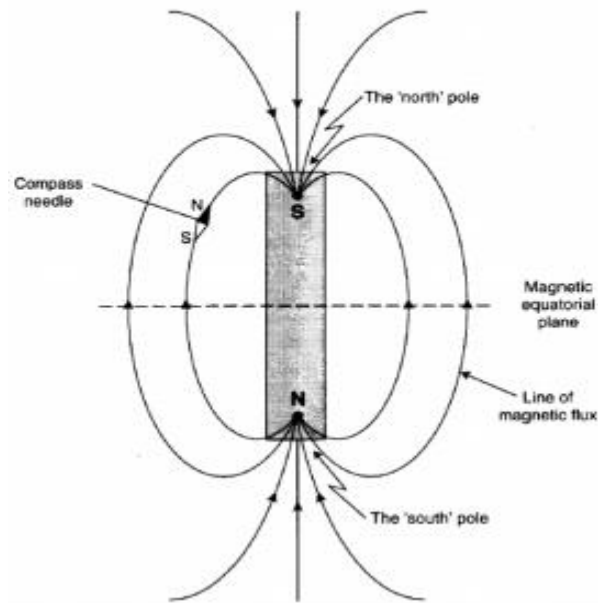


Figure 2.11 Magnetic flux (Telford, 1990)

The magnetic field can also be defined in terms of a force field which is produced by electric currents. This magnetising field strength H is defined, following Biot-Savart's Law, as being the field strength at the centre of a loop of wire of radius r through which a current I is flowing such that $H = I/2r$. Consequently, the units of the magnetising field strength H are amperes per metre (A/m). The ratio of the flux density B to the magnetising field strength H is a constant called the absolute magnetic permeability (μ). Practically, the magnetic permeability of water and air can be taken to be equal to the magnetic permeability of free space (a vacuum), denoted μ_0 which has the value $4\pi \times 10^{-7} \text{ WbA}^{-1}\text{m}^{-1}$. For any medium other than a vacuum, the ratio of the permeabilities of a medium to that of free space is equal to the relative permeability μ_r such that $\mu_r = \mu/\mu_0$ and, as it is a ratio, it has no units. Susceptibility It is possible to express the relationship between B and H in terms of a geologically diagnostic parameter, the magnetic susceptibility κ Susceptibility is in

essence a measure of how susceptible a material is to becoming magnetised. For a vacuum, $\mu_r = 1$ and $\kappa = 0$. Although susceptibility has no units, to rationalise its numerical value to be compatible with the SI or rationalised system of units, the value in c.g.s. equivalent units (e.g., unrationalised units such as e.m.u. - electromagnetic units) should be multiplied by 4π .

Relationship between magnetic flux density B , magnetising force H , and susceptibility κ

Given that $B = \mu H$

Since $\mu = \mu_r \mu_0$

It can be written that, and $B = \mu_r \mu_0 H$

For a vacuum, $\mu_r = 1$ and $\kappa = 0$

Therefore, $\kappa = \mu_r - 1$ and B can be rewritten as

$$B = \mu_0 H + \mu_0 H + \mu_r \mu_0 H$$

$$= \mu_0 H + \mu_0 (\mu_r - 1) H$$

$$= \mu_0 H + \mu_0 k H$$

$$= \mu_0 H + \mu_0 J$$

$$\text{Hence, } B = \mu_0 H (1 + k) \tag{2.22}$$

Induced and remanent magnetisation

In many cases, in the absence of an applied field (H), there is still a measurable intensity of magnetisation which is sustained by the internal field strength due to permanently magnetic particles. The intensity of this permanent or remanent magnetisation is denoted by J_r (Figure 2.12).

A rock mass containing magnetic minerals will have an induced as well as a remanent magnetisation. These magnetisations may have different directions and magnitudes of intensity.

The magnitude and orientation of the resultant J dictate both the amplitude and shape of a magnetic anomaly, respectively.

Consequently, interpretation of magnetic data is complicated by having greater degrees of freedom of the magnetic parameters and physical properties compared with gravity, which is largely dependent upon only rock density.

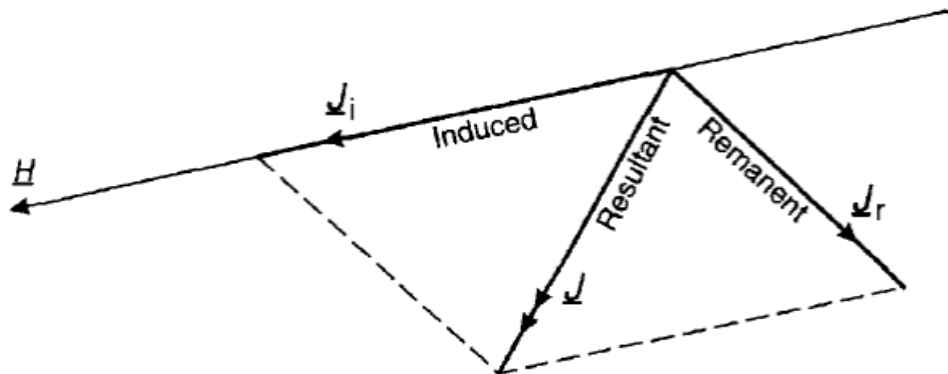


Figure 2.12 Induced and remanent magnetisation denoted by J_r and J_i respectively (Telford, 1990)

Similarities and Differences between magnetic and electric fields:

- i. Like the electric field, the magnetic field is directly proportional to the magnetic force. But unlike E , which is parallel or antiparallel to the electric force, the direction of B is perpendicular to the magnetic force.
- ii. Like E , the magnetic field may be defined through the force experienced by a small test charge, but unlike E , the speed and direction of the test charge must be taken into consideration when relating magnetic forces and fields.
- iii. Because the magnetic force is perpendicular to the velocity at every instant, the component of the force in the direction of the displacement is zero, and the work done by the magnetic field is therefore always zero.

- iv. Whereas electrostatic fields are produced by electric charges, magnetostatic fields are produced by electric currents.

Susceptibility of rocks and minerals

Magnetic susceptibility is an extremely important property of rocks and is to magnetic exploration methods what density is to gravity surveys. Rocks that have a significant concentration of ferro- and/or ferri-magnetic minerals tend to have the highest susceptibilities.

Consequently, basic and ultrabasic rocks have the highest susceptibilities, acid igneous and metamorphic rocks have intermediate to low values, and sedimentary rocks have very small susceptibilities in general.

Metamorphic rocks are dependent upon their parent material. Susceptibilities depend upon the alignment and shape of the magnetic grains dispersed throughout the rock. Table 2.3 shows the different magnetic susceptibility of different materials.

Table 2.3 Magnetic susceptibility of different materials (Telford, 1990)

Mineral or rock type	Susceptibility*
<i>Sedimentary</i>	
Dolomite (pure)	- 12.5 to + 44
Dolomite (impure)	20 000
Limestone	10 to 25 000
Sandstone	0 to 21 000
Shales	60 to 18 600
Average for various	0 to 360
<i>Metamorphic</i>	
Schist	315 to 3000
Slate	0 to 38 000
Gneiss	125 to 25 000
Serpentine	3100 to 75 000
Average for various	0 to 73 000
<i>Igneous</i>	
Granite	10 to 65
Granite (m)	20 to 50 000
Rhyolite	250 to 37 700
Pegmatite	3000 to 75 000
Gabbro	800 to 76 000
Basalts	500 to 182 000
Oceanic basalts	300 to 36 000
Peridotite	95 500 to 196 000
Average for acid igneous	40 to 82 000
Average for basic igneous	550 to 122 000
<i>Minerals</i>	
Ice (d)	- 9
Rocksalt (d)	- 10
Gypsum (d)	- 13
Quartz (d)	- 15
Graphite (d)	- 80 to - 200
Chalcopyrite	400
Pyrite (o)	50 to 5000
Hematite (o)	420 to 38 000
Pyrrhotite (o)	1250 to 6.3×10^6
Ilmenite (o)	314 000 to 3.8×10^6
Magnetite (o)	70 000 to 2×10^7

Elements of the magnetic field

The geomagnetic field can be described in terms of the declination, D, inclination, I, and the total force vector F.

A freely suspended magnetised needle will align itself along the F vector so that at the magnetic (dip) north, the inclination is 90° ; i.e., the needle will point vertically downwards. At the south magnetic (dip) pole, the needle will point vertically upwards. At the magnetic equator, the needle will lie horizontally.

Time variable field

Diurnal Variation: Of more direct significance in magnetic prospecting are the smaller but more rapid oscillations in the earth's field which have a periodicity of about a day and an amplitude averaging about 25 gammas known as Diurnal variations.

The records generally show two types of variations, the quiet day and the disturbed day. The quietday variation is smooth, regular, and low in amplitude; it can be separated into predictable components having both solar and lunar periodicities. The disturbed-day variation is less regular and is associated with magnetic storms.

The diurnal variations are caused by changes in the strength and direction of currents in the ionosphere. On a magnetically 'quiet' (Q) day, the changes are smooth and are on average around 50 nT but with maximum amplitudes up to 200 nT at the geomagnetic equator. The changes are least during the night when the background is almost constant, and decrease in amplitude from dawn to midday where upon they increase to the daily maximum about mid-late afternoon before settling down to the night-time value.

Secular Variation: Slow changes in the earth's field which take place progressively over decades or centuries are known as secular variations. Such changes are noted in all the magnetic elements at magnetic observatories everywhere in the world. Secular variation is a slow, progressive, temporal change in all the geomagnetic elements.

Magnetic Storms: In addition to the predictable short-term variations in the earth's field, there are transient disturbances which by analogy with their meteorological counterparts are called magnetic storms. Such storms cause considerable disruption in magnetic prospecting operations. The oscillations that take place while they are going on are so rapid and unpredictable that it usually is not feasible to correct for them as with diurnal variations. Magnetic surveys must generally be

discontinued during storms of any severity. From the equator to latitudes of 60° , the oscillations during such storms may have amplitudes as great as 1000 gammas. In Polar Regions, particularly during auroral displays, the storms may be accompanied by much greater amplitudes of magnetic variation. Their frequency correlates with the extent of sunspot activity. As the sun rotates, carrying sunspots away and toward the earth, some prediction of magnetic storms can be accomplished. The more intense storms begin suddenly, rage simultaneously all around the world, and usually last for several days.

International Geomagnetic Reference Field (IGRF): defines the theoretical undisturbed magnetic field at any point on the Earth's surface. In magnetic surveying, the IGRF is used to remove from the magnetic data those magnetic variations attributable to this theoretical field. The formula is considerably more complex than the equivalent Gravity Formula used for latitude correction.

Corrections for Magnetic Variations

Secular Variation: The need to tie different surveys, observed at different times, together and so compare individual magnetic responses in different areas has led to the development of models of the estimated value and the annual change of the main magnetic field of the earth. One such model is the International Geomagnetic Reference Field (IGRF). The IGRF is a mathematical model of the earth's main field and its temporal variations and consists of a series of spherical harmonics based on worldwide magnetic observatory data. The model was developed in 1968 and is periodically updated. It has become standard processing practice for magnetic surveys that the applicable IGRF (updated to the time of the survey) is subtracted from the observed values of the total magnetic intensity.

Diurnal Variation: The correction for the observed diurnal variation is more problematical, because the daily variation of the earth's magnetic field is highly variable and cannot easily be approximated by a mathematical model. Diurnal variations are subject to amplitude and phase changes, depending on the geographic location of the observer, and can also be influenced by geological conditions, such as rock susceptibility, at the place of observation. The necessary corrections are mostly attempted by the continuous observation of a base-station magnetometer located in or near the survey area. The measured magnetic field in the survey area is then corrected for the observed diurnal changes, either through a direct subtraction of the two data sets or through the manual removal of corresponding anomalies from the observed survey data. For most marine magnetic surveys or airborne magnetic surveys in remote localities, the placement of a base magnetometer in or near the survey area can present a logistical problem. Significant phase and/or amplitude differences in the observed diurnal data from the base station and the survey area can be present and may require additional techniques, such as a cross correlation method, to effectively remove the diurnal events in the observed total field. In some cases, the effects of diurnal variation can be minimized by a tie-line analysis of the observed data set.

Magnetic Storms: The variations in the magnetic field due to magnetic storms can be so rapid, unpredictable, and of such large amplitude, that normally no corrections can be made. Magnetic surveying is therefore generally discontinued under these conditions.

CHAPTER THREE

METHODOLOGY

3.1 Data Collection

This section provides a detailed description of the three geophysical techniques and methodology used for data collection and processing. These methods were selected because of their application in determining the position, depth, and lateral extent of buried utilities.

3.1.1 Electrical Resistivity (ER)p

The SuperSting R8 system manufactured by American Geoscience Institute (AGI) was used during data collection for the 2D electrical resistivity survey. The SuperSting R8 system is made up of resistivity/IP meter, 112 electrodes that are connected via cable, and an energy source that is used to power the resistivity/IP meter. These components were set up during acquisition as shown in Figure 3.1.

For the measurement, the resistivity meter was set for two-cycle stacking and the standard error of measurements of less than 10%.

Data were collected at three different locations using Dipole – Dipole array. At location 1, three traverses were established. Each traverse was 3 meters apart and 11.2 meters long. The electrodes were placed at a 0.1-meter interval in order to ensure high resolution and be able to delineate the buried pipe. Figure 3.2 shows how the traverses were established from Google Earth.

At location 2, three traverses were also established. The first two traverses were 5 meters apart while the third traverse was established 10 meters away from the second traverse (Figure 3.3). The traverses were 11.2 meters long with an electrode spacing of 0.1 meter.



Figure 3.1 The setup of the SuperSting R8



Figure 3.2 Map showing 2D resistivity traverses at Location 1

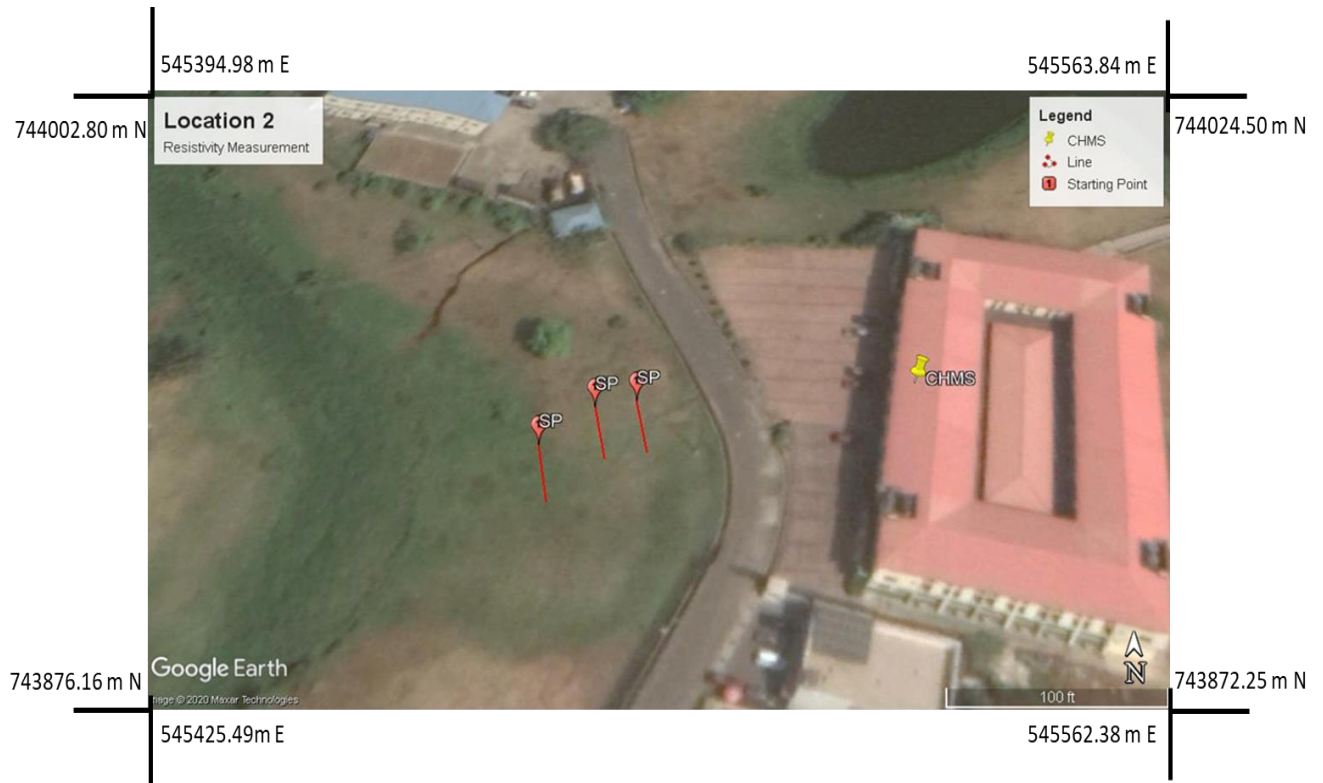


Figure 3.3 Map showing 2D resistivity traverses at Location 2

Data collection at location 3 was divide into two; the first sets of traverses were established at the middle of the survey area to map the first pipe, and the other at one edge of the survey area to map the second pipe (Figure 3.4). Similarly, each of the traverses was 11.2 meters long with an electrode spacing of 0.1 meter.



Figure 3.4 Map showing 2D resistivity traverses at Location 3

3.1.2 Ground Penetrating Radar (GPR)

The MALA Ground Explorer (Figure 3.5) was used in the investigation because it can map the subsurface with high resolution and good for mapping shallow buried utilities. The GPR system is composed of a shielded antenna, a control unit, and a MALA rough terrain cart. The MALA Ground Explorer has a full surveying capability with interchangeable shielded antennas range of 80 – 750 MHz. Each of these antennas have different resolution and different depth of investigation (DOI) due to their different frequencies. The higher the frequency, the higher the resolution and shallow DOI. Also, the lower the frequency, the lower the resolution and deeper DOI.



Figure 3.5 MALA Ground Explorer

For this study, two antennas were used: 450MHz and 750MHz. The 450 MHz and the 750MHz antennas were chosen to produce a high resolution of the shallow subsurface. Proper settings were adjusted, signals were released by a trigger connected to the measuring wheel. Data were collected at three different locations. Location 1, 2, and 3 are represented by Figure 3.6, Figure 3.7, and

Figure 3.8 respectively. The red lines on the maps represent the traverses that were taken during the survey in each of the locations. The 3D GPR is represented by black boxes at each of the respective locations. Table 3.1 summarizes the GPR survey at each of the three locations.

Table 3.1 Table showing the number of traverses in each location

Location	Number of Traverses	Length of Traverse (m)	3D GPR
1	3	30	6 by 6m at 1m interval
2	6	11	3 by 3m at 0.5m interval
3	3	65	3 by 3m at 0.5m interval

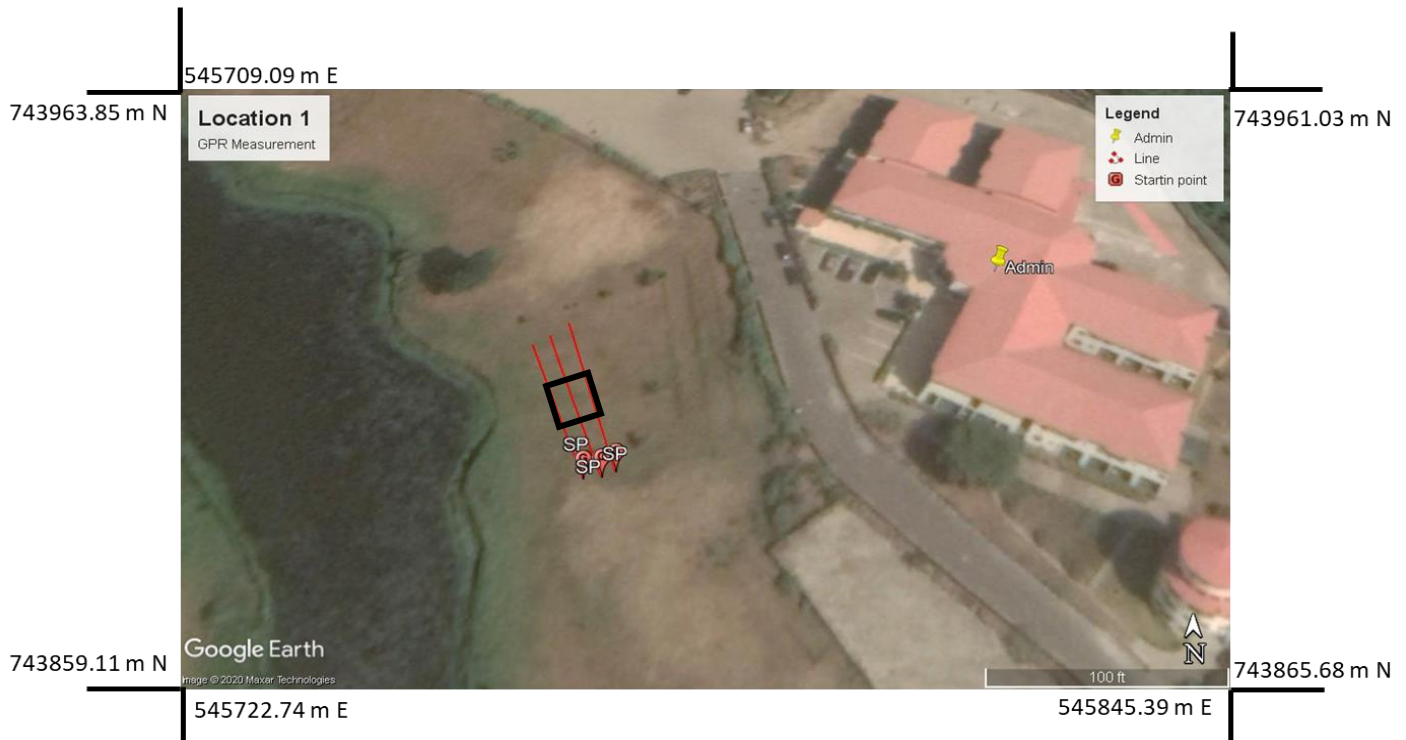


Figure 3.6 Map showing GPR traverses and 3D GPR at Location 1



Figure 3.7 Map showing GPR traverses and 3D GPR at Location 2



Figure 3.8 Map showing GPR traverses and 3D GPR at Location 3

3.1.2 Magnetics Methods

The Scintrex ENVI PRO magnetometer was used to record the total magnetic fields of the study areas. The ENVI PRO is a lightweight, portable proton precession magnetometer with integrated GPS and versatile design that offers users. The ENVI PRO system is composed of a control unit, a GPS antenna, a total field sensor and/or gradiometer sensor, sensor staff and, a backpack (Figure 3.9).

Data were collected along three traverses, 30 meters long and 3 meters apart at Location 1 (Figure 3.10). At location 2, data were collected along six traverses, 11 meters long and 5 meters apart (Figure 3.11).



Figure 3.9 ENVI PRO during data acquisition



Figure 3.10 Map showing magnetic traverses at Location 1

Lastly, at location 3, data was collected over 3 traverses; the first and the third traverse were collected over 40 meters while the third traverse was collected over 65 meters (Figure 3.12). The interstation spacing for all three locations was 0.1 meter to ensure high resolution.

Base stations were established at each of the locations in other to correct for the diurnal variation. Diurnal variation is the oscillation of the earth's magnetic field which occurs during the day. Repeated readings were taken at each station and base station to check for high amplitudes and inconsistencies in the magnetic field which is likely to be due to magnetic storms. The resulting data was first processes using Microsoft Excel to correct for the diurnal variation in the earth's magnetic field and to generate profiles for each location.

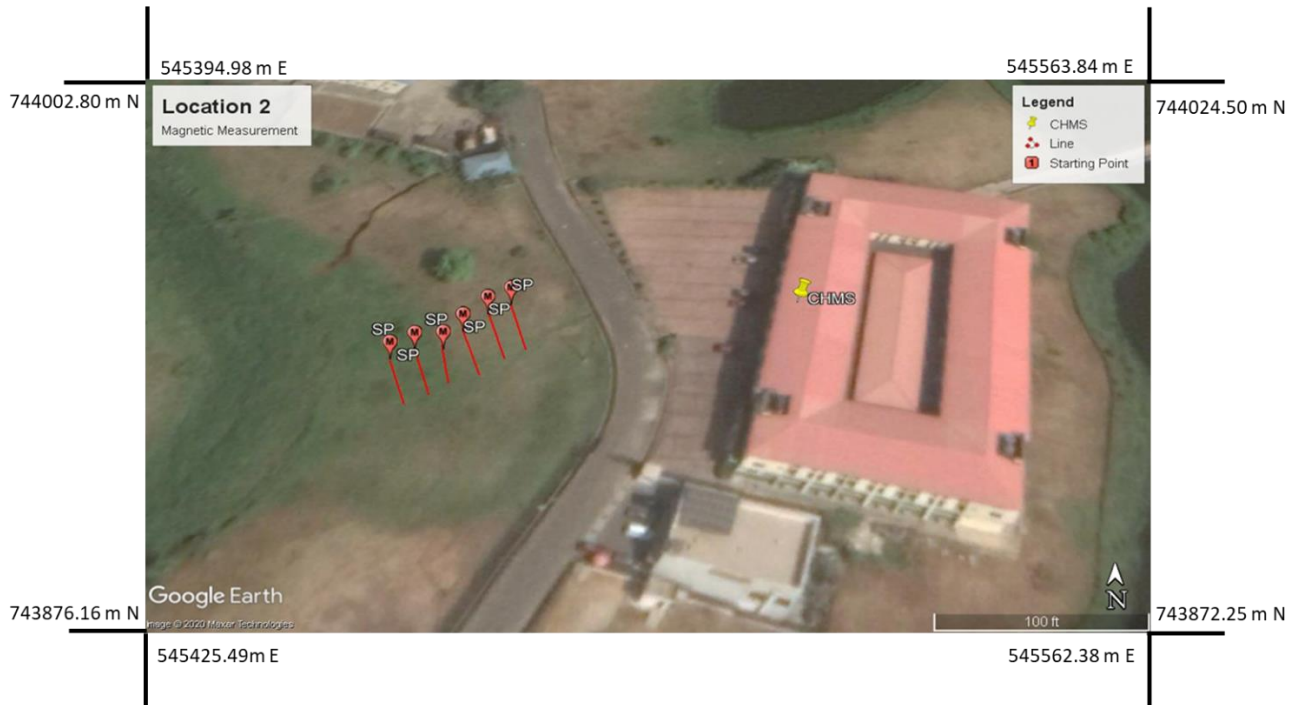


Figure 3.11 Map showing magnetic traverses at Location 2



Figure 3.12 Map showing magnetic traverses at Location 3

3.2 Data Processing and Interpretation

Magnetic Method

Repeated readings were taken at each station and base station to check for high amplitudes and inconsistencies in the magnetic field which is likely to be due to magnetic storms. The resulting data was first processed using Microsoft Excel to correct for the diurnal variation in the earth's magnetic field and to generate profiles for each location.

Electrical Resistivity (ER)

The processing program (AGI EarthImager) inverted the data creating the apparent resistivity and final models. The final models were obtained by comparing the calculated data with the observed (raw data) and represents the true distribution of subsurface resistivity underneath each traverse. Figure 3.13 shows an example of a 2D resistivity section obtained along a traverse. (a) shows the raw data, the middle (b) shows the calculated apparent resistivities, and the inverted model is shown in (c). The inverted 2D ERT section is presented and discussed.

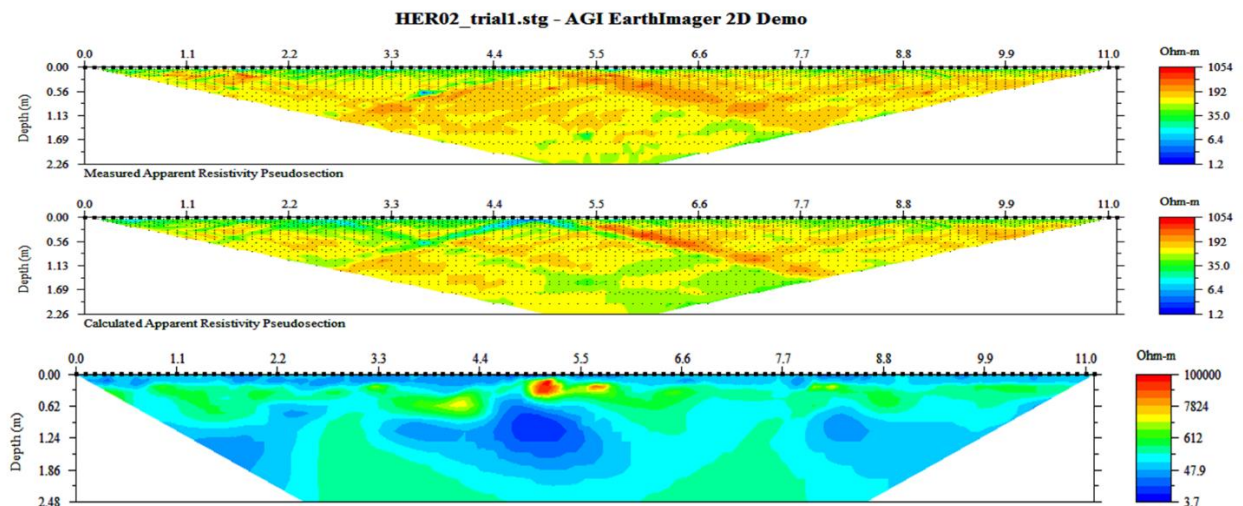


Figure 3.13: a.) Raw apparent resistivity data, b.) calculated apparent resistivity, and c.) Final resistivity model.

Ground Penetrating Radar

The data were processed and analyzed with ReflexW, GPR viewer and manufacturer's cloud-based processing software at <https://malavision.guidelinegeo.com/> for the 3D GPR processing. The following filters: gain control, time zero adjustment, background removal, and topographic correction were applied. The major aim of GPR data processing was to improve the reflected signals from buried utilities and attenuate the noise signals.

Gain control was applied in order to enhance the low amplitude reflections on the radargram. Time zero adjustment adjusts the all the traces to a common zero position so that zero equals ground level and the true depth of the utility is obtained. Background removal all remove interference that is more pronounced than the data and thus presents a clearer image.

CHAPTER FOUR

RESULTS AND DISCUSSION

4.1 Introduction

As discussed in previous chapters, the three geophysical methods used in this study include Magnetics Survey, Electrical Resistivity (ER) Survey, and Ground Penetrating Radar (GPR). The result and discussion are presented in this chapter for each of the geophysical method.

4.2 2D Electrical Resistivity Imaging (ERI)

Location 1

Figure 4.1a is the interpreted inverted 2D electrical resistivity section along Traverse 2. The resistivity along this section ranges from 3.7 Ωm to about 100 $\text{k}\Omega\text{m}$ and a depth of about 2.48m was investigated.

The 2D electrical resistivity section can be characterized into three geoelectric layers based on its vertical and lateral variation in electrical resistivity values. The first region is the topsoil with electrical resistivity range of about 3.7 Ωm to 47.9 Ωm and thickness range of 0.2 to 0.3 m.

The second geoelectric layer is with relatively higher electrical resistivity range of 171 to 612 Ωm and delineated to a depth range of 0.9 to 1m. Along the lateral distance of about 5 to 5.22m an anomalously high electrical resistivity of about 7824 to 100 $\text{k}\Omega\text{m}$ can be observed which is suggestive of buried pipe at a depth range of 0.2 to 0.5m. Therefore, the average diameter of the delineated pipe is about 0.22m.

The third geoelectric layer is represented by resistivity range of 3.7 to 121 Ωm expressive of Clay/Sand layer.

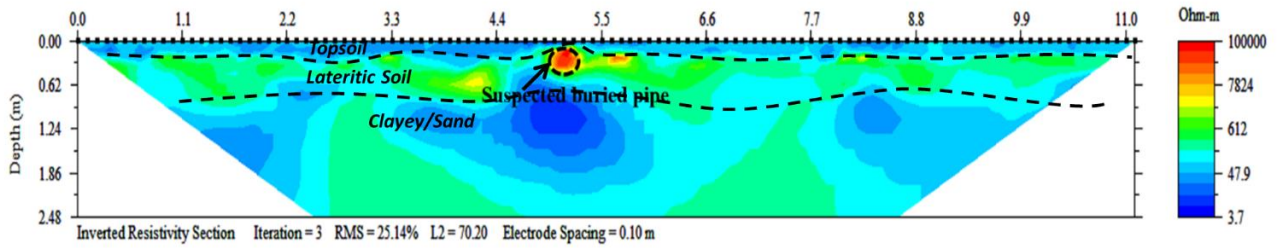


Figure 4.1a. Interpreted inverse model resistivity results for traverse 2

The 2D electrical resistivity section along traverse 3, (Fig 4.1b) is with resistivity value ranging from 1.8 Ωm – 52 $\text{k}\Omega\text{m}$ and a depth of about 2.48 m was investigated.

Similarly, the 2D electrical resistivity section is characterized to three geoelectric layers. The first layer is the topsoil with electrical resistivity range of about 1.8 to 23.8 Ωm and thickness range of 0.2 to 0.3 m.

The second geoelectric layer is with relatively higher electrical resistivity range of 85.9 to 1117 Ωm and delineated to a depth range of 0.47 to 0.5 m. Along the lateral distance of about 4.9 to 5.1 m an anomalously high electrical resistivity of about 4026 Ωm to 52 $\text{k}\Omega\text{m}$ can be observed which is suggestive of buried pipe and at a depth range of 0.2 to 0.5m. Therefore, the average diameter of the delineated pipe is about 0.2 m.

The third geoelectric layer is represented by relatively low resistivity range of 23.8 to 85 Ωm expressive of Clay/Sand layer.

An augmented 3D view of the inverted 2D sections at location 1 is presented in Figure 4.1c. The augmented 3D view has shown the continuity of the anomaly associated to the pipe across the two traverses.

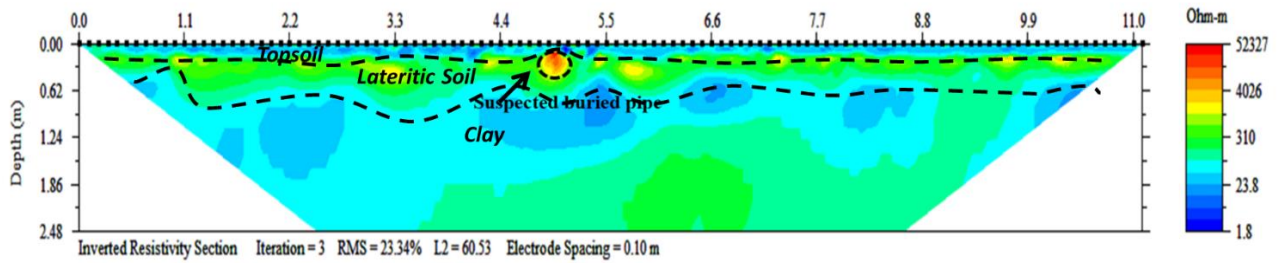


Figure 4.1b. Interpreted inverse model resistivity results for traverse 2.

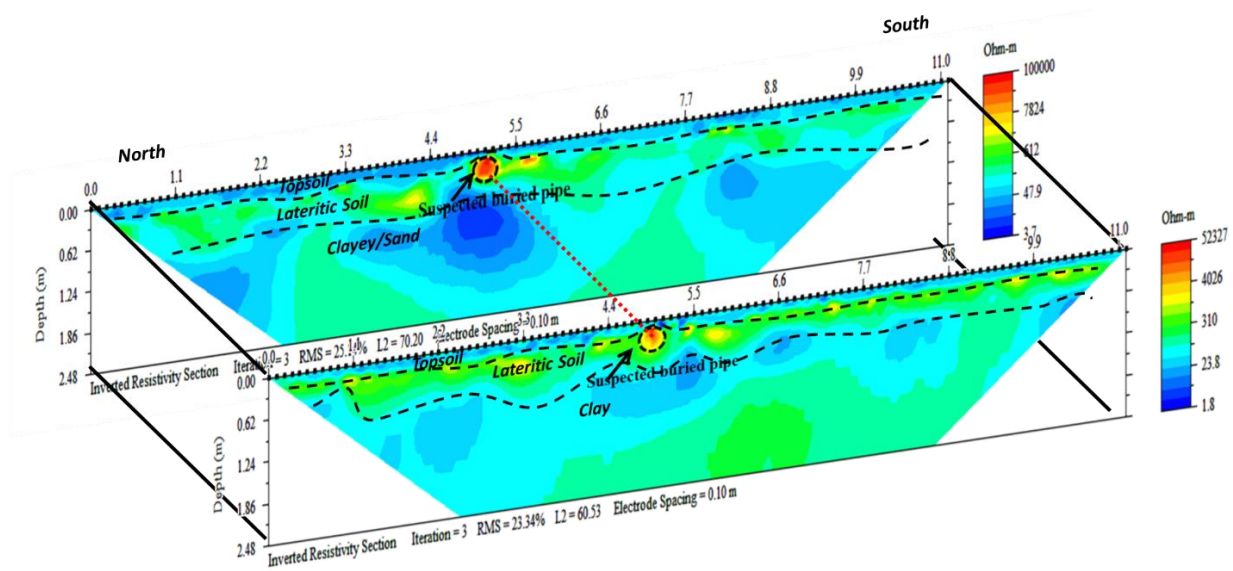


Fig 4.1c Augmented 3D view of the inverted 2D ERT sections at Location 1

Location 2

Traverse 1: Figure 4.2a represents the interpreted inverted 2D electrical resistivity section along Traverse 1 in location 2. The resistivity along this section ranges from 7.7 to 1910 Ωm and a depth of about 2.48 m was investigated.

The 2D electrical resistivity section can be characterized into three geoelectric layers based on its vertical and lateral variation in electrical resistivity values. The first region is the topsoil with electrical resistivity range of about 7.7 to 30.6 Ωm and thickness range of 0.2 to 0.3 m.

The second geoelectric layer is with relatively higher electrical resistivity range of 60.8 to 283.3 Ωm and delineated to a depth range of 0.5 to 0.6 m. Along the lateral distance of about 5.50 to 5.78 m an anomalously high electrical resistivity of about 481 to 958 Ωm can be observed which is suggestive of buried pipe and at a depth range of 0.16 to 0.41 m. Therefore, the average diameter of the delineated pipe is about 0.25 m.

The third geoelectric layer is represented by resistivity range of 7.7 to 30.6 Ωm expressive of Clay layer.

Traverse 2: Figure 4.2b representing the interpreted inverted 2D section along traverse 2 has a resistivity range of range of 8.7 to 1766 Ωm and a depth of about 2.48 m. The 2D electrical resistivity section can be characterized into four geoelectric layers based on its vertical and lateral variation in electrical resistivity values. The first geoelectric layer is the topsoil with electrical resistivity range of about 16.9 to 32.8 Ωm and thickness range of 0.2 to 0.3 m.

The second geoelectric layer is with relatively higher electrical resistivity range of 121 to 481 Ωm and delineated to a depth range of 0.5 to 0.9 m. An anomalously high electrical resistivity of about 481 to 1910 Ωm can be observed along the lateral distance of about 5.41 to 5.67 m which is suggestive of buried pipe and at a depth range of 0.16 to 0.41 m. Therefore, the average diameter of the delineated pipe is about 0.25 m.

An augmented 3D view of the inverted 2D sections at location 2 is presented in Figure 4.2c. The augmented 3D view has shown the continuity of the anomaly associated to the pipe across the two traverses.

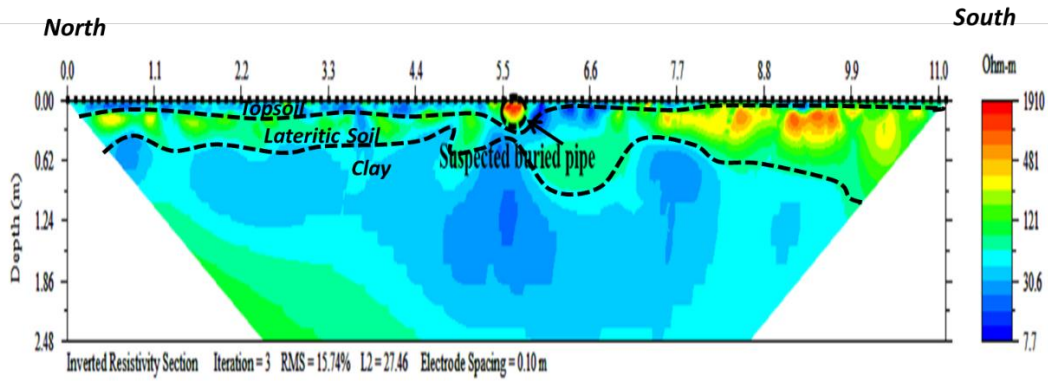


Figure 4.2a. Interpreted inverse model resistivity results for traverse 1.

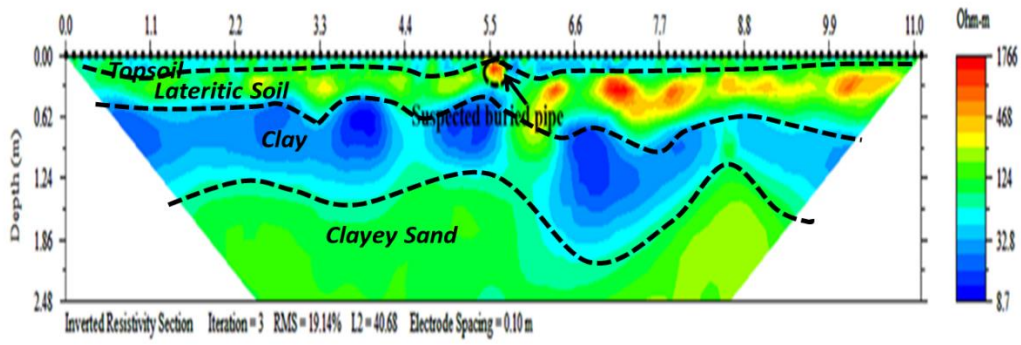


Figure 4.2b. Interpreted inverse model resistivity results for traverse 2.

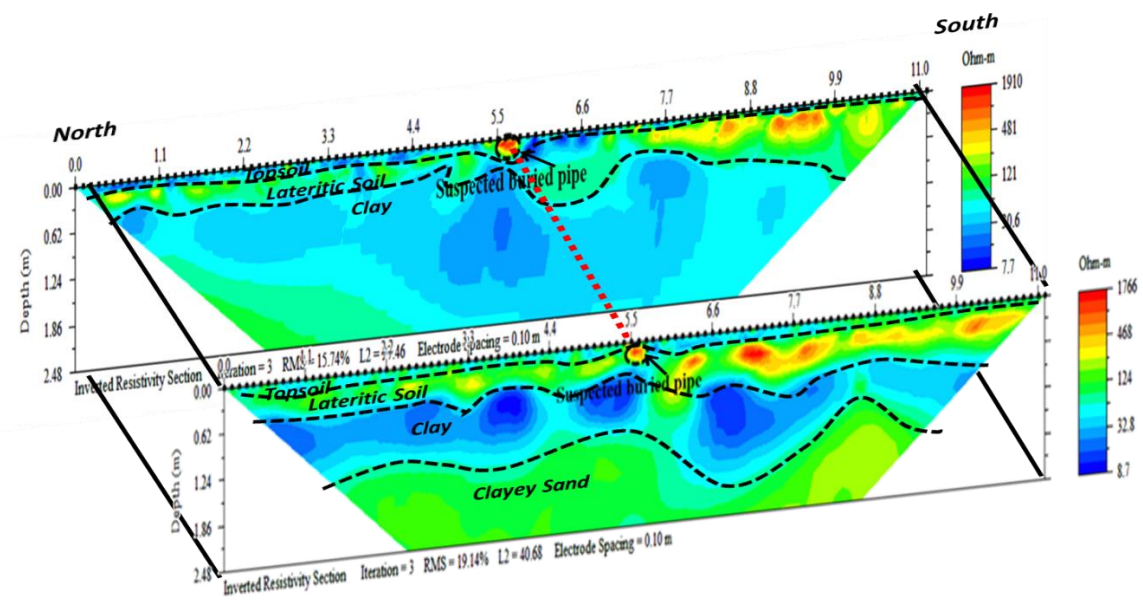


Fig 4.2c Augmented 3D view of the inverted 2D ERT sections at Location 2

Location 3

Pipe 1:

The 2D electrical resistivity inverted section of traverse 1 (Figure 4.3) fails to map the buried pipe. It does not show an interpretable anomaly for the buried pipe. Hence, it could not be resolved.

However, Figure 4.4a is the interpreted inverted 2D electrical resistivity section along traverse 2. The resistivity along this section ranges from 10.9 to 752 Ωm and a depth of about 2.48 m was investigated.

The 2D electrical resistivity section can be characterized into four geoelectric layers based on its vertical and lateral variation in electrical resistivity values. The first layer is the topsoil with electrical resistivity range of about 18.5 to 53.5 Ωm and thickness range of 0.2 to 0.3 m.

The second geoelectric layer is with relatively higher electrical resistivity range of 91 to 261 Ωm and delineate to a depth range of 0.58 to 0.6 m. Along the lateral distance of about 5.41 to 5.69 m an anomalously high electrical resistivity of about 154 to 443 Ωm can be observed which is suggestive of buried pipe and at a depth of 0.29 m.

The third geoelectric layer is represented by resistivity range of 10.9 to 91 Ωm expressive of Clay Sand layer. The fourth geoelectric layer is represented by resistivity of about 91 to 154 Ωm expressive of Clayey Sand layer.

Figure 4.4b is the interpreted inverted 2D electrical resistivity section along traverse 2. The resistivity along this section ranges from 10.9 to 752 Ωm and a depth of about 2.48 m was investigated.

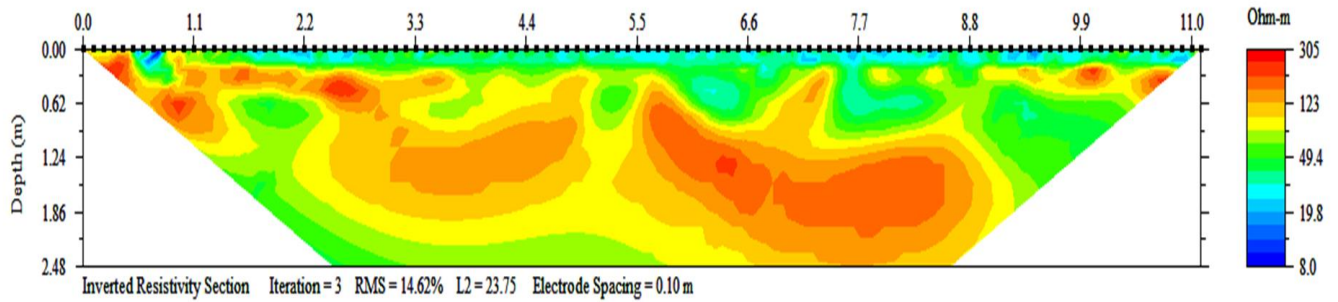


Figure 4.3 Inverse model resistivity results for traverse 1.

The 2D electrical resistivity section can be characterized into three geoelectric layers based on its vertical and lateral variation in electrical resistivity values. The first layer is the topsoil with electrical resistivity range of about 10.9 to 18.5 Ωm and thickness range of 0.2 to 0.3 m.

The second geoelectric layer is with relatively higher electrical resistivity range of 31.5 to 91 Ωm and delineated to a depth range of 0.31 to 0.61 m. Along the lateral distance of about 5.2 to 5.49 m an anomalously high electrical resistivity of about 154 to 261 Ωm can be observed which is suggestive of buried pipe and at a depth of 0.31 m.

The third geoelectric layer is represented by resistivity range of 10.9 to 31.4 Ωm expressive of Clayey layer. An augmented 3D view of the inverted 2D sections is presented in Figure 4.4c and have shown the continuity of the anomaly associated to the pipeline across the two traverses.

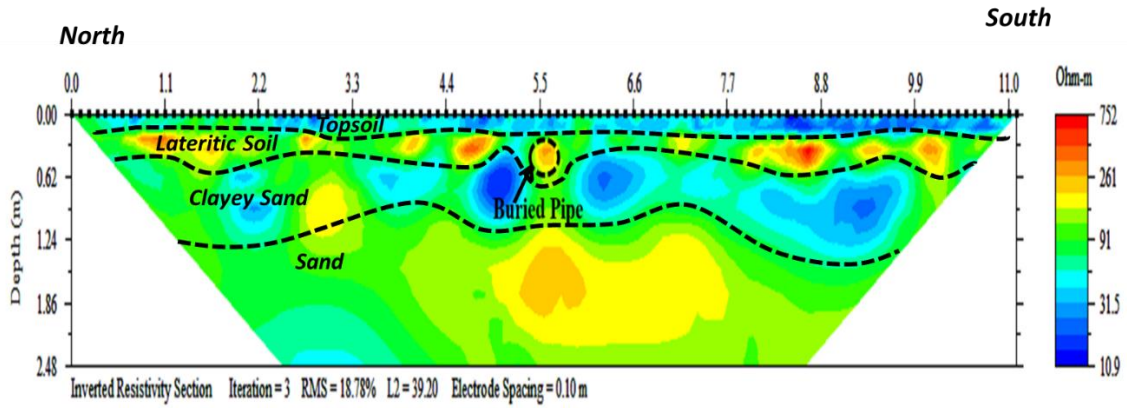


Figure 4.4a. Interpreted inverse model resistivity results for traverse 2.

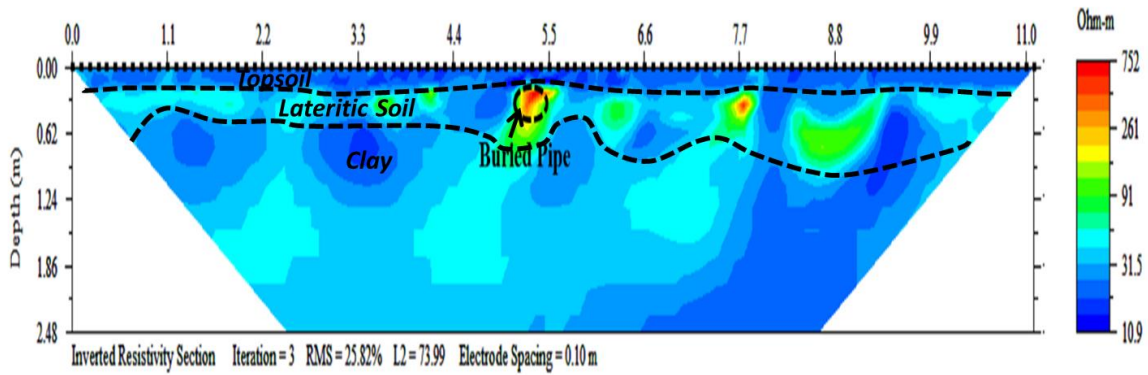


Figure 4.4b. Interpreted inverse model resistivity results for traverse 3.

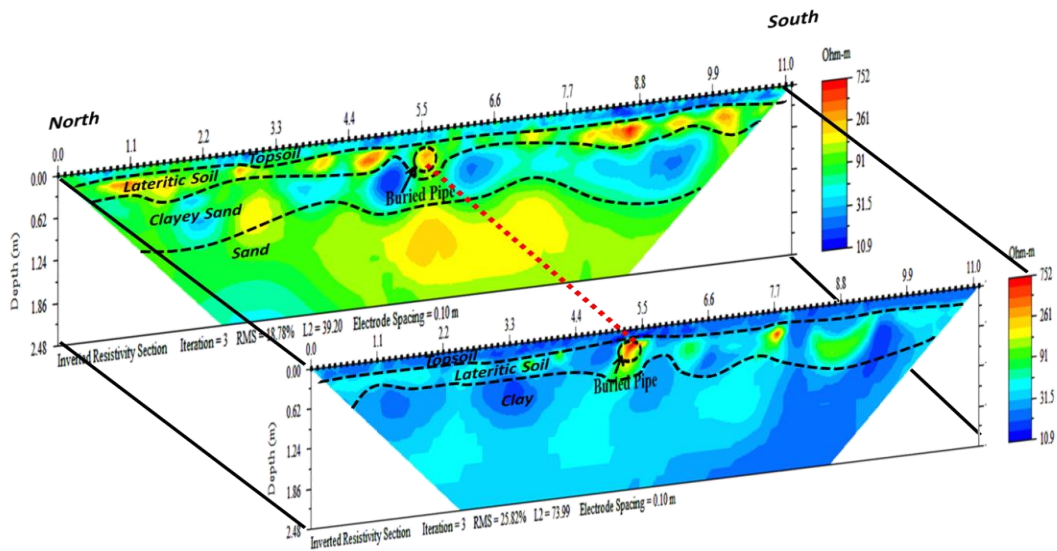


Figure 4.4c. Augmented 3D view of the inverted 2D ERT sections for pipe 1 at Location 3 (Pipe 1).

Pipe 2:

Similarly, Figures 4.5a and 4.5b are the interpreted inverted 2D electrical resistivity sections along traverses 2 and 3 around Pipe 2 at location 3. On traverse 2, anomalously high electrical resistivity of about 1152 to 16763 Ωm can be observed along the lateral distance of about 5.8 to 6.05 m which is suggestive of buried pipe and at a depth of 0.25 m.

Likewise, on traverse 3, an anomalously high electrical resistivity of about 7342 to 100 k Ωm can be observed along the lateral distance of about 5.6 to 5.85 m which can be associated to the buried pipe (Figure 4.5b). An augmented 3D view of the inverted 2D sections is presented in Figure 4.5c and have shown the continuity of the anomaly associated to the pipeline across the two traverses.

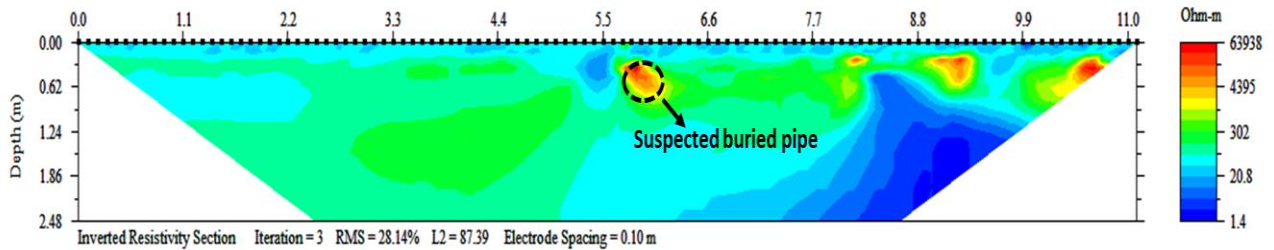


Figure 4.5a. Interpreted inverted 2D ERT for traverse 2 at Pipe 2, Location 3.

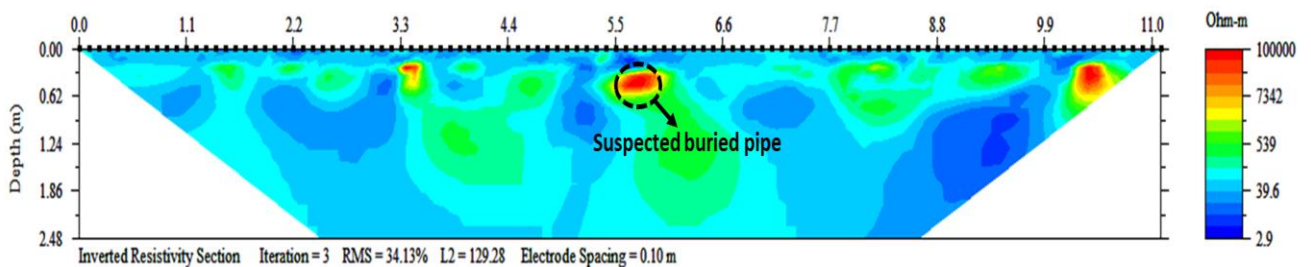


Figure 4.5b. Interpreted inverted 2D ERT for traverse 3 at Pipe 2, Location 3.

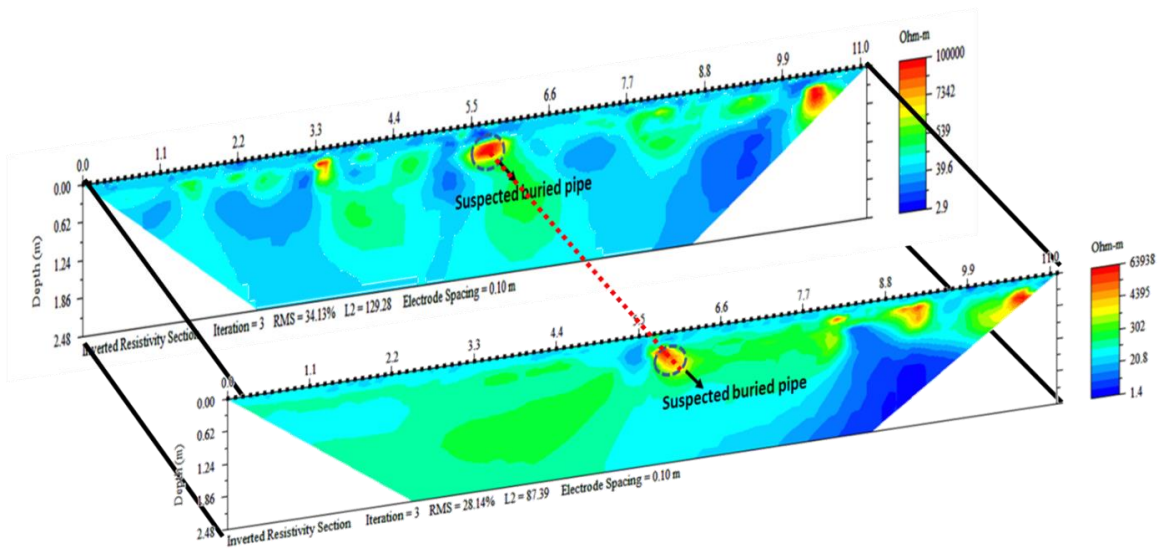


Figure 4.5c. Augmented 3D view of the inverted 2D ERT sections for pipe 2 at Location 3.

4.2 Magnetism Method

Generally, the observed magnetic anomalies in the region were rather subtle due to the abundance of cultural noises and lateral inhomogeneity resulting from sand filling/ landscaping of the environment. The data quality was also not the best. It was dominated by spikes and steps. However, attempts were still made to deduce reasonable interpretation. Presented are the figures showing the results obtained from the magnetic profile at each location. The drift corrected data are however, presented in Appendix A.

Location 1

Figure 4.6 shows the magnetic profile of traverse 1 and 3 showing an attempted interpretation of the buried pipe in location 1. The signature indicates that the pipe is located at 16 m mark along the traverse. The profile for traverse 2 (presented in Appendix A) did not show an interpretable signature.

Shown in figure 4.6 (a.), 4.6(b.) and 4.6(c) are magnetic profiles 1, 2 and 3. Signatures likely to be buried by buried pipe were identified at a distance 16 m from the beginning of the lines on profile 1 and 3 while no interpretable signature was identified on profile 2.

Similar signature is observed on traverse 3 which also indicates that the pipe is located at 16 m mark.

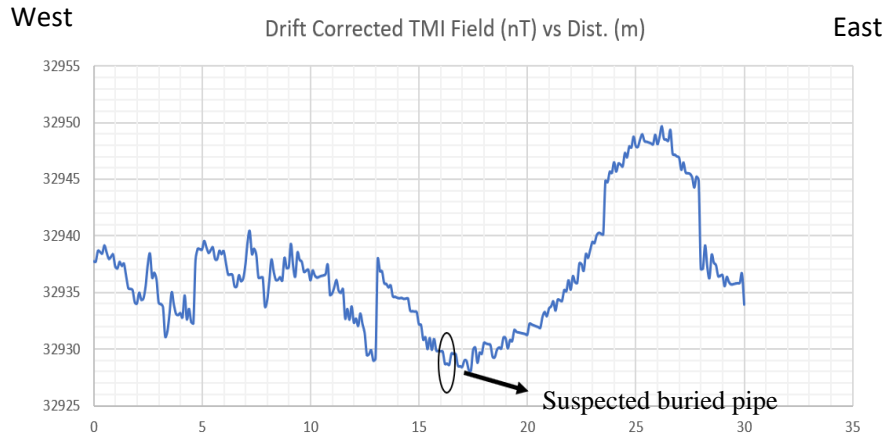


Figure 4.6(a)i. Total magnetic intensity (TMI) plot for profile 1.

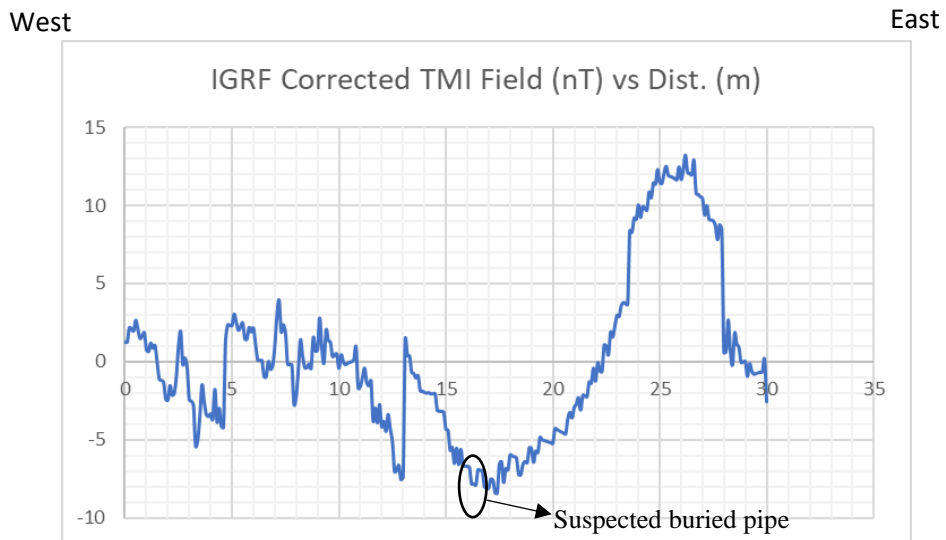


Figure 4.6(a)ii. IGRF corrected TMI plot for profile 1.

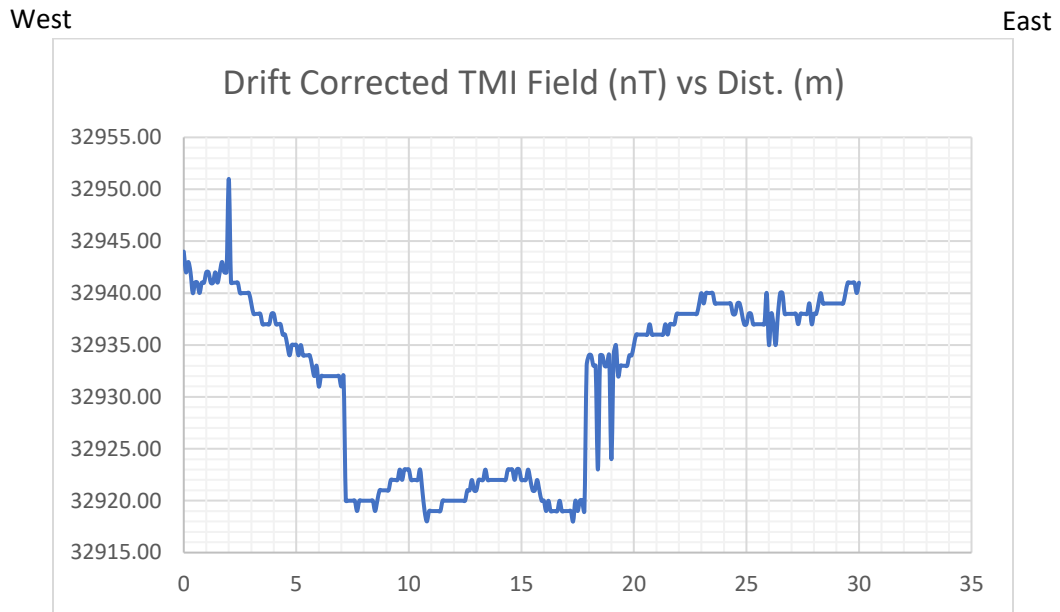


Figure 4.6(b)i. Total magnetic intensity (TMI) plot for profile 2.

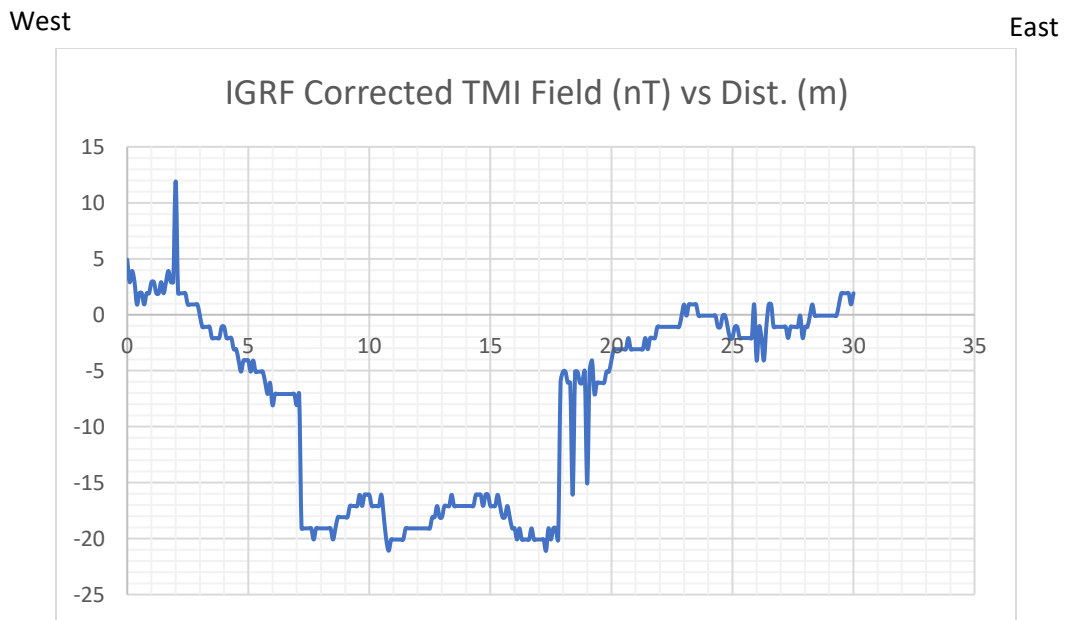


Figure 4.6(b)ii. IGRF corrected TMI plot for profile 2.

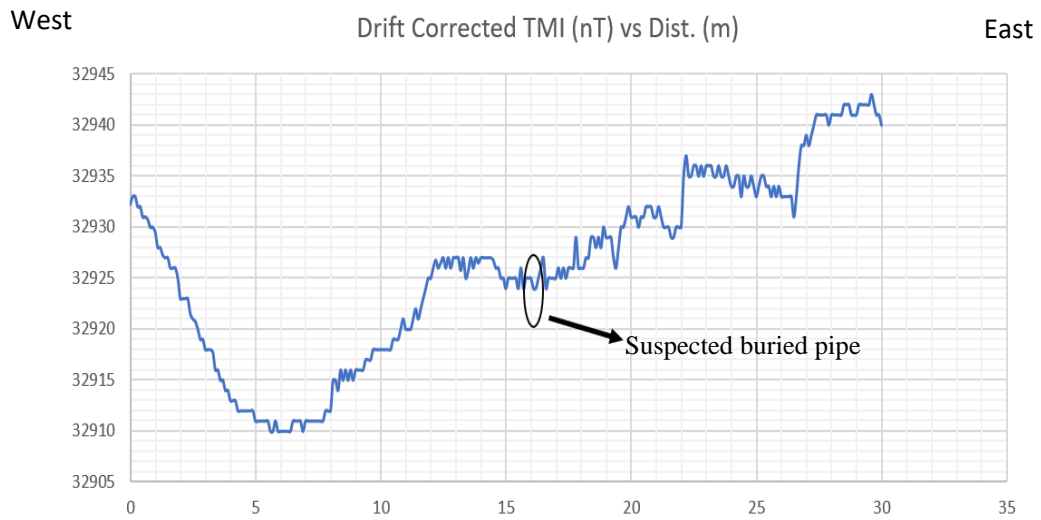


Figure 4.6(c)i. Total magnetic intensity (TMI) plot for profile 3.

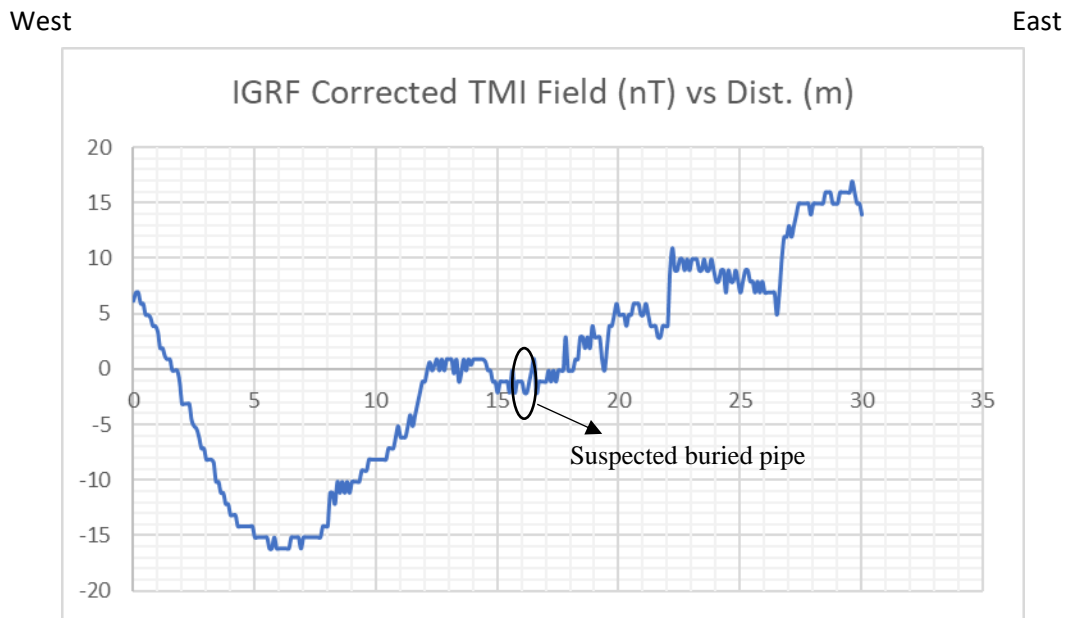


Figure 4.6(c)ii. IGRF corrected TMI plot for profile 3.

Location 2

Shown in Figure 4.7(a), 4.7(b) and 4.7(c) are magnetic profiles 1, 2 and 4 at location 2. The position of the pipe across the three (3) profiles varies. it was mapped at 4.4 m from the start of the profile 1, 4.7 m on profile 2 and 6.2 m on profile 4. This validates that the buried pipe was trending in the NW-SE direction. Profile 3, 5 and 6 (presented in Appendix A) did not show any appreciable signature that can be interpreted as the buried pipe.

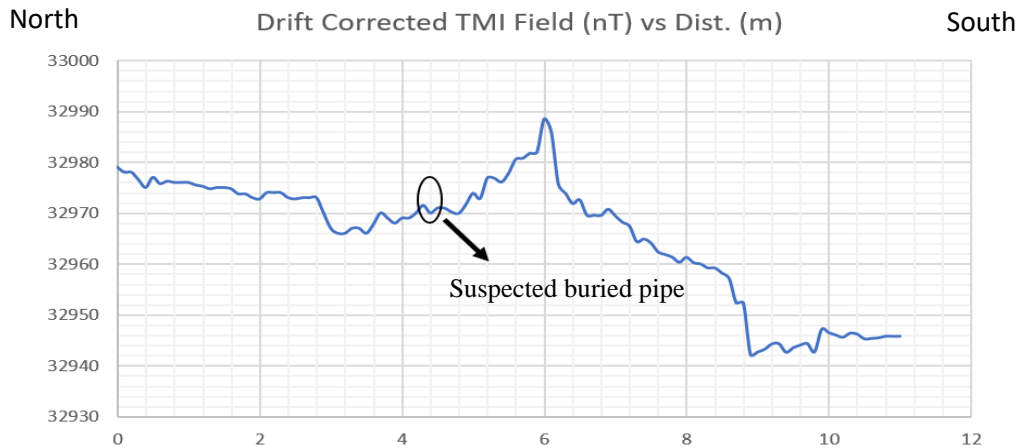


Figure 4.7(a)i. Total magnetic intensity (TMI) plot for profile 1.

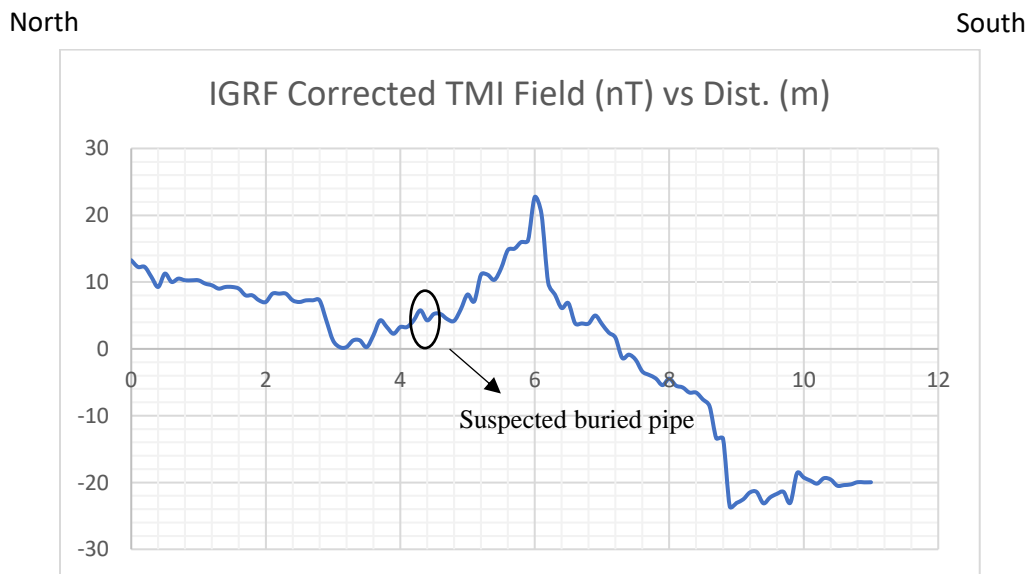


Figure 4.7(a)ii. IGRF corrected TMI plot for profile 1.

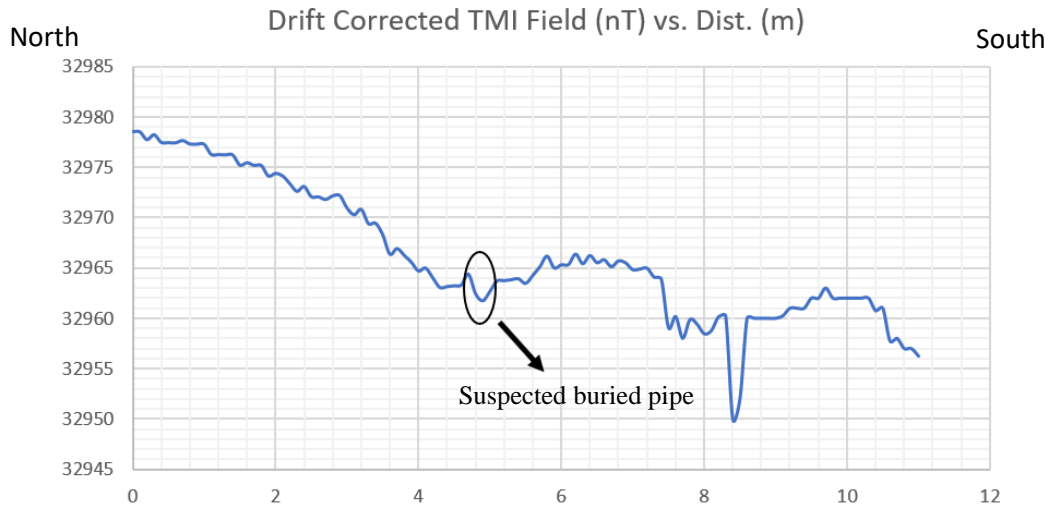


Figure 4.7(b)i. Total magnetic intensity (TMI) plot for profile 2

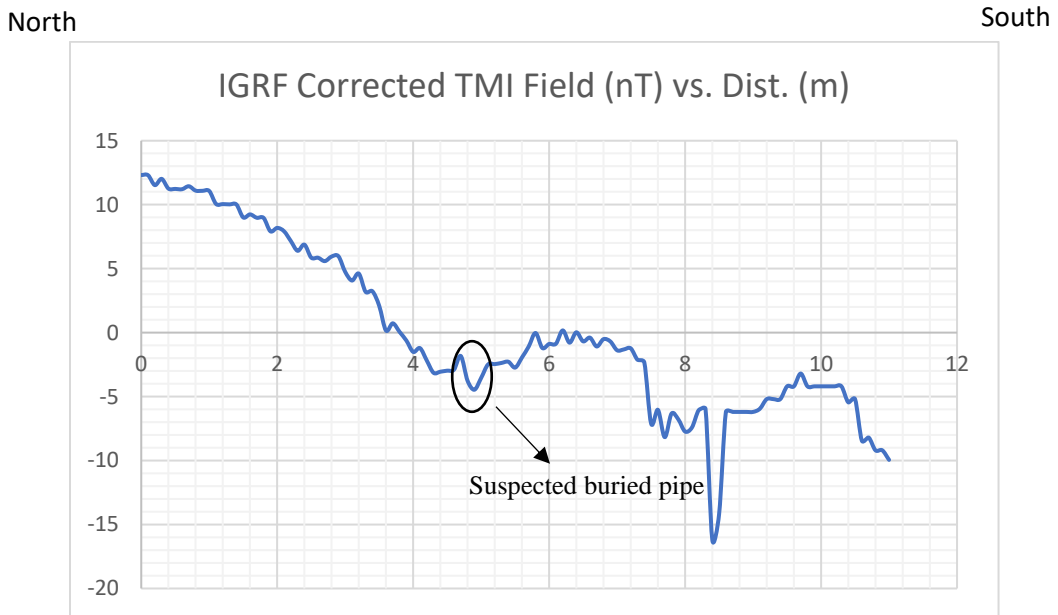


Figure 4.7(b)ii. IGRF corrected TMI plot for profile 2.

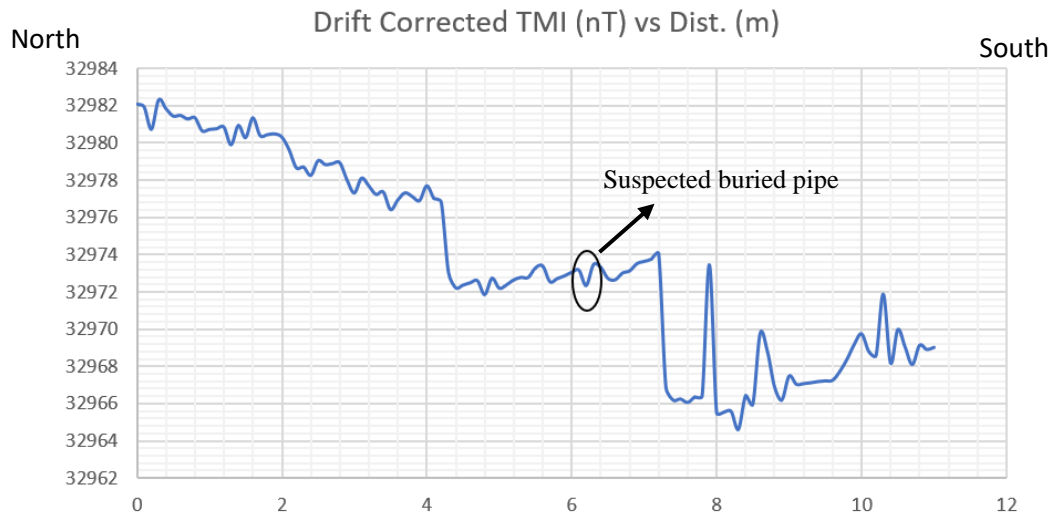


Figure 4.7(c)i. Total magnetic intensity (TMI) plot for profile 4

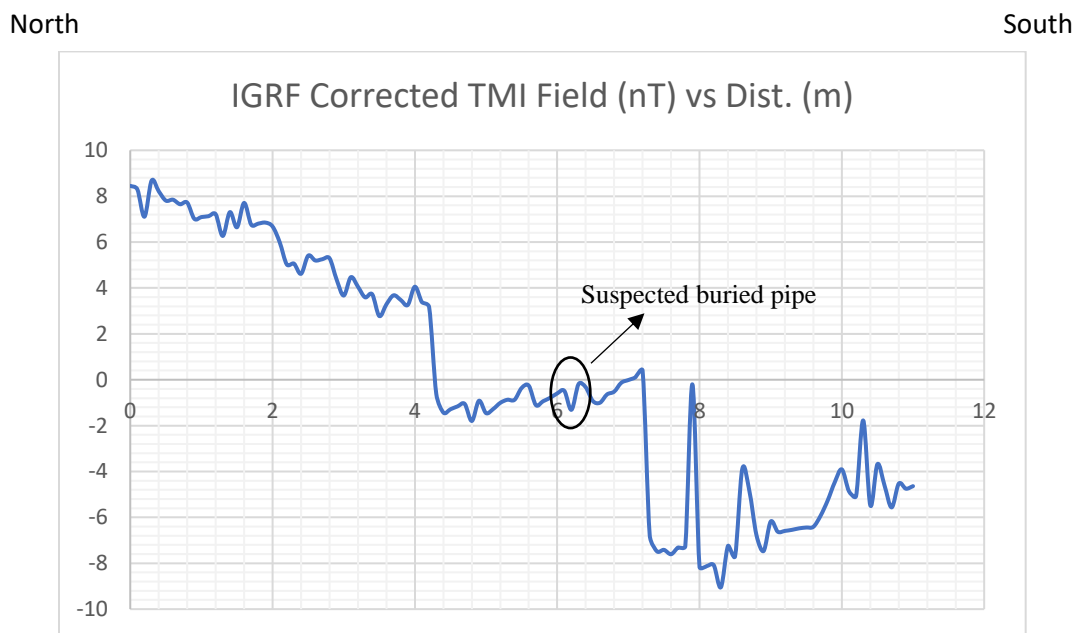


Figure 4.7(c)ii. IGRF corrected TMI plot for profile 4.

Location 3

Three magnetic profiles were acquired in the approximate N – S direction in this location. Only two of the three profiles, only two were interpretable. Presented in Figures 4.8(a) and 4.8(b) are the two interpretable profiles. Although, no conspicuous signature due to a buried pipe was found, a conspicuous magnetic low approximately 2 m wide (occurring between 40.7 m to 42.7 m from the start of profile one 4.8(a) and 45.2 m to 47.5 m from the start of the of profile two 4.8(b)) was delineated. The conspicuous magnetic low was interpreted as a geologic structure relating to a buried stream/river channel.

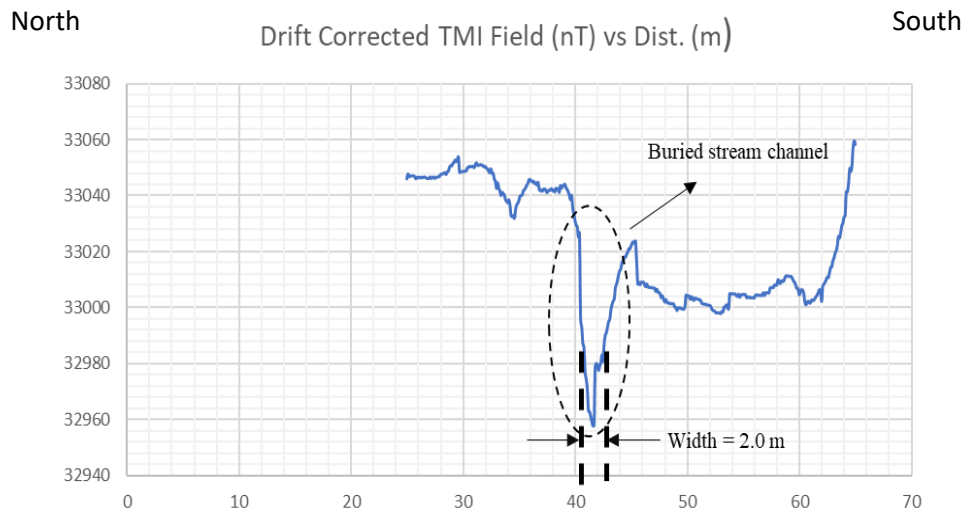


Figure 4.8(a)i. Total magnetic intensity (TMI) plot for profile 1

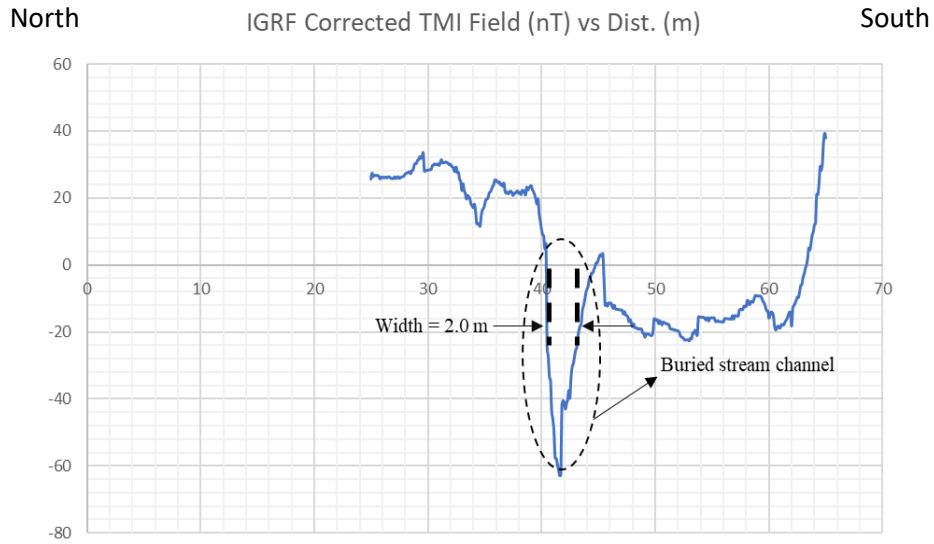


Figure 4.8(a)ii. IGRF corrected TMI plot for profile 1.

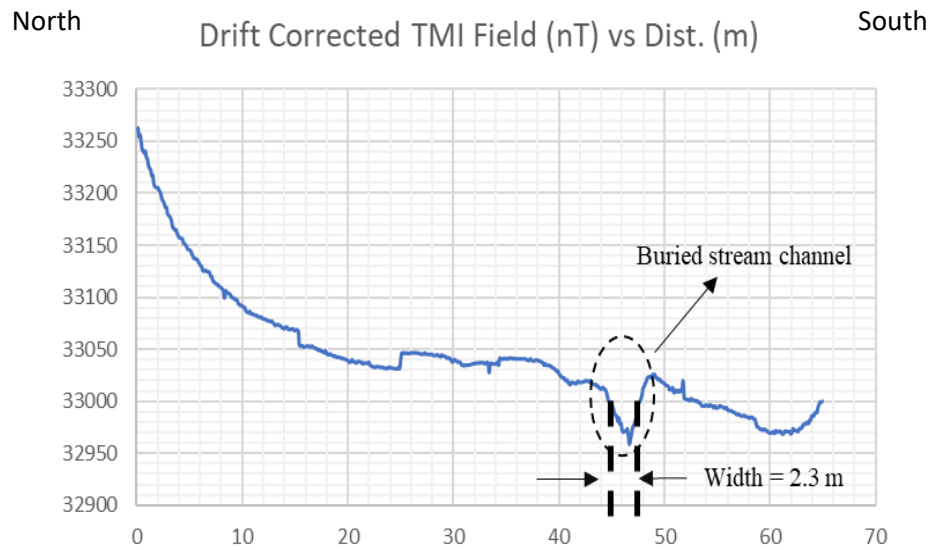


Figure 4.8(b)i. Total magnetic intensity (TMI) plot for profile 2

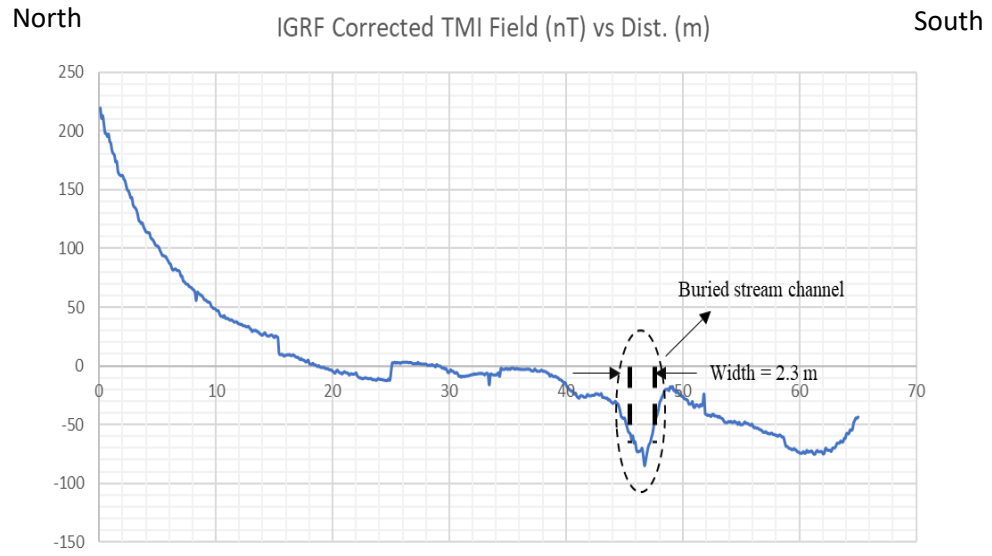


Figure 4.8(b)ii. IGRF corrected TMI plot for profile 2.

4.3 Ground Penetrating Radar

As discussed in the previous chapter two antennas (450 MHz and 750MHz) were used to acquire data at each of the location. The interpreted results acquired on each individual traverse at each of the location is presented and discussed below. The produced radargram for each frequency is included in Appendix B.

Location 1

Figure 4.9a shows the GPR radargram obtained on traverse 1 using the 750 MHz antenna. The hyperbolic signature indicates the suspected buried pipe at the depth of 0.22 m. The top of the hyperbolic signature indicates the middle of the buried pipe which is at a lateral distance of 15 m. A 3D augmented view of the interpreted radar section of other traverses at location 1 is presented in Figure 4.9b which shows the continuity of the anomaly.

The 3D GPR have been presented as an interpreted 3D volume in Figure 4.9c(i). The lines perpendicular to the strike of the pipe in the 3D volume have been interpreted which have shown the position of the pipe in the investigated area (Figure 4.9c(ii)).

The interpreted time slice of the 3D GPR at 0.1m interval is presented in Figure 4.9d. The time slice at 0.2m shows the buried pipe indicated by the yellow box, distinctively.

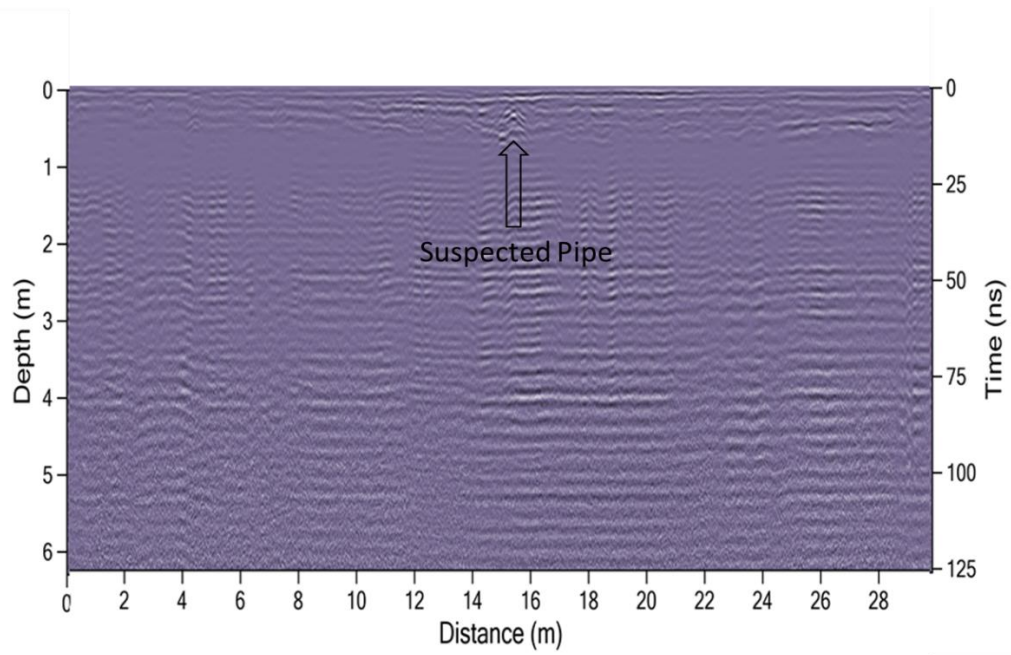


Figure 4.9a Interpreted GPR radargram using the 750 MHz antenna along traverse 1 at Location 1.

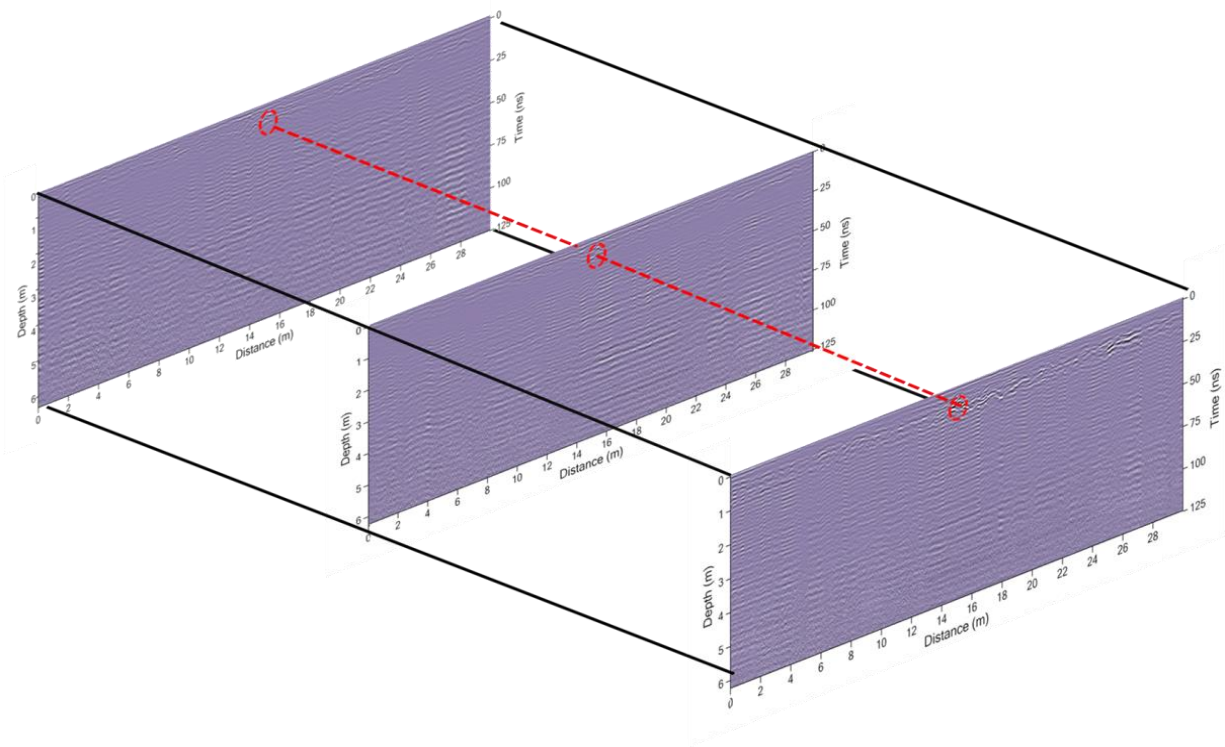


Figure 4.9b Augmented 3D view of the GPR radargram for Location 1.

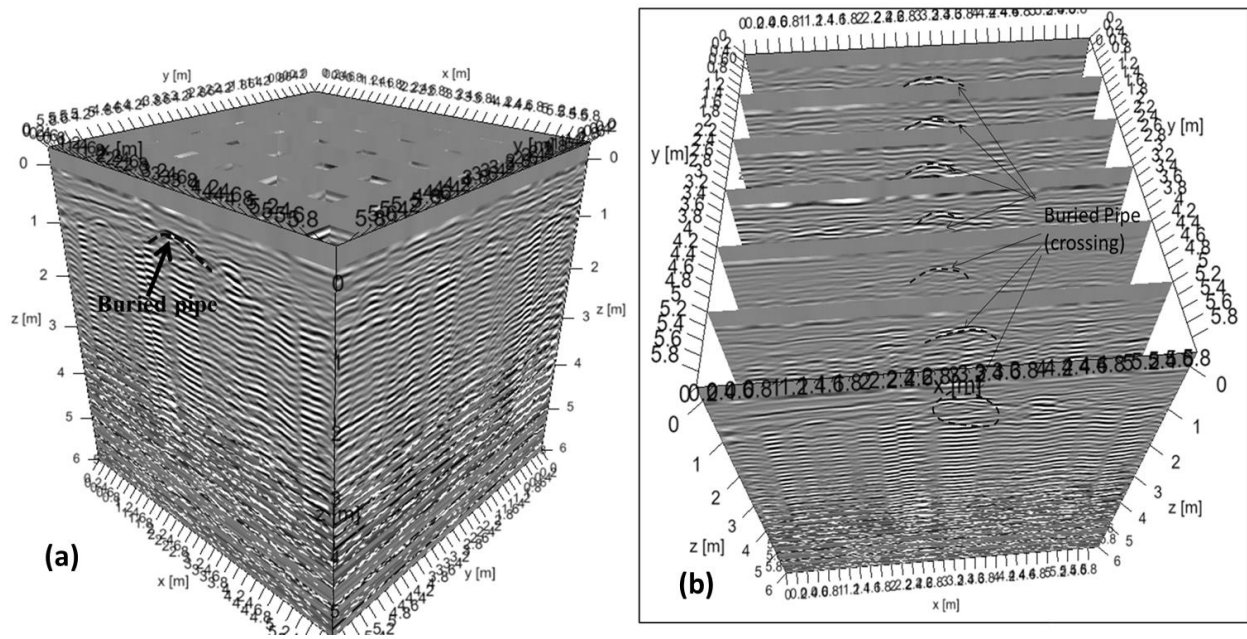


Figure 4.9c Interpreted 3D GPR (i) volume and (ii) dip lines at Location 1

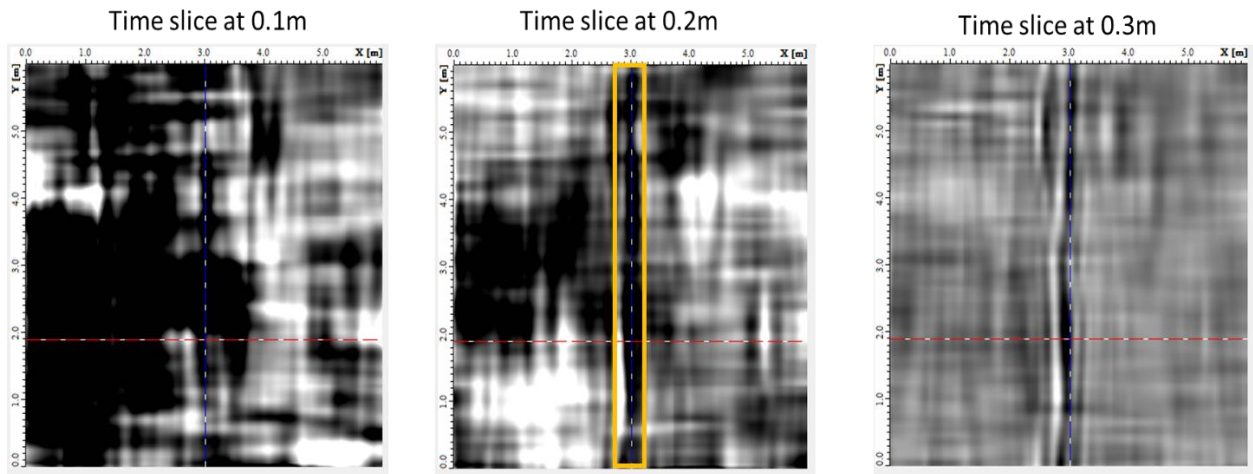


Figure 4.9d Interpreted Time slice of 3D GPR for Location 1.

Location 2

Figure 4.10a shows the GPR radargram obtained on traverse 1 using the 750 MHz antenna. The hyperbolic signature indicates the suspected buried pipe at the depth of 0.16 m. The top of the hyperbolic signature indicates the middle of the buried pipe which is at 5.5 m mark. A 3D augmented view of the interpreted radar section of other traverses at location 2 is presented in Figure 4.10b which shows the continuity of the anomaly.

The 3D GPR have been presented as an interpreted 3D volume in Figure 4.10c(i). The lines perpendicular to the strike of the pipe in the 3D volume have been interpreted which have shown the position of the pipe in the investigated area (Figure 4.10c(ii)).

The interpreted time slice of the 3D GPR at 0.1m interval is presented in Figure 4.10d. The time slice at 0.15m shows the buried pipe indicated by the yellow box, distinctively.

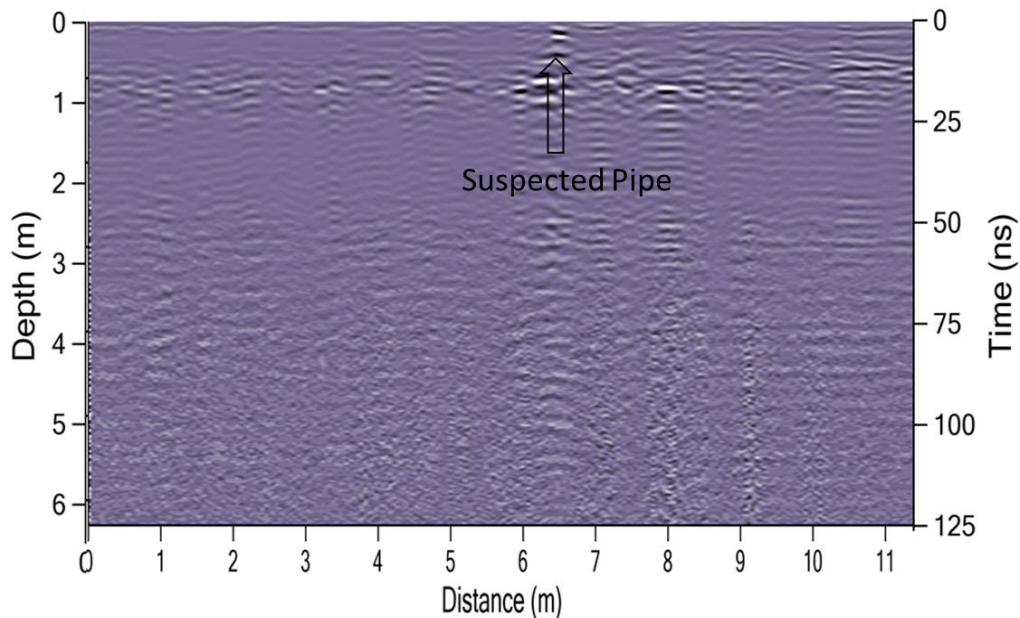


Figure 4.10a Interpreted GPR radargram using the 750 MHz antenna along traverse 1 at Location 2.

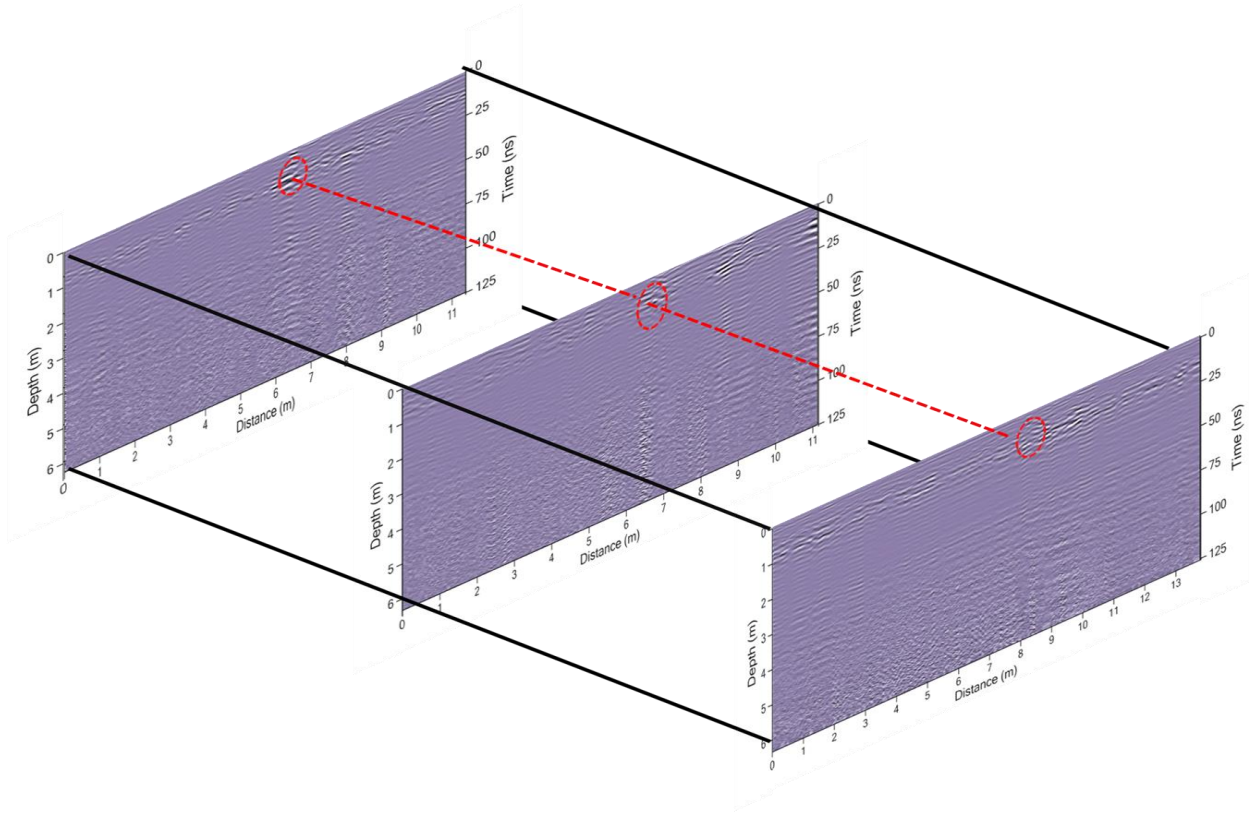


Figure 4.10b Augmented 3D view of the GPR radagram for Location 2.

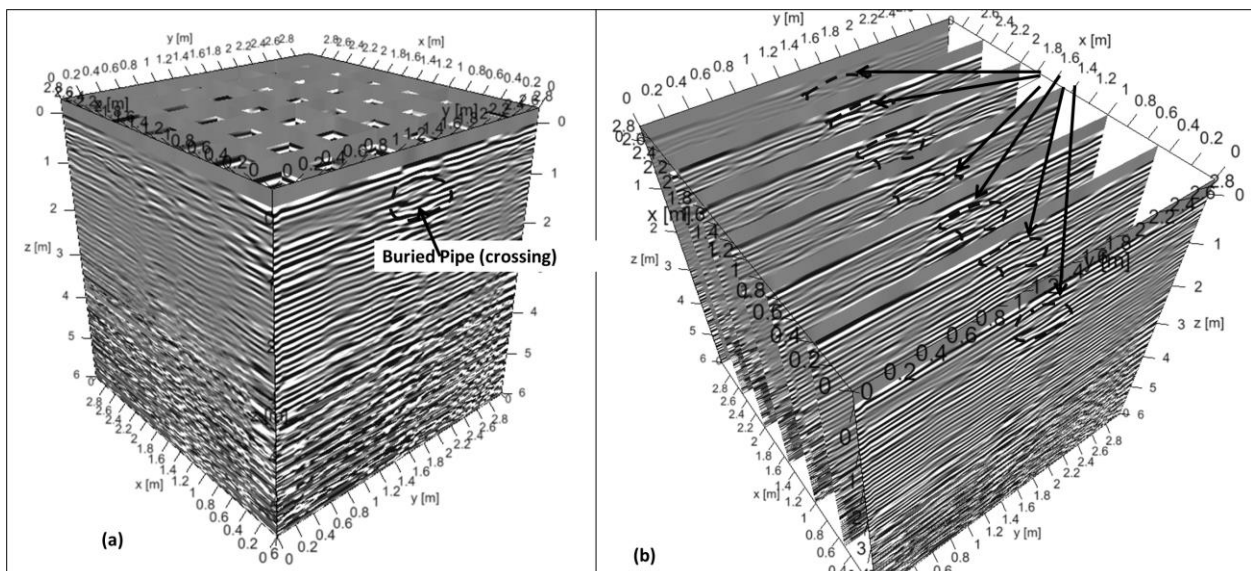


Figure 4.10c Interpreted 3D GPR (i) volume and (ii) dip lines at Location 2

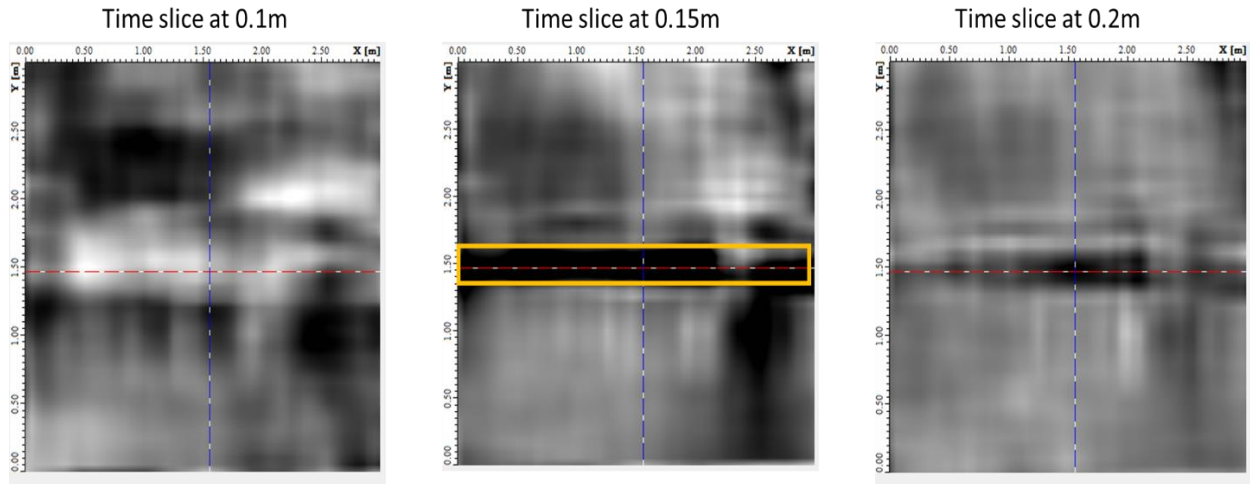


Figure 4.10d Interpreted Time slices of 3D GPR for Location 2.

Location 3

At this location, the result of the GPR obtained using the 750 MHz (Figure 4.11a) show two buried pipes at the depth of 0.31 m and 0.18m respectively. The top of the hyperbolic signatures indicate the middle of the buried pipes at 32 m and 55 m mark respectively. Therefore, the pipes are estimated to be 23 m apart. Figure 4.11b presents an augmented 3D view of the radargram obtained along the traverses.

The 3D GPR have been presented as an interpreted 3D volume in Figure 4.11c(i). The lines perpendicular to the strike of the pipe in the 3D volume have been interpreted which have shown the position of the pipe in the investigated area (Figure 4.9c(ii)).

Figure 4.11d shows the time slice 0.1 interval of the 3D GPR that was carried out. The time slice at 0.2m shows the pipe 2 indicated by the yellow box, distinctively

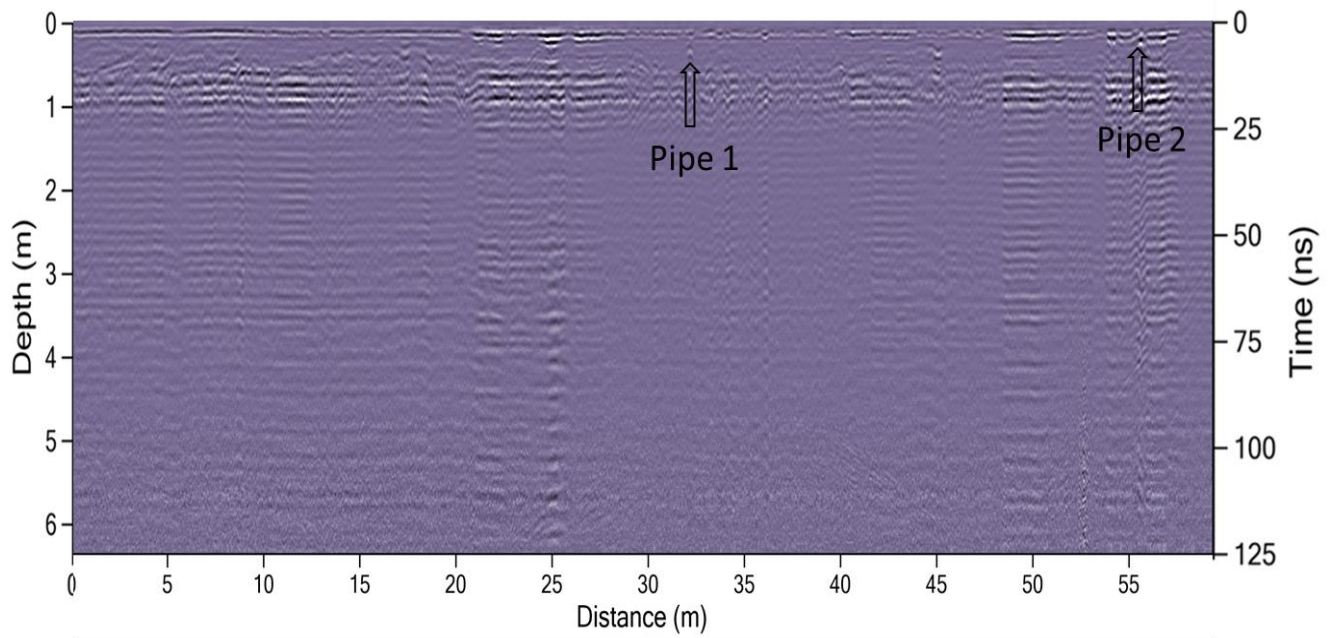


Figure 4.11a Interpreted GPR radargram using the 750 MHz antenna along traverse 1 at Location 3.

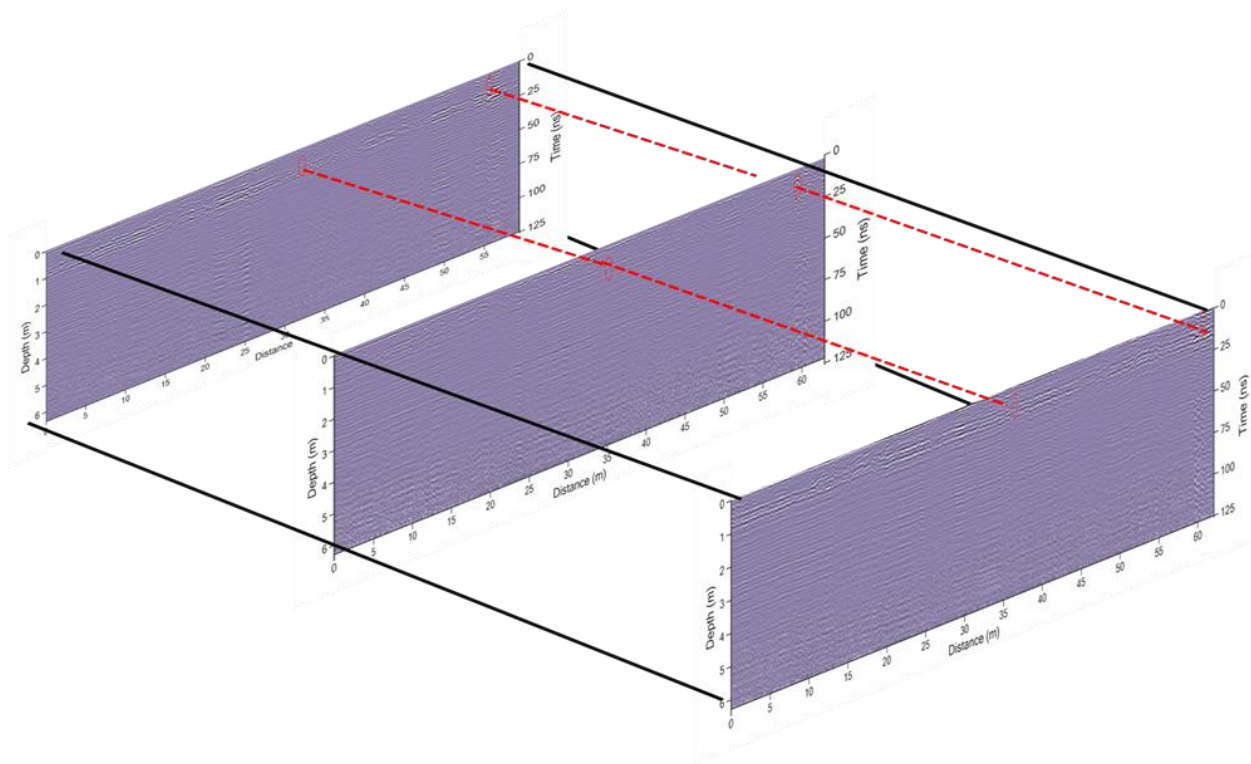


Figure 4.11b Augmented 3D view of the GPR radargram for Location 3.

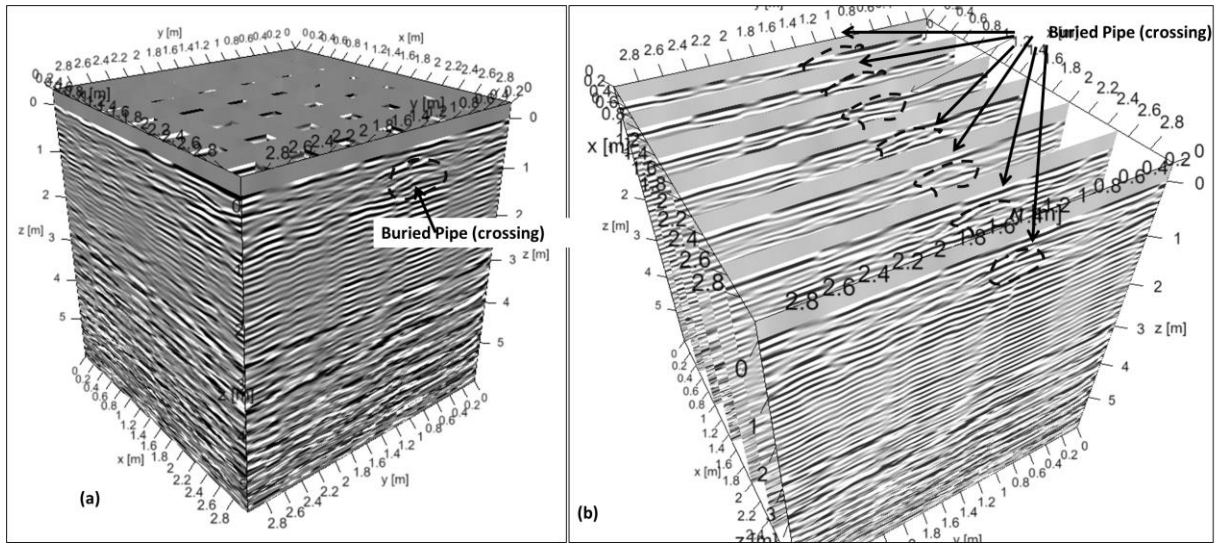


Figure 4.11c Interpreted 3D GPR (i) volume and (ii) dip lines at Location 3

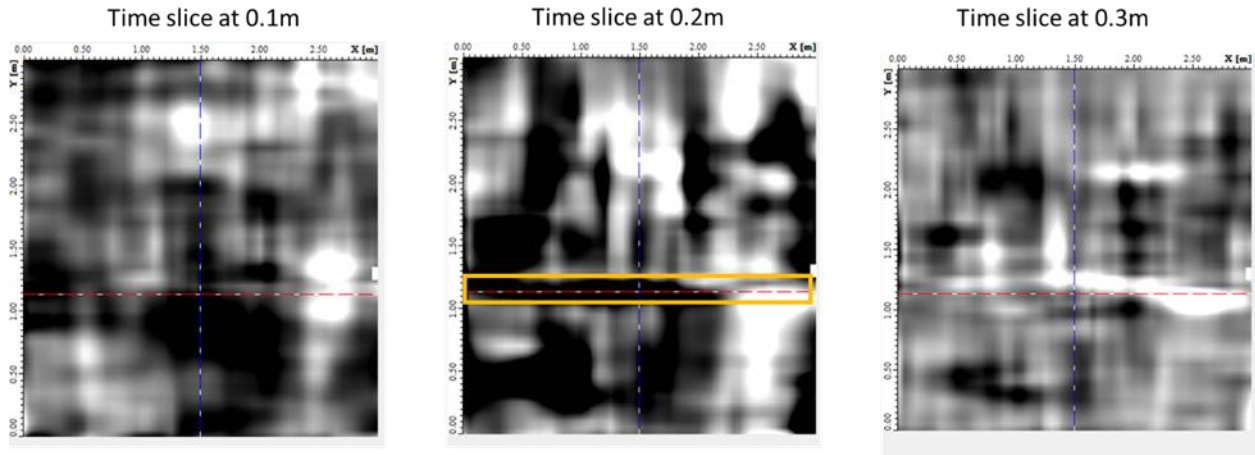


Figure 4.11d 3D GPR Time slice for pipe 2, Location 3.

4.4 Integration of methods

The geophysical methods deployed have been integrated to appraise the consistency of the results.

Location 1

The 2D resistivity inverted section in Figure 4.12a indicates that the buried pipe is located at the depth of 0.2 m from the surface and lateral extent of 0.22 m wide. The interpretation obtained from the radargram (Figure 4.12b) correlates with the 2D ERT section and shows that the pipe is buried at the depth of approximately 0.2 m from the surface.

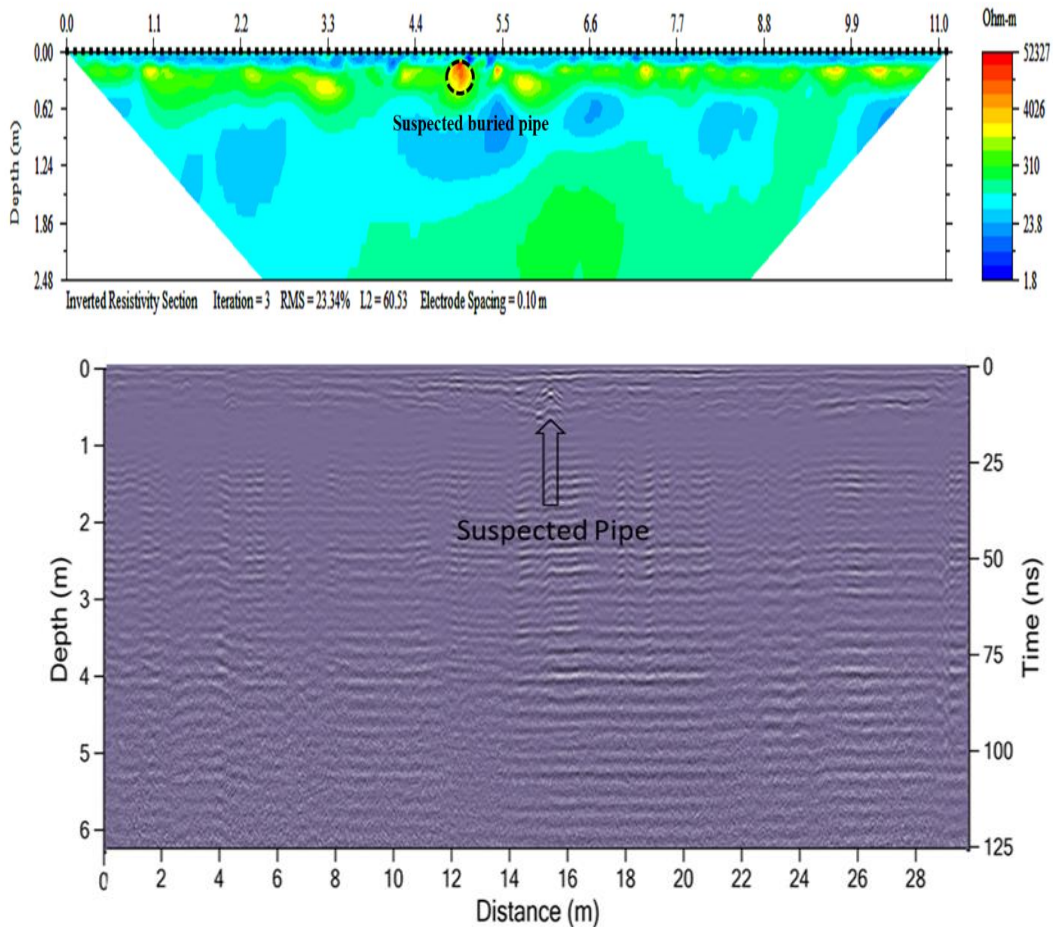


Figure 4.12 A comparison of interpreted results of a.) the final resistivity model and b.) 750 MHz GPR antenna for traverse 1 at Location 1.

Location 2

The 2D resistivity inverted section in Figure 4.13a indicates that the buried pipe is located at a depth 0.16m from the surface and 0.28 m wide. The radargram in Figure 4.13b on the other hand, indicates that the pipe is buried the depth of about 0.16 m from the surface. It also indicates that the buried pipe is located at 5.5 m mark along the traverse from the beginning.

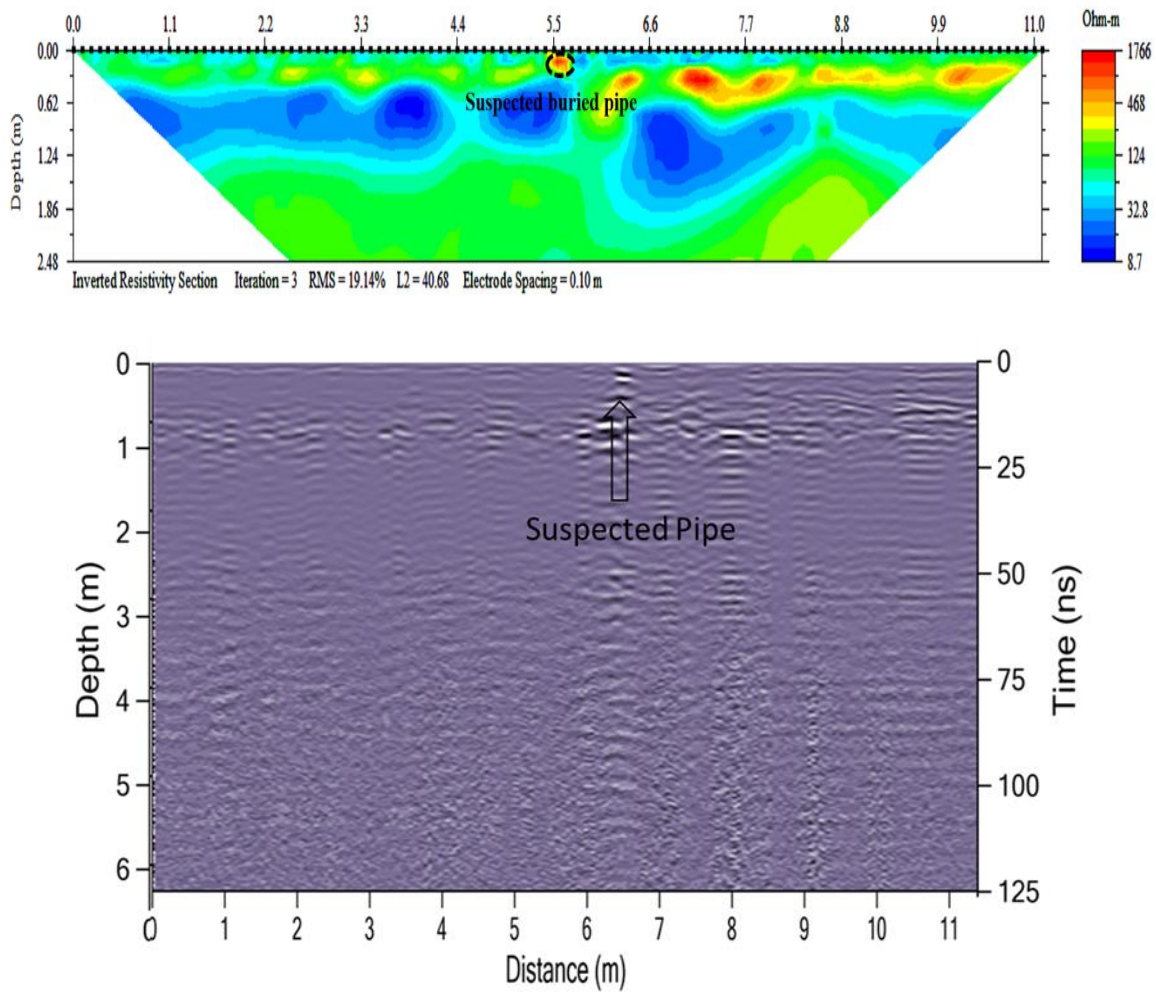


Figure 4.13 A comparison of interpreted results of a.) the final resistivity model and b.) 750 MHz GPR antenna for traverse 1 at Location 2.

Location 3

The 2D resistivity inverted section in Figure 4.14a indicates that pipe 1 is buried at the depth of about 0.29 m from the surface and lateral extent of about 0.29 m wide. Figure 4.14b indicates that pipe 2 is buried at the depth of 0.18m. The radargram in Figure 4.14c confirms that pipe 1 and pipe 2 are buried at the depth of about 0.31 m and 0.18 m respectively from the surface. It also indicates that pipe 1 and pipe 2 are located at 32 m and 55 m mark respectively along the traverse from the beginning.

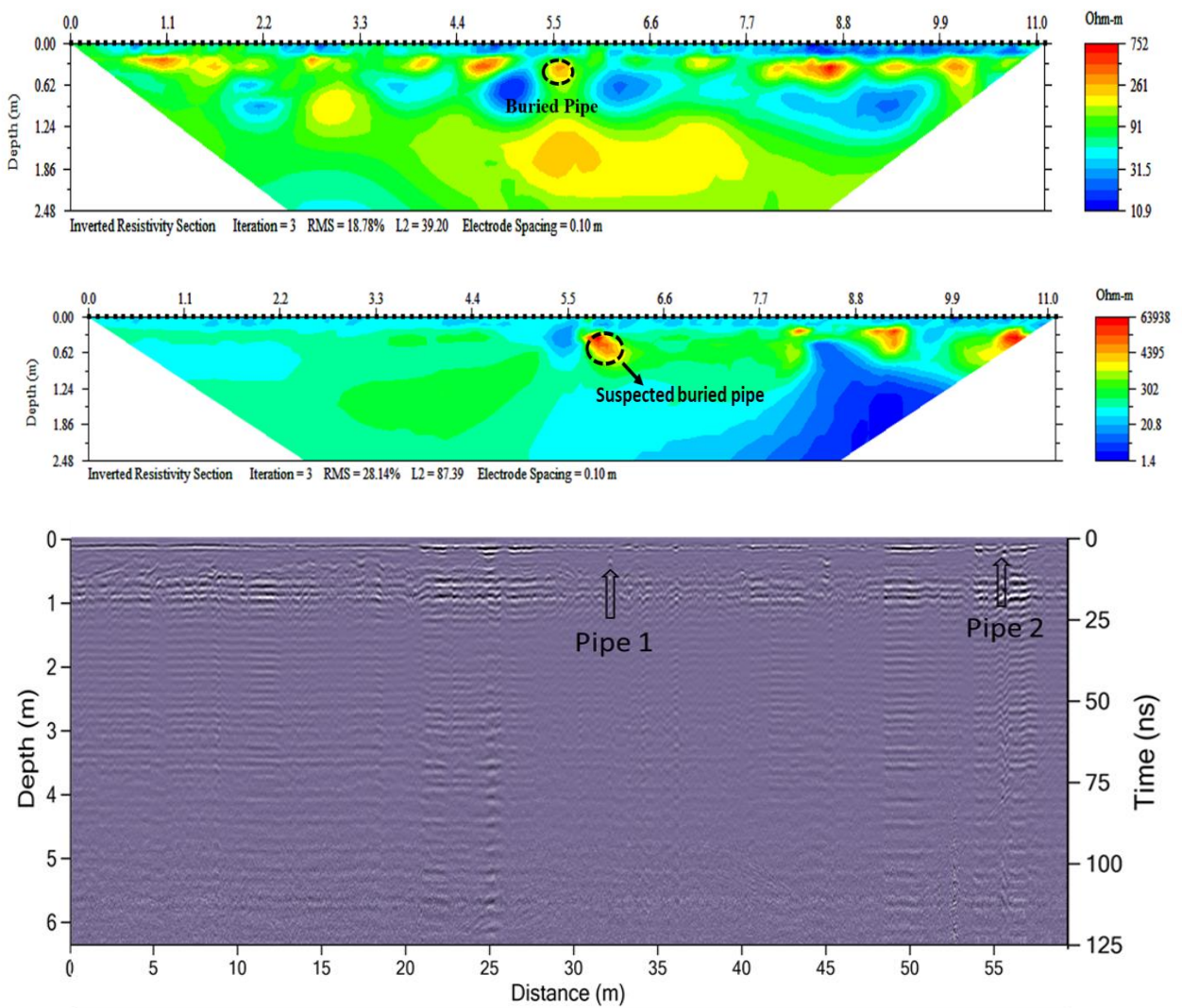


Figure 4.14 A comparison of interpreted results of a.) the final resistivity model for pipe 1 b.) the final resistivity model for pipe 2 and c.) 750 MHz GPR antenna for traverse 1 at Location 3.

CHAPTER FIVE

CONCLUSION AND RECOMMENDATION

5.1 Conclusion

An integrated geophysical survey involving magnetic, 2D ERT, and GPR were used to collect data that provides information about the location, lateral extent and depth of buried utilities at selected area within Mountain Top University. From the result gathered, the buried pipes were detected are suspected to be plastic pipes which was further subjected to ground confirmation. Although, magnetic method is not consistent in the detection of the buried plastic pipes, 2D ERT and GPR have proven to show significant anomalies that are consistent in delineating the buried plastic pipes with different level of precision.

Magnetic survey at location 3 indicated a conspicuous magnetic low approximately 2 m wide. The conspicuous magnetic low was interpreted as a geologic structure relating to a buried stream/river channel which is conspicuous as a visible depression on the ground.

On the 2D ERT, the pipeline is represented by relatively high electrical resistivity value range of 700 to 100k Ω m. The high resistivity contrast is suggestive of air-filled plastic pipes. The pipeline has shown hyperbolic anomalies on the GPR and have been more pronounced on the 3D GPR time slice as lineament features.

Based on the interpretation of the 2D ERT model sections and radargram, the depth to the top of the buried pipe in location 1 is approximately 0.2 m, and 0.2 m wide. At location 2, the depth of the buried pipe detected and its lateral extent is approximately 0.16 m and 0.28 m respectively. Lastly, the results obtained at location 3 reveals that pipe 1 and pipe 2 are buried approximately at the depth of 0.31 m and 0.2 m respectively with respective diameter of 0.28 m and 0.25 m.

The result of this study further corroborates the fact that the integration of 2D ERT and GPR surveys allows for a better identification of buried utilities.

5.2 Recommendation

To prevent damages of buried utilities during construction and renovation at other part of Mountain Top University, more geophysical survey should be carried out to delineate other buried utilities such as fibre cables, electric cables, water pipes and similar utilities. As built map can be developed for buried utilities within the university campus which will serve as guide for construction works and can be updated as more facilities are installed.

2D ERT (with small electrode spacing for high resolution) and GPR (with high frequency) is recommended for detection of buried utilities.

REFERENCES

- Allred BJ, Fausey NR, Peters L Jr, Chen C, Daniels JJ, Youn H (2004) Detection of buried agricultural drainage pipe with geophysical methods. *Appl Eng Agric* 20(3):307–318
- Archie, G.E. (1942). The Electrical Resistivity Log as an Aid in Determining Some Reservoir Characteristics. *Transactions of the AIME*, 146, 54-62.
- Bharti AK, Pal SK, Priyam P, Kumar S, Shalivahan S, Yadav PK (2016a) Subsurface cavity detection over Patherdih colliery, Jharia coalfield, India using electrical resistivity tomography. *Environ Earth Sci* 75(5):443. <https://doi.org/10.1007/s12665-015-5025-z>
- Billman HG (1976) Offshore Stratigraphy and Paleontology of the Dahomey Embayment. *Proceedings, 7th African micropaleontology colloquium, Ile-Ife.*
- Billman HG (1992) Offshore stratigraphy and paleontology of Dahomey (Benin) Embayment. *Nigerian Association of Petroleum Explorationists Bulletin* 70(2): 121-130.
- Binley, A., G. Cassiani, R. Middleton, and P. Winship, 2002, Vadose zone flow model parameterisation using cross-borehole radar and resistivity imaging: *Journal of Hydrology*, 267, 147-159.
- Cardarelli E, Marrone C, Orlando L (2003) Evaluation of tunnel stability using integrated geophysical methods. *J Appl Geophys* 52:93–102. [https://doi.org/10.1016/50926-9851\(02\)00242-2](https://doi.org/10.1016/50926-9851(02)00242-2)
- Cardarelli E, Di Filippo G (2009) Integrated geophysical methods for the characterization of an archaeological site (Massenzio Basilica-Roman forum, Rome, Italy). *J Appl Geophys* 68:508–521

- Cardarelli E, Cercato M, Cerreto A, Di Filippo G (2010) Electrical resistivity and seismic refraction tomography to detect buried cavities. *Geophysics Prospect* 58:685–695. <https://doi.org/10.1111/1/j.1365-2478.2009.00854.x>
- Cardarelli E, Cercato M, De Donno G, Di Filippo G (2014) Detection and imaging of piping sinkhole by integrated geophysical methods. *Near Surf Geophys* 12:439–450. <https://doi.org/10.3997/1873-0604.2013051>
- Coker SJL (2002) Field excursion guide to tar sand outcrops in Benin Basin. Nigerian Association of Petroleum Explorationists, MiniConference, pp. 32.
- Daily, W., A. Ramirez, and R. Johnson, 1998, Electrical impedance tomography of a perchloroethylene release: *Journal of Environmental and Engineering Geophysics*, 2, 189-201.
- Daily, W., and A. L. Ramirez, 2000, Electrical imaging of engineered hydraulic barriers: *Geophysics*, 65, 83-94.
- Daniels, J., Roberts, R., and Vendl, M., 1995, Ground penetrating radar for the detection of liquid contaminants: *Journal of Applied Geophysics*, v. 33, p. 195–207, doi: 10.1016/0926-9851(94)00033-K.
- Goes, B. J. M., and J. A. C. Meeke, 2004, An effective electrode configuration for the detection of DNAPLs with electrical resistivity tomography: *Journal of Environmental and Engineering Geophysics*, 9, 127-141.
- Hazreek ZAM, Nizan ZM, Azhar ATS, Aziman M, Shaylinda MZN (2016) Physical modeling on detecting buried object using electrical resistivity imaging (ERI). 1OP Conference Series.

- Materials Science and Engineering, 136, 1–10: 01, 2008. Doi:10.1088/1757-899x/136/1/012008.
- Jones HA, Hockey RD (1964) The Geology of part of Southwestern Nigeria. Geological Survey of Nigeria Bulletin 31: 101.
- Kearey P., Brooks M., Hill I., (2002). “*An Introduction to Geophysical Exploration*”, 3rd ed. Blackwell Science, Oxford.
- Keller, G. V., and Frischknecht, F. C. (1966). *Electrical Methods in Geophysical Prospecting*. Oxford: Pergamon.
- Mahato PP (2018) Detection of cavity using electrical resistivity tomography (ERT) at Patherdih, Jharia coal field, Dhanbad, India. *Univ J Geosci* 6(4):114–117. <https://doi.org/10.13189/ujg.2018.060402>.
- Meads, L. N., L. R. Bentley, and C. A. Mendoza, 2003, Application of electrical resistivity imaging to the development of a geologic model for a proposed Edmonton landfill site: *Canadian Geotechnical Journal*, 40, 551-558.
- Metwaly M, Al Fouzau F (2013) Application of 2D geoelectrical resistivity tomography for subsurface cavity detection in the eastern part of Saudi Arabia. *Geosci Front* 4:469–476. <https://doi.org/10.1016/j.gef.2012.12.005>.
- Michot D (2003) Spatial and temporal monitoring of soil water content with an irrigated corn crop cover using surface electrical resistivity tomography. *Water Resour Res.* <https://doi.org/10.1029/2002WR001581>.

- Mishra RK, Roy PNS, Singh VK, Pandey JK (2018) Detection and delineation of coal mine fire in Jharia coalfield, India using geophysical approach: A case study. *J Earth Syst Sci* 127:107. <https://doi.org/10.1007/s12040-018-1010-8>
- Mochales T, Casas AM, Pueyo EL, Pueyo O, Roman MT (2008) Detection of underground cavities by combining gravity, magnetic and ground penetrating radar surveys: a case study from the Zaragoza Area, NE Spain. *Environ Geol* 53:1067–1077. <https://doi.org/10.1007/S00254-007-0733/>
- Neal P. Kerrigan (2013). Using Shallow Geophysical Methods to Locate a Buried Stream Channel at a Stream Restoration Site in the Burd Run Watershed, Shippensburg, PA.
- Obaje NG (2009) *Geology and Mineral Resources of Nigeria*. SpringerVerlag Berlin Heidelberg, pp. 13-108.
- Okosun EA (1990) A review of the Cretaceous stratigraphy of the Dahomey Embayment, West Africa. *Cretaceous Res* 11(1): 17-27.
- Olabode SO, Mohammed MZ (2016) Depositional Facies and Sequence Stratigraphic Study in Parts of Benin (Dahomey) Basin SW Nigeria: Implications on the Re-Interpretation of Tertiary Sedimentary Successions. *International Journal of Geosciences* 7: 210-228.
- Olorunfemi, M. O. and Griffiths, D. H., (1985). A laboratory investigation of the induced polarization of the Triassic Sherwood Sandstone of Lancashire and its hydrogeological application: *Geophys. Prospect.*, v. 32, p.
- Omatsola ME, Adegoke OS (1981) Tectonic evolution and Cretaceous stratigraphy of the Dahomey Basin. *J Mining Geol* 18: 130-137.

- Oyedepo, J.A., Shittu, O.B., Popoola, T.O.S and Ogunshola, E.O. (2013) Rapid epidemiological mappin of cholera outbreak in parts of Abeokuta metropolis: A GIS-supported post-epidemic assessment. *International Journal of Public Health and Epidemology* ISSN:2326-7291 Vol. 4(6), pp. 152-157.
- Pazzi V, Ceccatelli M, Gracchi T, Masi EB, Fanti R (2018) Assessing subsoil void hazards along a road system using H/V measurements, ERTs and IPTs to support local decision makers. *Near Surf Geophys* 16:282–297. <https://doi.org/10.3997/1873-0604.2018002>.
- Patnode H.W and Wyllie M.R.J., (1950). Application of electrical resistivity measurement for the determination of porosity and permeability in sand-stones, Vol 14, Issue 3 – 4. [https://doi.org/10.1010/0016-7142\(76\)90014-4](https://doi.org/10.1010/0016-7142(76)90014-4)
- Pueyo Anchuella O, Pocovi Juan A, Casas- Sainz AM, Anson-Lopez D, Gill-Garbi H (2013) Actual extension of sinkholes; considerations about geophysical, geomorphological and field inspection techniques in urban planning projects in the Ebro basin (NE Spain). *Geomorphology* 189:135–149.
- Ramirez A, Daily W, Binley A, LaBrecque D, Roelent D (1996) Detection of leaks in underground storage tanks using electrical resistance methods. *J Environ Eng Geophys* 1:189–203.
- Reynolds, J.M. (2011), “*An Introduction to Applied and Environmental Geophysics*”, Second Edition, John Wiley & Sons Ltd.
- Rehman F, Abouelnaga HSO, Rehman F (2016) Estimation of dielectric permittivity, water content and porosity for environmental engineering and hydrological studies using ground penetrating radar, a short review. *Arab J Geosci* 9:312. <https://doi.org/10.1007/s12517-016-2328-7>.

- Sandberg, S. K., L. D. Slater, and R. Versteeg, 2002, An integrated geophysical investigation of the hydrogeology of an anisotropic unconfined aquifer: *Journal of Hydrology*, 267, 227-243.
- Sagnard F, Tarel JP (2016) Template-matching based detection of hyperbolas in ground penetrating radargrams for buried utilities. *J Geophys Eng* 13:491–504. <https://doi.org/10.1088/1742-2132/13/4/491>.
- S.A Ganiyu, M.A Oladunjoye, O.I. Onakoya, J.O Olutoki, B.S Badmus (2020) Combined Electrical Resistivity Imaging and Ground Penetrating Radar Study for Detection of Buried Utilities in Federal University of Agriculture, Abeokuta, Nigeria. *Environmental Earth Science* (2020) 79:177. <https://doi.org/10.1007/s12665-020-08919-2>.
- Samouëlian A, Cousin I, Tabbagh A, Bruand A, Richard G (2005) Electrical resistivity survey in soil science: a review. *Soil Tillage Res.* <https://doi.org/10.1016/j.still.2004.10.004>.
- Shah SD, Smith BD, Clark AK, Kress WH.2008. A Multi-Tool Geophysical and Hydrogeological Investigation of a Karst Aquifer System, Cibolo Canyon Development Area, Bexar County, Texas. USGS Scientific Investigations Report 2008-5023.
- Sun H, Cheng M, Su C, Li H, Zhao G, Su M, Li S, Zhang L, Li K (2017) Characterization of shallow karst using electrical resistivity imaging in a limestone mining area. *Environ Earth Sci* 76:767. <https://doi.org/10.1007/s12665-017-7112-9>.
- Telford W.M., Geldart L.P., and Sheriff R.E. (1990), “*Applied Geophysics*”, Second Edition, Cambridge University Press, pages 6-50; 209-240; 353-358.

Ungureanu C, Princeputu A, Buges AL, Chirică A (2017) Use of Electrical Resistivity Tomography (ERT) for detecting underground voids on highly anthropized urban construction sites. Urban subsurface planning and management week, SUB-URBAN 2017, 13–16, March 2017, Bucharest, Romania. *Procedia Eng* 209:202–209. <https://doi.org/10.1016/j.proeng.2017.11.148>.

Xu X, Miller EL, Rappaport CM, Sower GD (2002) Statistical method to detect subsurface objects using array ground-penetrating radar data: geosciences and remote sensing. *IEEE Trans Geosci Remote Sens* 40(4):963–976.

APPENDIX A

Magnetic Profiles

Location 2

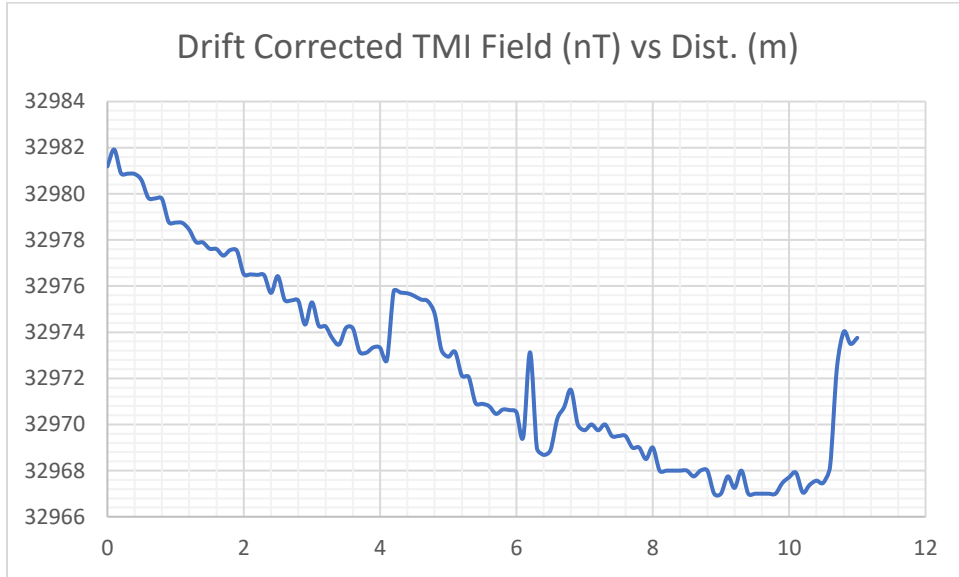


Figure A1: Magnetic profile along traverse 3

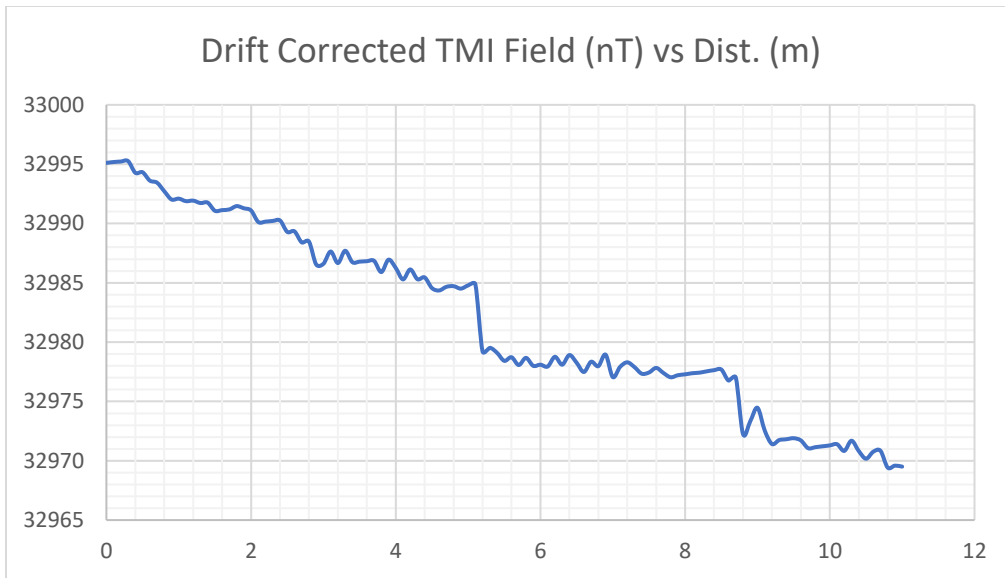


Figure A2: Magnetic profile along traverse 5

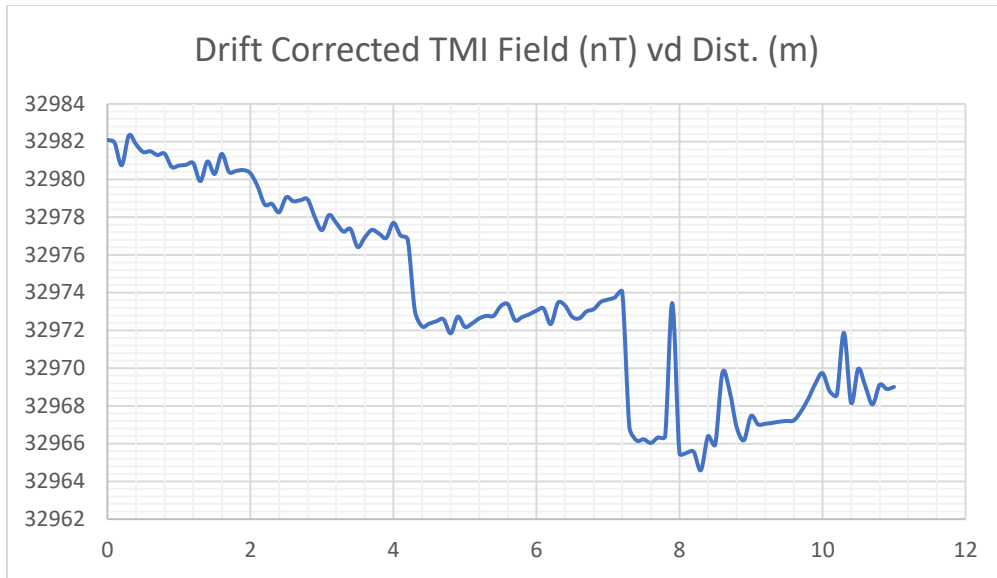


Figure A3: Magnetic profile along traverse 6

Location 3

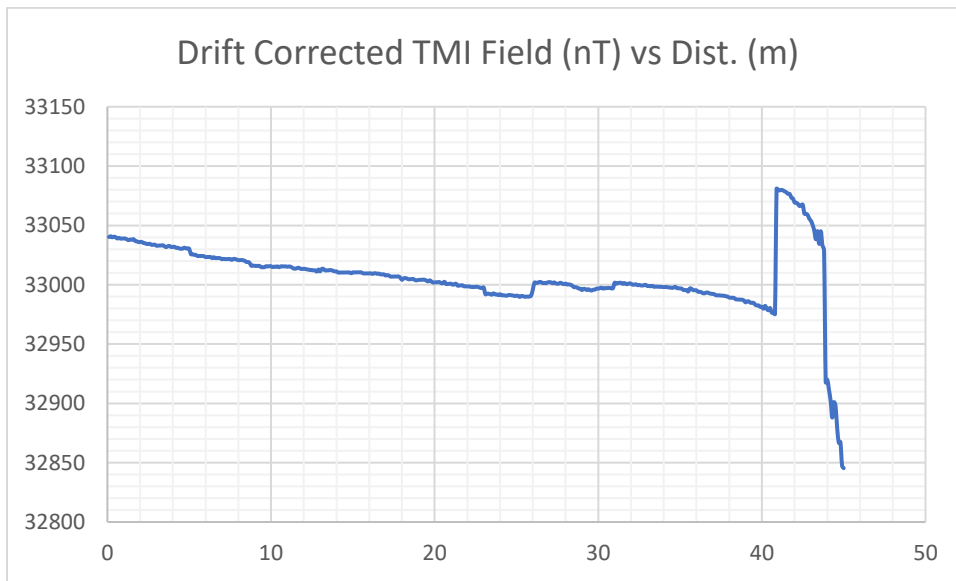


Figure A4: Magnetic profile along traverse 3

Location 1

LINE 1				LINE 2					LINE 3					
SN	Time			TMI (Ave)	SN	Time			TMI (Ave)	SN	Time			TMI (Ave)
	H	M	S			H	M	S			H	M	S	
BS 0	3	1	39	32949	BS1	13	40	30	32951.25	BS 1	1	48	3	32968
1	3	3	18	32938	1	13	43	57	32943.25	1	1	51	10	32961.25
2	3	3	46	32939	2	13	45	10	32941.25	2	1	52	6	32962
3	3	4	19	32939	3					3	1	52	41	32962
4	3	5	5	32939	4	13	48	58	32942	4	1	53	9	32961
5	3	5	29	32939.75	5	13	49	57	32939	5	1	53	58	32961
6	3	6	6	32939.25	6	13	53	4	32940	6	1	54	45	32960
7	3	6	31	32938.75	7	13	53	58	32939.5	7	1	55	16	32960
8	3	7	1	32939	8	13	54	37	32939	8	1	55	45	32959.75
9	3	7	22	32939.25	9	13	56	30	32939	9	1	56	20	32959
10	3	7	50	32938.25	10	13	57	36	32939	10	1	57	11	32959
11	3	8	37	32938.25	11	13	58	31	32940	11	1	57	37	32958.5
12	3	9	54	32939	12	13	59	50	32940	12	1	58	51	32957
13	3	10	23	32938.75	13	14	0	43	32939	13	1	59	22	32957
14	3	10	50	32939	14	14	1	31	32939	14	2	0	4	32956.25
15	3	11	18	32938	15	14	2	23	32939.25	15	2	0	56	32956
16	3	11	47	32937	16	14	4	5	32939	16	2	1	30	32956
17	3	12	13	32937	17	14	4	54	32939	17	2	1	54	32955
18	3	12	59	32937	18	14	6	8	32940	18	2	2	38	32955
19	3	13	25	32936	19	14	7	0	32939	19	2	3	3	32955
20	3	13	56	32936	20	14	8	51	32939	20	2	3	46	32954
21	3	14	19	32937	21	14	9	35	32948	21	2	5	36	32952
22	3	15	4	32936.5	22	14	12	2	32938	22	2	6	8	32952
23	3	15	50	32936.75	23	14	12	56	32938	23	2	6	50	32952
24	3	16	47	32938	24	14	13	30	32938	24	2	7	57	32952
25	3	17	17	32940	25	14	14	4	32937	25	2	8	41	32950.5
26	3	17	45	32941	26	14	15	3	32936	26	2	9	28	32950
27	3	18	23	32939	27	14	15	31	32936	27	2	9	55	32949.75
28	3	18	53	32939.5	28	14	16	5	32936	28	2	10	35	32949
29	3	19	22	32939	29	14	17	8	32935.75	29	2	11	20	32948
30	3	19	51	32937	30	14	17	58	32936	30	2	12	29	32948
31	3	20	32	32937	BS 2	14	20	37	32947	31	2	13	37	32947
32	3	22	13	32937	31	14	28	24	32934	32	2	14	6	32947
33	3	22	48	32934.5	32	14	30	8	32933	33	2	14	37	32947

34	3	23	24	32935	33	14	30	31	32933	34	2	15	56	32946.75
35	3	24	23	32936.75	34	14	31	57	32933	35	2	17	39	32945
36	3	24	54	32938.75	35	14	32	42	32932	36	2	18	49	32945
37	3	25	22	32937.75	36	14	33	22	32931.75	BS 2	2	20	15	8488.5
38	3	25	54	32937	37	14	34	15	32931	BS 3	19	29	29	32934
39	3	26	35	32937	38	14	34	59	32931	35	19	32	0	32916
40	3	27	8	32937.25	39	14	35	57	32931	36	19	32	39	32916
41	3	27	45	32937	40	14	36	57	32931.75	37	19	33	6	32915
42	3	28	16	32939	41	14	37	59	32932	38	19	33	38	32915
43	3	28	53	32937	42	14	40	42	32931	39	19	34	18	32914
44	3	29	29	32938	43	14	42	12	32930.75	40	19	35	3	32915
45	3	30	22	32937	44	14	44	44	32930	41	19	35	28	32914
46	3	31	2	32937	45	14	45	54	32929	42	19	36	8	32914
BS 1	3	32	42	32954	46	14	47	2	32928.75	43	19	36	41	32914
47	3	38	54	32935.75	47	14	49	20	32928	44	19	37	4	32913
48	3	39	29	32936	BS 3	14	52	44	32944	45	19	37	35	32913
49	3	40	9	32935.75	48	14	55	3	32926.25	46	19	38	23	32913
50	3	40	57	32936.25	49	14	55	48	32926.75	47	19	39	12	32913
51	3	41	36	32936.75	50	14	56	58	32927	48	19	39	51	32913
52	3	42	37	32936	51	14	58	8	32927	49	19	40	29	32913
53	3	43	7	32936	52	14	58	39	32926	50	19	41	6	32913
54	3	43	49	32936	53	14	59	12	32927	51	19	41	33	32912
55	3	44	16	32935.75	54	15	0	50	32925.75	52	19	42	28	32912
56	3	44	45	32935	55	15	2	3	32925	53	19	43	0	32912
57	3	45	27	32937	56	15	2	51	32925	54	19	43	34	32912
58	3	46	4	32935.5	57	15	4	0	32925	55	19	44	0	32912
59	3	46	54	32935	58	15	4	27	32924	56	19	44	23	32912
60	3	47	24	32936	59	15	6	27	32923	57	19	45	21	32912
61	3	48	13	32936	60	15	7	35	32924	58	19	45	48	32912
62	3	48	42	32936	61	15	8	49	32922	59	19	46	24	32912.25
63	3	49	35	32935	62	15	10	36	32922	60	19	46	57	32912
64	3	50	33	32936	63	15	13	9	32922	61	19	47	43	32912
65	3	51	6	32936	64	15	13	41	32922	62	19	48	8	32912
66	3	51	38	32935.75	65	15	16	9	32922	63	19	48	35	32912
67	3	52	23	32937	66	15	17	21	32922	64	19	48	58	32912
68	3	53	5	32935	67	15	18	21	32922	65	19	49	35	32912
69	3	53	39	32936	68	15	19	10	32922	66	19	50	31	32913
70	3	54	23	32937.25	69	15	19	37	32922	67	19	51	15	32913
71	3	55	16	32935	70	15	20	54	32921.5	68	19	51	45	32913

72	3	55	49	32934.75	71	15	21	32	32920.75	69	19	52	16	32913
73	3	56	23	32935	72	15	24	42	32921	70	19	52	50	32912.25
74	3	58	29	32936	BS 4	15	26	56	32940	71	19	53	20	32913
75	3	59	5	32936	73	15	34	30	32919.25	72	19	54	2	32913
76	3	59	35	32936	74	15	35	56	32919	73	19	54	29	32913
77	4	0	14	32937	75	15	36	42	32919	74	19	54	56	32913.25
78	4	1	14	32938	76	15	37	28	32918.75	75	19	55	43	32914
79	4	2	18	32939	77	15	38	7	32919	76	19	56	11	32914
80	4	3	5	32938.25	78	15	38	43	32918	77	19	56	40	32914
81	4	4	2	32940	79	15	39	26	32918	78	19	57	9	32914
82	4	6	48	32939	80	15	40	5	32918	79	19	58	17	32914.75
83	4	7	22	32940	81	15	40	54	32918	80	19	58	52	32915
84	4	7	51	32938	82	15	41	31	32918	81	19	59	22	32914.5
85	4	8	27	32939	83	15	42	41	32918.25	BS 4	20	0	53	32937
86	4	9	20	32939	84	15	43	48	32917.5	82	20	2	27	32915
87	4	10	10	32938.5	85	15	44	43	32917.5	83	20	3	2	32914.75
88	4	10	37	32939	86	15	45	30	32917	84	20	3	32	32914.5
BS 2	4	12	18	32955	87	15	46	8	32917.25	85	20	5	2	32915.75
89	4	13	36	32937	88	15	48	11	32918.25	86	20	5	48	32915.25
90	4	14	6	32937	89	15	49	15	32918	87	20	6	19	32916
91	4	14	36	32939	90	15	50	42	32918.25	88	20	6	50	32915
92	4	15	4	32937	91	15	53	47	32918	89	20	7	56	32916
93	4	15	37	32936	92	15	55	18	32918	90	20	8	59	32915.5
94	4	16	31	32938	93	15	56	39	32918.5	91	20	9	33	32916
95	4	17	25	32937.25	BS 5	15	58	8	32936	92	20	10	24	32916
96	4	18	12	32937	94	16	0	28	32917.75	93	20	11	0	32916
97	4	19	6	32936	95	16	1	15	32918	94	20	11	32	32916
98	4	19	54	32936	96	16	2	8	32918	95	20	13	11	32917
99	4	20	28	32936	97	16	2	42	32918.25	96	20	13	49	32917
100	4	21	11	32935	98	16	3	30	32918	97	20	14	27	32917
101	4	22	5	32935.75	99	16	4	38	32918	98	20	15	10	32918
102	4	22	36	32935.25	100	16	6	20	32918	99	20	15	48	32918
103	4	23	6	32935	101	16	8	31	32917.5	100	20	16	37	32919
104	4	23	44	32935	102	16	10	55	32917	101	20	17	27	32919
105	4	24	22	32935	103	16	14	31	32916	102	20	17	52	32919
106	4	24	45	32935	104	16	16	43	32916.25	103	20	18	20	32919
107	4	25	46	32935	105	16	20	25	32915.75	104	20	18	43	32919
108	4	26	15	32935.75	106	16	21	6	32916.5	105	20	19	24	32919
109	4	27	6	32933	107	16	24	5	32914	106	20	20	25	32920

110	4	28	5	32933	108	16	27	9	32911.25	107	20	20	58	32920
111	4	28	38	32933.5	109	16	29	6	32910.75	108	20	21	49	32920
112	4	29	33	32934	BS 6	16	31	1	32929	109	20	22	22	32921
113	4	30	3	32933	110	16	32	46	32911	110	20	23	15	32922
114	4	30	38	32932.75	111	16	33	51	32911	111	20	23	44	32921
115	4	31	8	32933	112	16	34	35	32911	112	20	24	34	32921
116	4	32	43	32930.25	113	16	35	25	32911	113	20	25	40	32921
117	4	33	15	32931	114	16	36	14	32911	114	20	27	34	32922
118	4	33	49	32930	115	16	36	43	32910.75	115	20	28	35	32923
119	4	35	11	32931	116	16	38	37	32911	116	20	29	35	32922
120	4	35	52	32929.5	117	16	39	16	32911	117	20	30	5	32923
121	4	36	37	32929.75	118	16	40	7	32911	BS 5	20	31	31	32937
122	4	37	33	32929	119	16	40	39	32911	BS 6	21	13	15	32939
123	4	38	13	32930	120	16	41	27	32911	118	21	15	31	32923
124	4	38	51	32929	121	16	42	3	32911	119	21	16	33	32924
125	4	40	27	32928	122	16	42	34	32911	120	21	16	55	32925
126	4	41	4	32926	123	16	43	3	32911	121	21	17	23	32925
127	4	41	36	32926	124	16	43	56	32910.75	122	21	18	12	32926
128	4	42	25	32926.25	125	16	44	57	32911	123	21	18	54	32926.75
129	4	43	5	32925.25	126	16	45	37	32910.25	124	21	19	24	32926
130	4	44	29	32925.25	127	16	46	26	32911.25	125	21	20	23	32926.5
BS 3	4	45	38	32951	128	16	47	9	32911.5	126	21	21	0	32927
BS 4	21	13	14	32962	129	16	47	49	32911.75	127	21	21	52	32926
131	21	14	36	32938	130	16	48	57	32911.5	128	21	22	18	32927
132	21	15	10	32937	131	16	49	18	32911	129	21	23	7	32926
133	21	15	37	32937	132	16	49	59	32911.75	130	21	23	39	32927
134	21	16	16	32936	133	16	51	54	32912	131	21	24	48	32927
135	21	17	29	32936	134	16	53	47	32911	132	21	25	22	32927
136	21	18	11	32935.75	135	16	54	34	32912	133	21	26	50	32925.75
137	21	19	43	32936	136	16	55	16	32911	134	21	27	32	32927
138	21	19	6	32935	137	16	56	10	32911	135	21	28	27	32925
139	21	19	32	32935	138	16	56	41	32911	136	21	29	14	32925.75
140	21	20	55	32935	139	16	57	17	32911	137	21	30	16	32927
141	21	21	40	32935	140	16	57	55	32911	138	21	31	18	32926
142	21	21	4	32935	141	16	58	26	32911	139	21	32	7	32927
143	21	22	28	32935	142	16	59	7	32911	140	21	32	36	32926.5
144	21	22	5	32935	143	17	0	32	32910.5	141	21	33	16	32927
145	21	22	19	32935	144	17	1	52	32911	142	21	34	10	32927
146	21	23	19	32934	BS 7	17	3	50	32930	143	21	35	0	32927

147	21	23	53	32934	145	17	6	10	32911	144	21	36	4	32927
148	21	24	27	32934	146	17	8	2	32911	145	21	36	40	32927
149	21	25	14	32934	147	17	8	53	32910.5	146	21	37	36	32926.75
150	21	26	17	32933	148	17	9	44	32910	147	21	38	8	32926
151	21	27	42	32933	149	17	10	35	32910	148	21	39	4	32926
152	21	27	59	32931.75	150	17	12	0	32910	149	21	39	46	32925
153	21	28	56	32932	151	17	14	36	32909	150	21	40	21	32925
154	21	29	24	32931	152	17	18	17	32909	151	21	40	56	32924
155	21	29	56	32932	BS 8	17	22	36	32931	152	21	41	47	32925
156	21	30	28	32931	BS 9	9	44	18	32957	153	21	42	16	32925
157	21	31	1	32932	150	9	49	45	32936	154	21	42	46	32925
158	21	31	31	32931	151	9	50	48	32937	155	21	43	13	32925
159	21	31	57	32931	152	9	51	58	32936	BS 7	21	44	35	32939
160	21	32	37	32931	153	9	52	18	32937	156	21	45	48	32924
161	21	33	7	32931	154	9	54	0	32936	157	21	46	17	32925.75
162	21	34	12	32930	155	9	54	46	32935	158	21	47	14	32924
163	21	34	4	32930	156	9	55	31	32935	159	21	47	45	32925
164	21	35	29	32930	157	9	56	3	32936	160	21	48	31	32924.75
165	21	35	57	32931	158	9	56	40	32935.75	161	21	50	20	32925
166	21	36	21	32931	159	9	57	33	32935	162	21	51	1	32924
167	21	36	46	32931	160	9	58	0	32935	163	21	51	56	32924
168	21	37	13	32930	161	9	58	46	32934	164	21	52	23	32925
169	21	37	39	32930	162	9	59	17	32934.5	165	21	53	5	32926
170	21	38	34	32930	163	10	0	1	32934	166	21	54	6	32927
171	21	41	25	32930.75	164	10	5	47	32935	167	21	54	44	32924
172	21	42	18	32930.75	165	10	8	9	32935	168	21	55	19	32925
173	21	43	10	32930	166	10	11	47	32935.5	169	21	55	53	32925
174	21	43	43	32930	167	10	12	14	32936	170	21	56	56	32925.75
BS 5	21	44	57	32964	168	10	15	13	32936	171	21	58	29	32926
175	21	45	52	32930	169	10	18	49	32936	172	21	59	23	32926.75
176	21	46	21	32930.25	BS 10	10	21	29	32961.75	173	22	0	21	32926
177	21	47	15	32929	170	10	23	44	32936.75	174	22	2	26	32927
178	21	48	21	32930	171	10	26	45	32937	175	22	3	0	32926
179	21	49	8	32930	172	10	29	16	32937.75	176	22	3	35	32927
180	21	49	38	32931	173	10	31	49	32937.25	177	22	4	8	32926.75
181	21	50	12	32931	174	10	35	25	32939	178	22	5	2	32927
182	21	50	42	32931	175	10	36	17	32938.75	179	22	6	21	32930
183	21	51	28	32931	176	10	39	1	32940	180	22	6	56	32927
184	21	51	50	32930	177	10	40	45	32940	181	22	7	33	32927

185	21	52	15	32930	178	10	46	48	32940	182	22	8	21	32927
186	21	53	7	32930.75	BS 11	11	30	55	32970	183	22	9	30	32928
187	21	53	34	32931	179	11	33	52	32946.25	184	22	10	11	32928
188	21	54	21	32931	180	11	37	0	32947	185	22	11	29	32930
189	21	54	49	32932	181	11	38	3	32947	186	22	12	8	32930
190	21	55	21	32932	182	11	38	55	32946.75	187	22	12	43	32929
191	21	56	35	32931.25	183	11	39	37	32947	188	22	13	39	32930
192	21	56	53	32932	184	11	40	47	32937	189	22	14	9	32929
193	21	57	43	32932	185	11	42	0	32947.25	190	22	14	43	32931
194	21	58	8	32933	186	11	43	30	32948	191	22	15	32	32930
195	21	59	34	32933	187	11	45	11	32947	BS 8	22	16	59	32940.25
196	22	0	1	32933	188	11	45	47	32947	202	22	18	28	32934
197	22	0	30	32933	189	11	47	12	32948	203	22	18	57	32933.75
198	22	0	56	32933	190	11	51	21	32938	204	22	19	49	32934
199	22	1	22	32933	191	11	52	2	32948	205	22	20	33	32933
200	22	1	51	32933	192	11	53	14	32949	206	22	21	2	32932.5
201	22	2	22	32934	193	11	54	53	32947	207	22	22	19	32933
202	22	2	56	32934	194	11	55	30	32947.75	208	22	22	57	32933
203	22	3	42	32934	195	11	56	20	32947.75	209	22	23	40	32932
204	22	4	27	32934	196	11	57	1	32948	210	22	25	13	32932
205	22	5	7	32934	197	11	58	42	32948	211	22	25	59	32933
206	22	5	39	32934	198	11	59	43	32948.75	212	22	26	30	32933
207	22	6	4	32935	199	12	0	17	32949	213	22	27	4	32932
208	22	6	51	32935.5	BS 12	12	1	56	32972	214	22	27	58	32932
209	22	7	49	32935.25	200	12	3	1	32948.25	215	22	28	43	32932
210	22	8	38	32936	201	12	3	51	32949	216	22	29	16	32931.25
211	22	9	9	32936.25	202	12	4	38	32949	217	22	29	48	32930.75
212	22	9	51	32936.75	203	12	5	20	32949	218	22	30	38	32932
213	22	10	20	32936	204	12	6	51	32949	219	22	31	8	32932.25
214	22	10	48	32937	205	12	7	28	32949	220	22	31	43	32932
215	22	11	15	32937	206	12	9	5	32949	BS 9	22	34	18	32943
216	22	11	41	32937	207	12	9	54	32949.25	BS 10	23	10	46	32948
217	22	12	19	32938	208	12	10	47	32949	221	23	12	31	32935
218	22	13	3	32938	209	12	12	1	32949	222	23	13	2	32937
219	22	13	28	32939	210	12	12	45	32949	223	23	13	30	32935.75
220	22	14	10	32938.25	211	12	13	4	32949	224	23	14	14	32935.5
221	22	14	51	32939.5	212	12	13	40	32949	225	23	15	3	32937
222	22	15	10	32939	213	12	14	15	32949	226	23	15	30	32937

223	22	15	36	32939	214	12	14	54	32949.25	227	23	16	21	32936
224	22	16	2	32940.75	215	12	15	51	32949	228	23	17	3	32937
225	22	16	37	32940.75	216	12	16	24	32950	229	23	18	13	32936
226	22	17	20	32940.25	217	12	17	0	32949.25	230	23	18	47	32937
227	22	17	46	32941.75	218	12	17	43	32949.5	231	23	19	42	32937
228	22	18	25	32941.5	219	12	18	30	32950	232	23	20	14	32937
229	22	18	58	32942.25	220	12	19	13	32950	233	23	20	47	32936
230	22	19	30	32943	221	12	19	48	32950	234	23	21	33	32936.75
231	22	20	14	32943	222	12	20	29	32950	235	23	22	39	32937.5
232	22	20	47	32943.75	223	12	21	3	32950	236	23	23	10	32937
233	22	21	15	32944	224	12	21	34	32950	237	23	23	38	32937
234	22	22	0	32944	225	12	22	10	32950	238	23	24	29	32937.75
235	22	22	29	32944	226	12	22	44	32950	239	23	25	45	32936.75
BS 7	22	23	48	32968	227	12	23	34	32950.25	240	23	26	20	32935.75
236	22	24	55	32945	228	12	24	14	32950.5	241	23	26	51	32936.25
237	22	25	43	32945	229	12	25	25	32951	242	23	27	57	32937
238	22	26	20	32946	230	12	26	8	32952	243	23	28	52	32938
239	22	26	56	32946	231	12	27	2	32951	244	23	29	31	32936
240	22	27	27	32947	232	12	28	29	32952	245	23	30	18	32938
241	22	27	53	32946.25	233	12	29	14	32952	246	23	30	59	32937
242	22	28	22	32947	234	12	30	9	32952	247	23	31	27	32937
243	22	28	59	32947	235	12	30	39	32952	248	23	32	6	32938
244	22	30	0	32947	BS 13	12	32	21	32971	249	23	33	9	32937
245	22	30	45	32948.25	236	12	34	40	32952.25	250	23	33	56	32936.5
246	22	31	32	32948	237	12	35	29	32952	251	23	34	42	32937
247	22	31	57	32949	238	12	36	11	32952.25	252	23	35	23	32938
248	22	32	30	32949	239	12	37	29	32952	253	23	35	54	32938.25
249	22	32	57	32950	240	12	38	17	32952	254	23	37	10	32938
250	22	33	26	32949.25	241	12	38	56	32952	255	23	37	51	32937.75
251	22	34	1	32949.25	242	12	39	37	32952	256	23	38	36	32937
252	22	34	43	32950	243	12	40	14	32952	257	23	39	18	32938
253	22	35	9	32950.5	244	12	40	46	32951	258	23	40	8	32937
254	22	35	43	32950	245	12	41	56	32951	259	23	40	34	32937.75
255	22	36	13	32950	246	12	42	26	32951.75	260	23	41	31	32937.75
256	22	36	42	32950	247	12	43	31	32952	261	23	42	12	32937
257	22	37	15	32950	248	12	44	29	32951	262	23	42	47	32937
258	22	37	47	32950	249	12	45	58	32950	263	23	43	27	32938
259	22	39	7	32951	250	12	46	32	32950	264	23	44	6	32938
260	22	39	34	32950.25	251	12	47	1	32950	265	23	44	30	32936

261	22	40	21	32951	252	12	48	7	32950	266	23	45	26	32938
262	22	40	58	32952	253	12	51	23	32949	BS 11	23	46	22	32953
263	22	41	41	32951	254	12	51	56	32949	267	23	47	22	32936
264	22	42	12	32951	255	12	52	19	32949.5	268	23	47	53	32938
265	22	42	52	32951	256	12	52	55	32949	269	23	48	24	32938
266	22	43	24	32952	257	12	53	23	32949.75	270	23	48	54	32938.25
267	22	44	15	32950	258	12	53	53	32949	271	23	49	29	32938
268	22	44	45	32950	259	12	55	6	32952	272	23	50	19	32939
269	22	45	50	32950	260	12	55	37	32947	273	23	50	54	32939
270	22	46	42	32950	261	12	56	47	32950.25	274	23	51	37	32940
271	22	47	9	32949	262	12	57	28	32949.5	275	23	52	17	32940.5
272	22	48	7	32949.75	263	12	58	20	32947.5	276	23	53	5	32940
273	22	48	56	32949	264	1	59	29	32950	277	23	53	56	32940
274	22	49	26	32949	265	1	0	32	32951.75	278	23	54	45	32940
275	22	49	51	32949	266	1	1	56	32952.25	279	23	55	11	32939
276	22	50	16	32948.75	BS 14	1	3	0	32967	280	23	55	48	32940
277	22	51	19	32948	267	1	4	29	32950	281	23	56	15	32939.5
278	22	51	42	32949	268	1	5	23	32950	282	23	57	39	32940
279	22	52	8	32948.75	269	1	5	51	32950	283	23	58	8	32939.25
BS 8	22	53	25	32972	270	1	6	22	32950	284	23	59	5	32939
280	22	54	19	32949	271	1	7	27	32950	285	23	59	41	32940
281	22	55	5	32949.75	272	1	8	2	32950	286	24	0	41	32940
282	22	55	31	32950	273	1	8	50	32949	287	24	1	42	32939.75
283	22	56	29	32950	274	1	9	24	32949.75	288	24	2	18	32939.25
284	22	57	18	32950	275	1	10	2	32950	289	24	2	57	32939.25
285	22	57	52	32950	276	1	10	47	32950	290	24	3	38	32939
286	22	58	46	32949	277	1	11	29	32950	291	24	4	9	32940
287	22	59	7	32950	278	1	11	50	32950.25	292	24	4	59	32940
288	22	59	40	32950	279	1	13	15	32949	293	24	5	28	32939.5
289	23	0	6	32950	280	1	14	19	32950	294	24	6	12	32939.5
290	23	0	42	32950	281	1	14	50	32950	295	24	6	44	32940
291	23	1	16	32950.75	282	1	15	33	32950.25	296	24	7	18	32940.75
292	23	2	4	32948	283	1	16	26	32951	297	24	8	30	32939
293	23	2	32	32949	284	1	17	36	32950	298	24	9	24	32938
294	23	3	21	32949	285	1	18	14	32950.25	299	24	10	7	32938
295	23	3	49	32949	286	1	18	58	32950	300	24	10	34	32937
296	23	4	31	32949	287	1	19	29	32950	BS 12	24	11	35	32950

297	23	5	2	32950	288	1	19	51	32950					
298	23	5	34	32949	289	1	20	35	32950					
299	23	6	9	32950	290	1	21	9	32950.25					
300	23	6	40	32950	291	1	21	38	32950					
BS 9	23	7	45	32971	292	1	21	55	32950					
					293	1	22	15	32950.25					
					294	1	23	2	32951.5					
					295	1	23	42	32952					
					296	1	25	31	32952					
					297	1	26	30	32952					
					298	1	27	8	32952					
					299	1	28	12	32951					
					300	1	29	25	32952					
					BS 15	1	30	35	32969					

Location 2

LINE 1				LINE 2				LINE 3						
SN	Time			TMI (Ave)	SN	Time			TMI (Ave)	SN	Time			TMI (Ave)
	H	M	S			H	M	S			H	M	S	
BS1	1	30	15	32924	BS1	20	43	0	32916	BS1	22	25	42	32925
1	1	31	53	32979	1	20	44	19	32969	1	22	27	38	32981.25
2	1	33	46	32978	2	20	44	46	32968	2	22	28	20	32982
3	1	34	36	32978	3	20	45	34	32967.25	3	22	29	10	32981
4	1	35	4	32976.5	4	20	46	36	32966.75	4	22	29	40	32981
5	1	35	39	32975	5	20	47	9	32967	5	22	30	11	32981
6	1	36	6	32977	6	20	48	2	32967	6	22	30	35	32980.75
7	1	36	34	32975.75	7	20	48	29	32966.75	7	22	31	13	32980
8	1	37	19	32976.25	8	20	48	55	32966	8	22	32	0	32980
9	1	37	47	32976	9	20	49	20	32966	9	22	32	28	32980
10	1	38	11	32976	10	20	49	52	32965.75	10	22	32	50	32979
11	1	38	39	32976	11	20	50	19	32966	11	22	33	27	32979
12	1	39	20	32975.5	12	20	50	42	32965.25	12	22	33	57	32979
13	1	40	13	32975.25	13	20	51	24	32965.25	13	22	35	17	32978.75
14	1	40	44	32974.75	14	20	52	36	32965.25	14	22	36	25	32978.25
15	1	40	59	32975	15	20	53	24	32964.25	15	22	36	56	32978.25
16	1	41	13	32975	16	20	53	56	32965	16	22	37	37	32978
17	1	41	56	32974.75	17	20	54	42	32965	17	22	38	5	32978
18	1	42	46	32973.75	18	20	55	39	32964	18	22	39	7	32977.75
19	1	43	15	32973.75	19	20	56	24	32964	19	22	39	35	32978
20	1	43	44	32973	20	20	56	55	32964.25	20	22	40	20	32978
21	1	44	50	32972.75	21	20	57	44	32963	21	22	40	45	32977
22	1	45	50	32974	22	20	58	14	32963.25	22	22	41	8	32977
23	1	46	17	32974	23	20	58	53	32962.25	23	22	41	53	32977
24	1	46	52	32974	24	20	59	53	32962.5	24	22	42	22	32977
25	1	47	22	32973	25	21	0	23	32962.25	25	22	42	52	32976.25
26	1	47	46	32972.75	26	21	1	3	32962.25	26	22	43	36	32977
27	1	48	33	32973	27	21	1	35	32962.75	27	22	44	27	32976
28	1	49	49	32973	28	21	2	34	32962.75	28	22	45	12	32976
29	1	50	24	32973	29	21	3	14	32963	29	22	45	38	32976
30	1	52	14	32970	30	21	3	48	32963	30	22	46	44	32975
31	1	52	52	32967	31	21	4	30	32962.25	31	22	47	47	32976
32	1	53	23	32966	32	21	5	15	32961.75	32	22	48	15	32975
33	1	57	2	32966	33	21	7	55	32962	33	22	49	6	32975
34	1	57	32	32967	34	21	8	26	32962	34	22	49	40	32974.5

35	1	58	9	32967	35	21	8	51	32963	35	22	50	9	32974.25
36	1	59	37	32966	36	21	9	14	32963.25	36	22	51	8	32975
37	2	0	22	32967.75	37	21	9	46	32964	37	22	51	46	32975
38	2	1	48	32970	38	21	10	12	32964.25	38	22	52	32	32974
39	2	2	24	32969	39	21	10	36	32965	39	22	53	26	32974
40	2	3	8	32968	40	21	11	11	32965	40	22	54	13	32974.25
41	2	3	42	32969	41	21	11	39	32966	41	22	54	42	32974.25
42	2	4	30	32969	42	21	12	15	32966	42	22	55	31	32973.75
43	2	5	4	32970	43	21	12	42	32966	BS2	22	57	3	32926
44	2	5	41	32971.5	44	21	13	20	32965	BS3	23	13	58	32927
45	2	6	13	32970	BS2	21	14	20	32920	43	23	17	25	32976
BS2	2	8	20	32924	45	21	15	25	32966	44	23	18	31	32976
46	2	10	2	32971	46	21	16	5	32966	45	23	18	59	32976
47	2	10	41	32971	47	21	16	39	32967	46	23	20	46	32976
48	2	11	11	32970.25	48	21	17	8	32967	47	23	23	20	32976
49	2	11	50	32970	49	21	17	41	32967.25	48	23	24	27	32976
50	2	12	58	32971.75	50	21	18	23	24808.25	49	23	25	7	32975.5
51	2	14	6	32974	51	21	19	38	32969	50	23	26	18	32974
52	2	14	44	32973	52	21	20	20	32968.25	51	23	27	0	32973.75
53	2	15	24	32977	53	21	20	54	32969	52	23	27	39	32974
54	2	15	49	32977	54	21	21	34	32968.25	53	23	28	13	32973
55	2	16	16	32976.25	55	21	22	21	32968.75	54	23	29	6	32973
56	2	17	8	32978	56	21	22	59	32969	55	23	31	10	32972
57	2	18	14	32980.75	57	21	23	47	32969	56	23	31	39	32972
58	2	19	26	32981	58	21	24	14	32969.25	57	23	33	20	32972
59	2	19	43	32982	59	21	24	40	32968.75	58	23	34	39	32971.75
60	2	20	28	32982.25	60	21	25	10	32968.25	59	23	35	38	32972
61	2	21	1	32988.75	61	21	25	45	32968.25	60	23	36	3	32972
62	2	21	56	32986.25	62	21	26	22	32968	61	23	37	30	32972
63	2	24	11	32976	63	21	28	31	32970	62	23	38	40	32971
64	2	24	40	32974.25	64	21	29	5	32968.75	63	23	39	58	32974.75
65	2	25	28	32972.25	65	21	29	55	32968	64	23	42	20	32970.75
66	2	26	29	32973	66	21	30	24	32968.75	65	23	43	5	32970.5
67	2	27	2	32970	67	21	31	1	32968	66	23	43	44	32970.75
68	2	28	5	32970	68	21	31	38	32968	BS4	23	46	0	32929
69	2	28	49	32970	69	21	32	13	32968	67	23	47	52	32970.25
70	2	30	53	32971.25	70	21	33	6	32968	68	23	48	31	32970.75
71	2	32	31	32970	71	21	33	51	32967.75	69	23	49	14	32971.5
72	2	33	9	32968.75	72	21	34	24	32967	70	23	49	55	32970

73	2	33	52	32968	73	21	34	56	32967	71	23	50	42	32969.75
74	2	34	42	32965	74	21	35	51	32967	72	23	51	27	32970
75	2	35	28	32965.5	75	21	36	29	32967	73	23	52	42	32969.75
76	2	35	52	32964.75	76	21	38	15	32967	74	23	54	24	32970
77	2	36	19	32963	77	21	38	44	32966.75	75	23	55	23	32969.5
78	2	37	5	32962.5	78	21	39	42	32966	76	23	56	51	32969.5
79	2	37	52	32962	79	21	40	18	32966	77	23	57	26	32969.5
80	2	38	13	32961	80	21	41	5	32966.25	78	23	58	12	32969
81	2	39	32	32962	81	21	41	44	32967	79	23	58	34	32969
82	2	41	19	32961	82	21	42	9	32967.75	80	23	59	18	32968.5
83	2	42	17	32960.75	83	21	42	41	32967.25	81	23	59	53	32969
84	2	42	52	32960	84	21	43	18	32967	82	24	0	59	32968
85	2	43	25	32960	85	21	44	3	32967	83	24	2	8	32968
86	2	44	17	32959	BS3	21	45	52	32925	84	24	2	42	32968
87	2	45	29	32958	86	21	47	50	32966	85	24	3	32	32968
88	2	47	57	32953.25	87	21	48	26	32965	86	24	4	8	32968
89	2	49	34	32953.25	88	21	48	56	32965.5	87	24	4	41	32967.75
BS3	2	51	27	32925	89	21	50	9	32966	88	24	6	30	32968
BS4	15	35	22	32918	90	21	50	58	32966	89	24	6	59	32968
90	15	37	26	32942	91	21	52	51	32964	90	24	7	26	32967
91	15	37	52	32942.5	92	21	53	28	32964.25	91	24	8	1	32967
92	15	38	24	32943	93	21	54	2	32964	92	24	8	45	32967.75
93	15	38	59	32944	94	21	54	33	32964	93	24	9	25	32967.25
94	15	39	59	32944	95	21	55	20	32964	94	24	10	1	32968
95	15	40	49	32942.25	96	21	55	49	32964	95	24	10	41	32967
96	15	42	43	32943	97	21	56	24	32964.25	96	24	11	17	32967
97	15	43	8	32943.5	98	21	57	2	32964.5	97	24	12	8	32967
98	15	43	55	32943.75	99	21	57	33	32964.75	98	24	12	37	32967
99	15	45	38	32942	100	21	58	5	32964	99	24	13	2	32967
100	15	48	13	32946.25	101	21	59	18	32965	BS5	24	14	9	32929
101	15	49	42	32945.5	102	22	0	19	32964.75	100	24	15	22	32967
102	15	50	12	32945	103	22	1	0	32964.5	101	24	16	2	32967
103	15	51	7	32944.5	104	22	1	50	32965	102	24	16	33	32967
104	15	52	0	32945.25	105	22	2	12	32965	103	24	16	56	32966
105	15	52	45	32945	106	22	2	55	32965	104	24	17	48	32966
106	15	53	50	32944	107	22	3	44	32964.75	105	24	18	17	32966
107	15	55	13	32944	108	22	5	4	32964	106	24	18	42	32965.75
108	15	56	42	32944	109	22	5	58	32965.75	107	24	19	54	32966
109	15	57	57	32944.25	110	22	6	39	32965.75	108	24	28	30	32967

110	16	1	15	32944	BS4	22	8	1	32923	109	24	30	4	32968
BS5	16	4	52	32916						110	24	31	20	32967
										BS6	24	32	40	32922

LINE 4				LINE 5				LINE 6						
SN	Time			TMI (Ave)	SN	Time			TMI (Ave)	SN	Time			TMI (Ave)
	H	M	S			H	M	S			H	M	S	
BS1	2	24	15	32920	BS1	24	17	6	32945.75	BS1	2	25	19	32937
1	2	25	37	32982.25	1	24	18	25	32995	1	2	26	19	32982
2	2	27	54	32981.25	2	24	19	16	32995	2	2	27	21	32981.75
3	2	28	17	32981.25	3	24	19	46	32995	3	2	27	59	32980.5
4	2	28	40	32981.5	4	24	20	12	32995	4	2	28	46	32982
5	2	29	3	32981	5	24	20	22	32994	5	2	29	9	32981.5
6	2	29	36	32981	6	24	20	54	32994	6	2	30	8	32981
7	2	30	13	32981	7	24	21	28	32993.25	7	2	30	33	32981
8	2	30	50	32981	8	24	22	21	32993	8	2	31	7	32980.75
9	2	31	15	32981	9	24	22	43	32992.25	9	2	31	53	32980.75
10	2	32	28	32980.25	10	24	23	22	32991.5	10	2	32	21	32980
11	2	33	6	32981	11	24	24	11	32991.5	11	2	33	9	32980
12	2	33	39	32980	12	24	24	38	32991.25	12	2	33	33	32980
13	2	34	3	32980	13	24	25	10	32991.25	13	2	34	30	32980
14	2	34	37	32980	14	24	25	44	32991	14	2	35	2	32979
15	2	35	37	32979.75	15	24	26	9	32991	15	2	35	27	32980
16	2	36	17	32979.75	16	24	26	53	32990.25	16	2	39	6	32979
17	2	36	54	32979.75	17	24	27	34	32990.25	17	2	39	45	32980
18	2	37	20	32979.25	18	24	28	16	32990.25	18	2	40	17	32979
19	2	37	50	32979	19	24	28	35	32990.5	19	2	40	48	32979
20	2	38	28	32978.75	20	24	29	25	32990.25	20	2	41	15	32979
21	2	39	40	32980	21	24	30	8	32990	21	2	42	7	32978.75
22	2	40	11	32979	22	24	30	30	32989	22	2	42	49	32978
23	2	40	36	32978.75	23	24	30	54	32989	23	2	43	8	32977
24	2	41	11	32979	24	24	31	34	32989	24	2	43	32	32977
25	2	41	58	32980	25	24	32	2	32989	25	2	44	7	32976.5
26	2	42	25	32979	26	24	32	31	32988	26	2	44	33	32977.25
27	2	42	51	32979	27	24	33	1	32988	27	2	44	59	32977
28	2	43	46	32978.25	28	24	33	53	32987	28	2	45	35	32977
29	2	44	11	32978.75	29	24	34	42	32987	29	2	46	3	32977

30	2	44	38	32978	30	24	35	30	32985	30	2	46	47	32976
31	2	45	28	32978	31	24	36	10	32985	31	2	47	21	32975.25
32	2	46	21	32978	32	24	36	35	32986	32	2	47	53	32976
33	2	47	5	32978.25	33	24	36	57	32985	33	2	48	46	32975.5
34	2	50	29	32978	34	24	37	21	32986	34	2	49	12	32975
35	2	51	4	32978	35	24	37	49	32985	35	2	50	37	32975
36	2	51	32	32978	36	24	38	22	32985	36	2	51	9	32974
37	2	52	0	32977	37	24	38	47	32985	37	2	51	17	32974.5
38	2	52	28	32977	38	24	39	11	32985	38	2	52	48	32974.75
39	2	53	19	32977	39	24	39	48	32984	39	2	53	20	32974.5
40	2	53	39	32977	40	24	40	19	32985	40	2	53	39	32974.25
41	2	54	4	32976	41	24	40	57	32984.25	41	2	54	8	32975
42	2	54	32	32976.25	42	24	41	22	32983.25	42	2	54	52	32974.25
43	2	55	4	32976	43	24	42	25	32984	43	2	55	19	32974
44	2	55	33	32976	44	24	44	30	32983	BS2	2	57	20	32934
45	2	56	70	32975	45	24	46	18	32983	44	3	1	10	32972
46	2	56	37	32975.25	46	24	47	33	32982	45	3	1	50	32971
47	2	57	4	32975	47	24	48	8	32981.75	46	3	2	22	32971
48	2	57	33	32974.25	48	24	48	48	32982	47	3	2	50	32971
49	2	58	7	32973.5	49	24	49	26	32982	48	3	3	14	32971
50	2	58	46	32974	50	24	49	58	32981.75	49	3	4	11	32970
51	2	59	19	32973	51	24	50	12	32982	50	3	4	40	32970.75
52	2	59	41	32973	52	24	51	26	32982	51	3	5	27	32970
53	3	0	14	32972.75	BS2	24	52	47	32942.75	52	3	6	7	32970
BS 2	3	1	36	32921	53	24	54	18	32979	53	3	7	7	32970
54	3	3	10	32972	54	24	54	49	32979.25	54	3	7	37	32970
55	3	3	27	32972	55	24	55	24	32978.75	55	3	8	32	32969.75
56	3	3	44	32970.75	56	24	55	56	32978	56	3	9	31	32970
57	3	4	32	32970	57	24	56	20	32978.25	57	3	9	54	32970
58	3	4	59	32970.5	58	24	57	2	32977.5	58	3	10	28	32969
59	3	5	48	32969	59	24	57	48	32978	59	3	11	5	32969
60	3	6	17	32969	60	24	58	24	32977.25	60	3	11	38	32969
61	3	7	31	32967.75	61	24	59	6	32977.25	61	3	12	21	32969
62	3	8	11	32965.75	62	24	59	48	32977	62	3	12	46	32969
63	3	8	54	32966.25	63	1	0	19	32977.75	63	3	13	25	32968
64	3	9	45	32965.5	64	1	0	58	32977	64	3	13	52	32969
65	3	10	32	32964.75	65	1	1	25	32977.75	65	3	14	17	32968.75
66	3	11	48	32963.75	66	1	2	12	32977	66	3	14	51	32968
67	3	12	16	32964	67	1	3	50	32976	67	3	15	29	32967.75

68	3	12	38	32963	68	1	4	40	32976.75	68	3	15	54	32968
69	3	13	2	32962	69	1	5	37	32976.25	69	3	16	21	32968
70	3	13	59	32962	70	1	7	16	32977	70	3	17	47	32968
71	3	14	51	32962	71	1	8	3	32975	71	3	18	14	32968
72	3	15	40	32962	72	1	8	51	32975.75	72	3	18	41	32968
73	3	16	27	32963	73	1	9	53	32976	73	3	19	45	32968
74	3	17	6	32961	74	1	10	36	32975.5	BS3	3	22	23	32927.25
75	3	17	40	32960.25	75	1	12	4	32974.75	74	3	24	1	32966.75
76	3	19	34	32961	76	1	12	48	32974.75	75	3	24	46	32966
77	3	20	1	32962	77	1	13	49	32975	76	3	25	37	32966
78	3	20	23	32962	78	1	14	22	32974.5	77	3	26	29	32965.75
79	3	21	24	32962	79	1	15	24	32974	78	3	27	8	32966
80	3	22	23	32962	80	1	16	41	32974	79	3	27	52	32966
81	3	22	52	32961.5	81	1	17	14	32974	80	3	28	40	32973
82	3	23	16	32962.25	82	1	17	56	32974	81	3	29	14	32965
83	3	24	30	32963	83	1	18	18	32974	82	3	29	45	32965
84	3	25	4	32964	84	1	19	8	32974	83	3	30	21	32965
85	3	25	54	32962.75	85	1	19	51	32974	84	3	30	53	32964
86	3	26	37	32963	86	1	20	15	32974	85	3	31	39	32965.75
87	3	26	49	32963	87	1	20	45	32973	86	3	32	27	32965.25
88	3	27	15	32964	88	1	22	41	32973	87	3	32	58	32969
89	3	27	43	32963	BS3	1	24	25	32938.5	88	3	33	49	32968
90	3	28	21	32963.75	89	1	25	51	32972	89	3	34	46	32966
91	3	28	50	32963	90	1	26	17	32973	90	3	35	34	32965.25
92	3	29	16	32963.25	91	1	27	10	32974	91	3	36	5	32966.5
93	3	29	55	32962.5	92	1	27	42	32972	92	3	36	52	32966
94	3	30	42	32963	93	1	28	23	32970.75	93	3	37	23	32966
95	3	31	26	32962.75	94	1	28	53	32971	94	3	38	3	32966
96	3	32	5	32962	95	1	29	19	32971	95	3	38	59	32966
97	3	32	50	32962	96	1	29	51	32971	96	3	39	30	32966
98	3	33	44	32962	97	1	30	15	32970.75	97	3	39	57	32966
99	3	34	50	32961	98	1	30	51	32970	98	3	43	10	32966.25
100	3	35	20	32960.75	99	1	31	22	32970	99	3	45	29	32966.75
BS3	3	36	43	32917.75	100	1	31	50	32970	100	3	46	12	32967.5
101	3	37	36	32959	101	1	32	17	32970	101	3	47	5	32968
102	3	38	22	32960	102	1	32	55	32970	102	3	47	45	32967
103	3	39	31	32957.75	103	1	34	4	32969.25	103	3	48	24	32966.75
104	3	40	25	32959.5	104	1	34	44	32970	104	3	49	0	32970
105	3	40	56	32959	105	1	35	34	32969	105	3	49	42	32966.25

Location 3

LINE 1				LINE 2				LINE 3						
SN	Time			TMI (Ave)	SN	Time			TMI (Ave)	SN	Time			TMI (Ave)
	H	M	S			H	M	S			H	M	S	
BS1	24	37	26	33035.25	BS1	23	54	11	33032	BS1	1	43	37	33018
1	24	39	40	33046	1	23	57	30	33262.75	1	1	44	59	33040
2	24	41	27	33047.75	2	23	58	35	33254	2	1	45	58	33040.5
3	24	44	26	33046.75	3	24	1	13	33256	3	1	46	29	33039.5
4	24	45	33	33047	4	24	2	57	33249	4	1	46	58	33040
5	24	46	24	33047	5	24	3	28	33241	5	1	47	39	33039.5
6	24	47	3	33047	6	24	4	1	33240.75	6	1	48	14	33038.25
7	24	47	50	33047	7	24	4	26	33238	7	1	48	48	33038.75
8	24	48	26	33046.75	8	24	5	53	33240	8	1	49	14	33038
9	24	49	11	33046	9	24	6	17	33233.75	9	1	49	38	33038
10	24	50	22	33046.5	10	24	6	55	33232	10	1	50	15	33038
11	24	51	11	33046.25	11	24	7	54	33225.5	11	1	51	3	33037.75
12	24	51	52	33046.5	12	24	8	22	33223.25	12	1	51	33	33037
13	24	53	9	33046.25	13	24	9	6	33222	13	1	52	14	33036.25
14	24	54	34	33046.5	14	24	10	54	33216	14	1	52	59	33036.75
15	24	55	30	33046.25	15	24	11	22	33216.5	15	1	53	13	33036.5
16	24	56	43	33046.5	16	24	12	14	33208	16	1	54	46	33036.75
17	24	58	7	33046.5	17	24	12	35	33205.5	17	1	55	54	33035
18	24	59	16	33046.25	18	24	13	36	33204.5	18	1	56	4	33034.75
19	1	0	5	33046	19	24	14	11	33204	19	1	56	49	33034
20	1	1	0	33046	20	24	14	39	33204.25	20	1	57	8	33034
21	1	1	46	33046	21	24	15	26	33201.25	21	1	57	32	33034
22	1	2	20	33046.5	22	24	15	56	33200	22	1	58	19	33033
23	1	3	23	33046	23	24	16	52	33196	23	1	58	46	33032.75
24	1	3	57	33046.25	24	24	17	35	33192	24	1	59	14	33032
25	1	4	53	33046.5	25	24	18	42	33191	25	1	59	39	33032
26	1	7	25	33046	26	24	19	20	33188.25	26	2	0	19	33032
BS2	1	9	3	33035	27	24	20	21	33184.75	27	2	0	52	33031
27	1	11	5	33046	28	24	21	22	33185	28	2	1	42	33031
28	1	11	55	33046	29	24	22	11	33178.75	29	2	2	8	33031
29	1	12	33	33046	30	24	23	6	33177	30	2	2	45	33030
30	1	13	1	33046	31	24	23	41	33176	31	2	3	26	33030
31	1	15	50	33046	32	24	24	12	33174	32	2	3	52	33030
32	1	16	51	33046	33	24	24	57	33170	33	2	4	23	33030
33	1	17	38	33046	BS2	24	26	30	33030	34	2	5	11	33030

34	1	18	19	33046	34	24	30	36	33166.5	35	2	5	37	33029
35	1	18	58	33046	35	24	32	20	33165.75	36	2	6	30	33028.25
36	1	19	53	33045.25	36	24	32	52	33163.75	37	2	7	6	33029
37	1	20	40	33046	37	24	33	14	33164.25	38	2	7	40	33029
38	1	21	24	33046	38	24	33	40	33160.75	39	2	8	49	33028
39	1	25	23	33046.5	39	24	34	34	33158.5	40	2	9	26	33028
40	1	27	6	33046.75	40	24	35	52	33156.25	41	2	10	10	33028
41	1	28	1	33046.5	41	24	36	32	33156	42	2	10	40	33027
42	1	28	44	33047.25	42	24	37	1	33155.25	43	2	11	24	33027
43	1	29	52	33047.25	43	24	37	51	33155.25	44	2	12	8	33026.25
44	1	30	32	33048	44	24	38	27	33151.25	45	2	12	40	33026
45	1	31	39	33047.25	45	24	39	0	33150	46	2	13	15	33026
46	1	32	36	33047.5	46	24	39	40	33149	47	2	13	44	33026.75
47	1	33	22	33048.5	47	24	40	10	33147.25	48	2	14	5	33026
BS3	1	36	32	33029	48	24	41	4	33144.75	49	2	14	56	33026
48	1	39	0	33048	49	24	41	30	33144	50	2	15	26	33025.5
49	1	39	43	33048	50	24	41	51	33143.5	BS	2	17	7	33013
50	1	40	16	33048	51	24	42	34	33142.5	51	2	20	13	33025.75
51	1	40	45	33048	52	24	43	20	33139.75	52	2	21	14	33025.5
52	1	41	11	33048	53	24	43	53	33137.5	53	2	21	52	33025
53	1	41	40	33048	54	24	44	23	33135.25	54	2	22	25	33025
54	1	42	5	33048	55	24	44	54	33135	55	2	23	8	33024
55	1	42	52	33049	56	24	45	21	33134.25	56	2	23	35	33024
56	1	43	42	33049	57	24	46	5	33134	57	2	24	22	33024
57	1	44	44	33049.25	58	24	46	45	33132	58	2	25	2	33024
58	1	45	12	33049	59	24	47	24	33130.25	59	2	25	31	33023.75
59	1	45	39	33049	60	24	48	25	33128	60	2	26	42	33023
60	1	46	8	33049	61	24	49	10	33127.25	61	2	27	26	33023
61	1	46	36	33048.5	62	24	49	44	33124	62	2	28	15	33023
62	1	47	29	33049.25	63	24	50	22	33122	63	2	28	48	33023
63	1	47	59	33050	64	24	51	45	33122.25	64	2	29	15	33022
64	1	48	23	33049	65	24	52	29	33122.75	65	2	30	8	33022.75
65	1	48	46	33049	66	24	53	3	33122	66	2	30	35	33022
66	1	49	16	33049	67	24	54	0	33121	67	2	31	8	33022
67	1	50	7	33049	68	24	54	29	33121	68	2	31	43	33022
68	1	50	28	33048.75	69	24	55	1	33119.75	69	2	32	44	33021.75
69	1	50	54	33048.5	70	24	55	52	33116	70	2	33	4	33021
70	1	51	15	33048	71	24	56	45	33116	71	2	33	29	33021.25
71	1	52	15	33048	BS3	24	58	17	33026	72	2	34	20	33021

72	1	52	49	33047.25	72	1	7	44	33115	73	2	35	1	33021
73	1	53	38	33047	73	1	8	39	33114.5	74	2	35	29	33021
74	1	53	59	33046	74	1	9	37	33113	75	2	36	21	33021
75	1	54	21	33045.5	75	1	10	18	33112.25	76	2	37	3	33020.25
76	1	54	53	33046.75	76	1	11	17	33112	77	2	37	34	33021
77	1	55	29	33045	77	1	11	53	33110.25	78	2	38	9	33021
78	1	56	14	33045	78	1	12	51	33109.75	79	2	38	36	33020.5
79	1	57	2	33042.75	79	1	13	43	33109	80	2	39	41	33020
80	1	57	42	33042	80	1	14	30	33107.75	81	2	39	39	33020
81	1	58	5	33039.25	81	1	15	11	33107	82	2	40	58	33020
82	1	59	36	33041	82	1	17	1	33105	83	2	41	37	33019.75
83	2	0	2	33039	83	1	18	46	33098	84	2	42	55	33019.25
84	2	0	49	33038	84	1	20	44	33104.75	85	2	43	51	33018.25
85	2	1	15	33036.25	85	1	21	24	33104	86	2	44	47	33018.25
86	2	1	44	33037.25	86	1	22	1	33103	87	2	45	15	33017.25
87	2	2	3	33036.75	87	1	23	2	33102	BS	2	46	52	33012
88	2	3	42	33036	88	1	23	34	33101.75	88	2	48	50	33016
89	2	4	11	33034.25	89	1	24	2	33100	89	2	49	29	33016.25
90	2	4	43	33033.75	90	1	25	35	33098.25	90	2	50	20	33016
91	2	5	18	33033	91	1	25	33	33098	91	2	50	46	33016
92	2	5	49	33034	92	1	27	45	33097	92	2	51	26	33016
93	2	6	13	33032	93	1	28	22	33096	93	2	52	12	33016
BS4	2	8	50	33024	94	1	29	21	33096	94	2	52	45	33015
94	2	11	17	33031.5	95	1	30	28	33095	95	2	53	11	33015
95	2	11	50	33031	BS4	1	31	43	33024	96	2	53	47	33015
96	2	12	14	33031	96	1	34	11	33094	97	2	56	54	33016
97	2	13	4	33029.75	97	1	34	46	33093	98	2	58	3	33015.75
98	2	13	43	33032.5	98	1	35	59	33092	99	2	58	30	33016
99	2	14	40	33033.75	99	1	36	37	33092	100	2	59	2	33016
100	2	15	4	33034	100	1	37	17	33091	101	3	0	7	33015.25
101	2	15	38	33034.75	101	1	38	7	33090	102	3	0	46	33015.75
102	2	16	8	33036	102	1	39	22	33090	103	3	1	19	33015.5
103	2	16	34	33036	103	1	40	13	33089	104	3	1	49	33016
104	2	17	15	33036	BS5	1	49	11	33023	105	3	2	18	33015.25
105	2	18	4	33037	BS6	3	29	14	33032	106	3	2	45	33016
106	2	18	46	33037	103	3	32	6	33084.75	107	3	3	12	33016
107	2	19	11	33037.5	104	3	32	33	33084.25	108	3	3	53	33016
108	2	19	56	33038	105	3	32	54	33084	109	3	4	23	33016
109	2	21	3	33038	106	3	33	31	33083	110	3	4	43	33015.75

110	2	21	44	33039	107	3	34	1	33084	111	3	5	24	33016
111	2	22	14	33038.75	108	3	34	22	33081.75	112	3	5	49	33015.75
112	2	22	51	33038	109	3	35	6	33081	113	3	6	29	33015
113	2	23	31	33037.25	110	3	35	23	33081	114	3	7	9	33014.25
114	2	24	1	33037.25	111	3	35	34	33080	115	3	7	50	33014.25
115	2	24	47	33036	112	3	36	23	33079	116	3	8	19	33014.75
116	2	25	16	33036	113	3	37	10	33079	117	3	9	8	33015
117	2	25	50	33035	114	3	38	4	33078	118	3	9	40	33014.25
118	2	26	11	33035.75	115	3	38	33	33076.75	119	3	9	54	33014
119	2	26	49	33033	116	3	39	10	33076	120	3	10	28	33014.25
120	2	27	34	33032	117	3	39	32	33076	121	3	11	14	33014
121	2	28	15	33032	118	3	40	23	33075.5	122	3	11	39	33013.75
122	2	29	14	33031	119	3	41	1	33073.75	123	3	12	26	33013.5
123	2	30	30	33031	120	3	41	55	33073.25	124	3	12	57	33013.25
124	2	31	10	33030.75	121	3	42	45	33072.25	125	3	13	38	33013.25
125	2	31	46	33030	122	3	43	15	33072.25	126	3	14	12	33013
126	2	32	5	33029	123	3	43	45	33070.75	127	3	14	31	33013
127	2	32	29	33029.5	124	3	44	12	33070.5	128	3	14	53	33012
128	2	33	25	33029	125	3	44	44	33070	129	3	15	38	33013.75
129	2	34	11	33029	126	3	45	10	33069	130	3	16	12	33012.25
130	2	34	40	33029	127	3	45	33	33069	BS	3	17	25	33013
131	2	35	13	33028	128	3	46	10	33069	131	3	19	2	33013.25
132	2	35	46	33028	129	3	46	38	33067	132	3	19	53	33013.25
133	2	36	25	33027	130	3	47	4	33066	133	3	20	26	33012
134	2	37	27	33027.75	131	3	47	33	33064	134	3	21	5	33012
135	2	37	51	33027	132	3	48	13	33064.75	135	3	21	25	33012
136	2	38	37	33027	133	3	48	57	33064	136	3	21	59	33012.25
137	2	39	59	33025	134	3	49	22	33064.25	137	3	22	55	33012
138	2	41	37	33026.5	135	3	49	47	33063	138	3	23	30	33011.5
139	2	43	20	33024.75	136	3	50	24	33062.5	139	3	24	27	33011
140	2	44	7	33025	137	3	50	54	33061	140	3	24	57	33011
141	2	44	53	33025	138	3	51	35	33060	141	3	25	23	33010
142	2	45	21	33025	139	3	51	49	33059	142	3	25	49	33010
143	2	45	24	33023.75	140	3	52	14	33058.75	143	3	26	5	33010
144	2	46	14	33022.75	141	3	52	40	33059.75	144	3	26	25	33010
145	2	46	51	33021.5	142	3	53	22	33060	145	3	26	57	33010
146	2	47	22	33020	143	3	53	58	33058	146	3	27	17	33010
147	2	47	51	33018.25	144	3	54	20	33057	147	3	27	33	33010
148	2	49	11	33019	145	3	54	47	33056.75	148	3	28	16	33010

149	2	50	0	33014	146	3	55	18	33056.75	149	3	28	47	33009.25
150	2	50	25	33011.75	147	3	55	46	33057	150	3	29	44	33010
151	2	51	14	33009	148	3	57	10	33056.25	151	3	30	13	33010
152	2	51	56	33007	149	3	57	33	33055	152	3	30	33	33010
153	2	52	52	33006	150	3	57	56	33054	153	3	31	10	33010
154	2	53	19	33002	151	3	58	40	33055	154	3	31	42	33010
155	2	54	14	33003	152	3	59	0	33054	155	3	32	20	33010
BS5	2	54	51	33000	153	3	59	39	33053.25	156	3	32	51	33009.25
156	2	55	30	32996.75	BS7	4	0	42	33017	157	3	33	18	33009
157	2	56	10	32995	154	4	2	33	33054	158	3	33	43	33009
158	2	56	43	32989.75	155	4	3	16	33053	159	3	34	13	33009
159	2	57	34	32989.75	156	4	3	40	33053	160	3	35	1	33009
160	2	59	20	32983.25	157	4	4	18	33053.25	161	3	35	33	33009
161	3	0	16	32982.25	158	4	4	52	33051.75	162	3	35	46	33008.5
162	3	1	58	32981	159	4	5	14	33052	163	3	36	35	33009
163	3	4	24	32976.75	160	4	5	50	33052.5	164	3	37	1	33009
164	3	5	15	32977.75	161	4	6	35	33052.75	165	3	37	47	33008.5
165	3	5	43	32976.75	162	4	7	20	33052.5	166	3	38	18	33008.75
166	3	6	58	32976.75	163	4	7	58	33053	167	3	39	3	33008
167	3	7	44	32976.25	164	4	8	20	33052	168	3	39	25	33008
168	3	8	11	32977	165	4	9	5	33052	169	3	40	36	33008
BS6	3	10	47	33023	166	4	9	49	33052.75	170	3	41	37	33007
169	3	12	51	32978.75	167	4	10	13	33052	171	3	42	13	33007.25
170	3	13	22	32980	168	4	11	20	33051	172	3	42	38	33007
171	3	14	25	32979.5	169	4	12	1	33050.5	173	3	43	50	33006
172	3	15	32	32977.5	170	4	12	36	33050.5	174	3	44	55	33006
173	3	16	46	32979	171	4	13	31	33049.5	175	3	45	16	33006
174	3	17	20	32980.25	172	4	14	17	33048.5	176	3	45	54	33006
175	3	17	59	32983	173	4	14	59	33049.25	177	3	46	19	33006
176	3	19	6	32980.75	174	4	15	42	33048	178	3	47	18	33006
177	3	19	37	32987	175	4	16	41	33048	179	3	47	38	33005
178	3	20	14	32990	176	4	17	28	33047.25	BS	3	48	52	33012
179	3	20	53	32991	177	4	17	48	33046.25	180	3	50	1	33004
180	3	21	25	32993	178	4	18	53	33047	181	3	50	42	33005
181	3	21	52	32995	179	4	19	25	33047.75	182	3	51	14	33005.25
182	3	22	59	32995.75	180	4	19	58	33044.75	183	3	52	8	33004.75
183	3	23	36	32999	181	4	20	23	33044.5	184	3	52	44	33004
184	3	24	17	33001	182	4	20	58	33044	185	3	53	16	33004
185	3	25	48	33002.25	183	4	21	26	33045	186	3	53	43	33004

186	3	26	41	33003	184	4	22	17	33043.75	187	3	54	12	33004
187	3	27	11	33007	185	4	22	48	33043.75	188	3	54	38	33003
188	3	27	42	33008.25	186	4	23	38	33043	189	3	55	3	33002.75
189	3	28	22	33010	187	4	24	24	33042.25	190	3	55	28	33003
190	3	29	34	33012	188	4	24	35	33043	191	3	56	1	33003
191	3	31	25	33013.25	189	4	25	49	33041.75	192	3	56	23	33003
192	3	32	28	33014	190	4	26	15	33041.5	193	3	57	10	33003
193	3	33	4	33016.25	191	4	26	57	33041.25	194	3	57	34	33002.75
194	3	33	37	33016.75	192	4	27	28	33041.5	195	3	58	23	33002
195	3	34	32	33018	193	4	28	6	33041	196	3	58	52	33001.25
196	3	34	56	33018	194	4	28	41	33040.25	197	3	59	54	33002
197	3	35	22	33019	195	4	29	19	33040.25	198	4	0	25	33001
198	3	35	47	33019.75	196	4	29	55	33040	199	4	1	1	33000
199	3	36	25	33021	197	4	30	20	33039.25	200	4	1	38	33000
200	3	36	56	33021	198	4	31	37	33039.25	201	4	2	15	33000
201	3	37	33	33022	199	4	31	58	33038.75	202	4	2	42	33000
202	3	37	54	33023	200	4	32	22	33038	203	4	3	17	33000
203	3	38	56	33023.5	BS8	4	34	23	33016	204	4	3	41	32999
204	3	39	24	33023	201	4	36	11	33038	205	4	4	20	32999
205	3	39	49	33023.75	202	4	36	35	33037.25	206	4	4	57	33000
206	3	40	21	33023.25	203	4	37	3	33038.75	207	4	5	48	32998
BS7	3	42	2	33023	204	4	37	53	33039.75	208	4	6	23	32998
BS8	19	36	9	33009.75	205	4	38	44	33038.25	209	4	6	58	32998
206	19	39	31	33010	206	4	39	22	33037.5	210	4	7	21	32998
207	19	40	0	33009	207	4	40	3	33037.25	211	4	8	33	32997
208	19	41	8	33009.75	208	4	40	47	33036.5	212	4	9	5	32997.25
209	19	41	46	33009	209	4	41	44	33037.5	213	4	9	28	32997.75
210	19	42	17	33010	210	4	42	44	33038.25	214	4	9	54	32996
211	19	43	2	33010	211	4	43	19	33037.5	215	4	10	28	32996
212	19	43	41	33010.25	212	4	44	23	33037.25	216	4	11	3	32996
213	19	44	22	33009.5	213	4	44	48	33037	217	4	11	46	32996
214	19	46	4	33009	214	4	45	12	33035.5	218	4	12	18	32995
215	19	46	27	33010	215	4	45	59	33036	219	4	12	46	32995
216	19	46	56	33009	216	4	47	32	33036.5	220	4	13	35	32994.75
217	19	47	37	33009	217	4	48	9	33036	221	4	13	54	32994.75
218	19	48	3	33009	218	4	49	3	33036	222	4	14	44	32994.25
219	19	48	26	33009	219	4	49	53	33036.25	223	4	15	22	32994
220	19	48	56	33009	220	4	50	30	33037	224	4	15	48	32994
221	19	49	17	33009	221	4	51	25	33034.5	225	4	16	13	32994

222	19	49	58	33009	222	4	51	54	33033.5	226	4	16	38	32994
223	19	50	29	33008	223	4	53	2	33032.75	227	4	17	2	32993.5
224	19	52	14	33009	224	4	53	38	33032.75	228	4	17	37	32993
225	19	52	39	33008	225	4	54	5	33032	229	4	18	6	32992.75
226	19	53	11	33008	226	4	54	42	33032	230	4	18	53	32993
227	19	53	33	33007.5	227	4	55	6	33032.5	BS	4	19	50	33007.25
228	19	54	0	33006.25	228	4	56	4	33032.75	231	4	23	53	32991.75
229	19	54	38	33007	229	4	56	50	33032.5	232	4	25	5	32992
230	19	55	11	33006	230	4	57	12	33032	233	4	25	49	32992
231	19	55	40	33005	231	4	57	48	33032	234	4	26	41	32991.5
232	19	56	33	33006	232	4	58	27	33032	235	4	28	38	32991
233	19	57	6	33005	233	4	58	52	33032	236	4	30	26	32992
234	19	57	43	33005	234	4	59	16	33031	237	4	31	18	32991
235	19	58	12	33005	235	4	59	53	33031	238	4	32	27	32991
236	19	58	13 8	33005	236	5	0	10	33031	239	4	33	9	32990.25
237	19	59	16	33005	237	5	0	40	33030.5	240	4	34	20	32991
238	19	59	49	33005	238	5	1	4	33031	241	4	35	14	32990
239	20	0	32	33005	239	5	1	36	33032	242	4	35	38	32990
240	20	1	21	33004	240	5	2	18	33031.25	243	4	36	14	32989.75
241	20	2	6	33004	241	5	2	58	33031	244	4	36	56	32989.5
242	20	2	40	33003	242	5	3	41	33031	245	4	37	39	32990
243	20	3	7	33004	243	5	4	21	33030.75	246	4	38	15	32990
244	20	3	33	33004	244	5	4	48	33030.5	247	4	38	58	32989.75
245	20	4	33	33004.25	245	5	5	41	33030.25	248	4	39	48	32989.5
246	20	5	0	33004	246	5	6	21	33030	249	4	40	36	32989
247	20	5	37	33004	247	5	6	48	33030.25	250	4	41	38	32989.25
248	20	6	5	33004	248	5	7	17	33031.5	251	4	42	24	32989
249	20	7	3	33005	249	5	7	48	33030.25	252	4	44	21	32988
BS9	20	10	20	33015	250	5	8	13	33030	253	4	45	7	32988.75
250	20	12	9	33004.75	BS9	5	9	41	33015	254	4	45	54	32988.5
251	20	12	43	33004.75	BS10	21	2	28	33033	255	4	46	42	32988
252	20	14	10	33004.75	250	21	3	42	33047	256	4	47	52	32988
253	20	14	36	33005	251	21	4	24	33046.25	257	4	48	5	32988
254	20	15	17	33004	252	21	5	19	33046	258	4	48	46	32988
255	20	15	44	33005	253	21	5	41	33046.75	259	4	49	38	32988.75
256	20	16	25	33004.5	254	21	6	7	33046	260	4	50	18	32988.5
257	20	17	6	33004	255	21	6	38	33046.75	BS	4	51	53	33005
258	20	17	49	33005	256	21	7	32	33046.25	BS	20	47	28	33020

259	20	18	37	33005	257	21	8	0	33046.5	260	20	48	46	33001.25
260	20	19	23	33005	258	21	9	2	33046	261	20	49	46	33002
261	20	19	58	33005	259	21	9	23	33046.75	262	20	50	7	33002
262	20	20	53	33005	260	21	9	59	33047	263	20	50	26	33002
263	20	21	26	33005	261	21	10	26	33047	264	20	51	12	33002.75
264	20	21	51	33004	262	21	11	9	33047	265	20	51	39	33002.75
265	20	22	43	33004	263	21	11	33	33047	266	20	52	15	33002
266	20	23	6	33004	264	21	11	52	33047.25	267	20	52	38	33002.25
267	20	23	29	33004	265	21	12	24	33046.75	268	20	53	12	33002
268	20	23	58	33004	266	21	12	55	33047	269	20	53	35	33002.75
269	20	24	23	33004	267	21	13	15	33047	270	20	53	58	33003
270	20	25	2	33004	268	21	13	56	33046.25	271	20	54	45	33003
271	20	25	21	33004	269	21	14	30	33046	272	20	55	10	33002.25
272	20	26	46	33004	270	21	14	57	33046	273	20	55	32	33003
273	20	27	52	33003.25	271	21	15	21	33046.25	274	20	55	55	33002.25
274	20	29	9	33003	272	21	16	10	33046	275	20	56	25	33002
275	20	29	41	33003	273	21	16	33	33047.25	276	20	56	46	33002.25
276	20	30	1	33002.75	274	21	17	0	33046	277	20	57	24	33003
277	20	31	7	33002.5	275	21	17	24	33046.25	278	20	58	9	33002.25
278	20	31	56	33002.75	276	21	17	57	33046	279	20	58	44	33002
279	20	32	56	33003	277	21	18	24	33046	280	20	59	19	33002.5
280	20	33	21	33003	278	21	18	50	33046	281	20	59	48	33001.75
281	20	34	26	33003	279	21	19	31	33046	282	21	0	23	33002
282	20	35	37	33004	280	21	19	54	33046	283	21	1	1	33001.75
283	20	36	10	33004	281	21	20	19	33045	284	21	1	44	33001.25
284	20	37	28	33006	282	21	20	54	33045	285	21	2	33	33000
285	20	38	0	33006	283	21	21	28	33045.25	286	21	3	6	33000
286	20	38	35	33007	284	21	22	3	33045	287	21	3	30	32999.75
287	20	39	25	33007	285	21	22	31	33045.75	288	21	4	27	32999
288	20	40	30	33006	286	21	23	23	33045	289	21	5	12	32999
BS10	20	42	53	33022	287	21	24	6	33045	290	21	6	21	32998
289	20	44	47	33005	288	21	24	42	33044	291	21	6	57	32999
290	20	47	2	33005	289	21	26	19	33046	292	21	7	44	32999
291	20	47	43	33005	290	21	26	59	33045	293	21	8	19	32998.25
292	20	48	12	33005	291	21	27	40	33045	294	21	8	36	32999
293	20	48	35	33005	292	21	28	12	33044.75	295	21	8	55	32998.25
294	20	49	28	33005	293	21	28	43	33044	296	21	9	22	32998
295	20	49	58	33004.5	294	21	29	5	33043	297	21	9	52	32998.75
296	20	50	48	33004.25	295	21	29	51	33043.5	298	21	10	56	32999

297	20	51	20	33005	296	21	30	48	33042.5	299	21	12	21	33000
298	20	51	49	33004	297	21	31	29	33043	300	21	12	57	33000
299	20	52	21	33004.75	298	21	32	5	33041	301	21	13	23	33000.5
300	20	53	1	33005	299	21	32	35	33039.5	302	21	14	20	33001
301	20	53	53	33005	300	21	32	48	33040.25	303	21	14	45	33000.25
302	20	54	28	33005	BS11	21	35	35	33035	304	21	15	3	33000.75
303	20	54	53	33005	301	21	36	48	33040.25	305	21	15	26	33000.75
304	20	55	31	33004	302	21	37	15	33039.25	306	21	16	0	33001
305	20	56	9	33004	303	21	37	32	33039.25	307	21	16	19	33001
306	20	56	53	33004.25	304	21	38	8	33038.25	308	21	16	43	33000.75
307	20	57	36	33004	305	21	38	38	33037.75	309	21	17	6	33001
308	20	58	6	33004	306	21	39	38	33038.5	BS	21	18	6	33024
309	20	58	38	33004	307	21	40	30	33037.5	310	21	19	3	33001.75
310	20	59	4	33004	308	21	41	2	33035.5	311	21	19	24	33001
311	20	59	28	33004	309	21	41	53	33036	312	21	20	9	33001.75
312	21	0	33	33005	310	21	42	18	33035	313	21	20	35	33002
313	21	1	30	33005	311	21	43	8	33036	314	21	20	56	33002
314	21	1	57	33005	312	21	43	39	33035.75	315	21	21	22	33001.25
315	21	2	28	33005	313	21	44	11	33035.75	316	21	21	45	33002
316	21	2	57	33005	314	21	44	53	33036.5	317	21	22	3	33001.25
317	21	3	22	33005	315	21	45	21	33036.25	318	21	22	45	33001.25
318	21	4	23	33005	316	21	45	52	33036.75	319	21	23	21	33002
319	21	5	7	33006	317	21	46	18	33037	320	21	23	44	33001.75
320	21	5	33	33005	318	21	47	10	33037.5	321	21	24	24	33001
321	21	6	17	33006	319	21	48	2	33038	322	21	25	5	33001.25
322	21	6	41	33006	320	21	48	34	33038	323	21	25	21	33001.5
323	21	7	11	33006	321	21	49	17	33039	324	21	26	51	33001
324	21	7	35	33006	322	21	49	41	33038.5	325	21	27	17	33001.25
325	21	8	19	33007.75	323	21	50	32	33039	326	21	28	2	33001
326	21	9	23	33008	324	21	51	8	33039	327	21	28	44	33001
327	21	9	58	33008	325	21	51	46	33039.75	328	21	29	52	33001.5
328	21	10	26	33008	326	21	52	18	33039.5	329	21	31	11	33002
329	21	10	57	33009	327	21	53	8	33040	330	21	31	39	33001
330	21	11	52	33009	328	21	53	58	33039.75	331	21	32	7	33001.25
331	21	12	45	33009	329	21	54	31	33039.75	332	21	32	49	33001
BS11	21	14	29	33023	330	21	55	30	33039	333	21	33	13	33001.5
332	21	17	20	33010	331	21	55	58	33040	334	21	33	51	33000.75
333	21	18	3	33009.75	332	21	57	42	33040.75	335	21	34	26	33001
334	21	22	24	33009	333	21	58	19	33040	336	21	34	47	33001

335	21	23	26	33010	334	22	58	52	33040.75	337	21	35	6	33001
336	21	24	14	33010	335	22	0	4	33040.25	338	21	35	35	33001
337	21	25	40	33010	336	22	0	43	33040.5	339	21	36	1	33001
338	21	26	23	33011	337	22	1	14	33040	340	21	36	36	33001
339	21	27	4	33012	338	22	1	51	33040	341	21	36	48	33001
340	21	27	49	33012	339	22	2	20	33040	342	21	38	20	33001.25
341	21	28	28	33012	340	22	2	52	33040	343	21	38	55	33001
342	21	29	18	33012	341	22	3	23	33041	344	21	39	28	33001
343	21	30	6	33012	342	22	3	54	33042	345	21	40	58	33001
344	21	30	51	33012	343	22	5	1	33039.25	346	21	41	22	33001.25
345	21	32	4	33011.25	BS12	22	6	44	33040	347	21	41	47	33002
346	21	32	52	33010.5	344	22	8	31	33041.25	348	21	42	14	33001
347	21	33	43	33010	345	22	9	19	33040.5	349	21	42	55	33001
348	21	35	2	33009	346	22	9	38	33040.25	350	21	44	14	33001
349	21	36	14	33008	347	22	10	6	33040.25	351	21	44	55	33001
350	21	37	36	33008	348	22	10	38	33041	352	21	45	57	33000
351	21	39	54	33006	349	22	11	12	33041	353	21	46	32	33000
352	21	41	5	33007	350	22	11	53	33040.25	354	21	47	20	33000
353	21	42	55	33008	351	22	12	33	33040.75	355	21	47	56	32999
354	21	45	55	33008	352	22	13	6	33040.25	BS	21	49	37	33029
355	21	47	6	33007	353	22	13	49	33041.25	356	21	51	35	32997.25
356	21	49	15	33004	354	22	14	46	33041.25	357	21	52	2	32997
357	21	49	37	33003	355	22	15	18	33041	358	21	52	42	32996
BS12	21	49	58	33025	356	22	16	6	33040.25	359	21	53	3	32996
358	21	52	39	33002	357	22	16	47	33040.75	360	21	53	31	32996
359	21	53	12	33002.5	358	22	17	15	33040.75	361	21	54	34	32995
360	21	53	47	33002	359	22	17	45	33040.25	362	21	54	57	32995
361	21	54	9	33002	360	22	18	25	33040.5	363	21	55	23	32994.75
362	21	54	36	33003	361	22	20	8	33040	364	21	55	49	32994
363	21	55	1	33003	362	22	20	10	33040	365	21	56	13	32994
364	21	55	29	33003	363	22	20	49	33040	366	21	56	48	32994.75
365	21	56	5	33003.75	364	22	21	23	33040	367	21	57	16	32994.75
366	21	57	48	33004.5	365	22	21	56	33040	368	21	57	49	32994.25
367	21	57	23	33005	366	22	26	10	33040	369	21	58	11	32994
368	21	57	48	33006	367	22	26	36	33040	370	21	58	51	32994
369	21	58	15	33007	368	22	27	6	33040	371	21	59	29	32993.75
370	21	58	43	33007	369	22	27	43	33039.75	372	21	59	39	32993
371	22	59	51	33007.75	370	22	28	17	33038.75	373	21	59	59	32993
372	22	0	28	33008.5	371	22	29	19	33038.5	374	22	0	0	32993

373	22	1	29	33009.25	372	22	30	1	33038.5	375	22	1	0	32993
374	22	2	27	33010	373	22	30	30	33040	376	22	1	23	32993
375	22	3	46	33011	374	22	31	25	33039	377	22	2	8	32993
376	22	4	32	33012	375	22	32	6	33038	378	22	2	33	32992.75
377	22	5	55	33012	376	22	32	33	33038	379	22	3	2	32992.5
378	22	7	0	33013.75	377	22	33	12	33038	380	22	4	34	32992
379	22	7	48	33015.75	378	22	33	37	33038.5	381	22	5	18	32992
380	22	8	44	33016	379	22	34	24	33039	382	22	5	39	32992
381	22	9	15	33018.25	380	22	34	43	33038	383	22	6	20	32992
382	22	10	18	33019.25	381	22	35	4	33038	384	22	6	59	32991
383	22	10	48	33021	382	22	35	42	33037.75	385	22	7	39	32991
384	22	11	33	33022	383	22	36	2	33037.25	386	22	8	23	32991
385	22	12	9	33024	384	22	36	33	33036.25	387	22	8	45	32991
386	22	13	3	33027.25	385	22	37	17	33036	388	22	9	13	32991
387	22	13	34	33026.75	BS13	22	38	21	33039	389	22	9	38	32990.5
388	22	14	10	33028.75	386	22	40	15	33034.5	390	22	10	15	32989
389	22	15	5	33031.25	387	22	40	47	33035.75	391	22	10	55	32990
390	22	15	32	33032.25	388	22	41	39	33034.75	392	22	11	21	32990
391	22	16	38	33034.5	389	22	42	36	33034	393	22	11	45	32989
392	22	17	28	33035	390	22	42	55	33034	394	22	12	8	32989
393	22	19	17	33043.75	391	22	43	45	33034	395	22	12	38	32989
394	22	20	43	33043.75	392	22	44	39	33033	396	22	13	0	32987.5
395	22	22	11	33047	393	22	45	6	33032.75	397	22	13	21	32987
396	22	22	38	33052.25	394	22	45	53	33031.25	398	22	14	15	32987.25
397	22	23	28	33051.25	395	22	46	37	33031	399	22	14	45	32986
398	22	24	16	33053.25	396	22	47	10	33030.25	400	22	15	7	32986.25
399	22	25	4	33059.75	397	22	47	48	33029.25	401	22	15	57	32984.75
400	22	26	10	33062.5	398	22	48	22	33027.75	402	22	16	35	32987.25
BS13	22	27	54	33028	399	22	49	3	33028.25	403	22	16	57	32984.75
					400	22	50	12	33025.75	404	22	17	39	32983.75
					401	22	50	38	33024.25	405	22	18	5	32985.75
					402	22	51	3	33023	406	22	18	37	32982
					403	22	51	30	33021.75	407	22	19	9	32982.25
					404	22	51	57	33021	408	22	19	57	32981
					405	22	53	9	33021	BS	22	21	29	33035
					406	22	53	47	33019	409	22	23	4	33081
					407	22	54	30	33018	410	22	23	46	33080
					408	22	55	21	33018.75	411	22	24	47	33079.75
					409	22	56	4	33016	412	22	25	41	33080.25

					410	22	56	38	33015	413	22	26	16	33079.75
					411	22	57	3	33014.25	414	22	26	45	33079
					412	22	57	28	33016.25	415	22	27	26	33078.25
					413	22	58	2	33016.25	416	22	28	9	33077
					414	22	58	44	33016	417	22	28	32	33077
					415	22	59	22	33015	418	22	29	28	33074
					416	22	59	49	33015	419	22	30	27	33073.25
					417	23	0	17	33015	420	22	30	59	33070
					418	23	1	11	33017	421	22	33	8	33070
					419	23	1	51	33016.25	422	22	34	2	33069
					420	23	2	39	33015.75	423	22	34	40	33067.25
					421	23	3	11	33015.75	424	22	35	24	33068
					422	23	3	48	33016	425	22	36	42	33068.5
					423	23	4	17	33016	426	22	37	16	33061
					424	23	5	13	33016	427	22	37	52	33061
					425	23	5	48	33017.25	428	22	39	52	33060
					426	23	6	35	33017	429	22	41	12	33057
					427	23	7	13	33017	430	22	41	38	33055.25
					428	23	8	38	33016	431	22	43	14	33052
					429	23	9	46	33016	432	22	45	2	33047.25
					430	23	10	6	33017	433	22	45	30	33040
					BS14	23	11	42	33036	434	22	46	32	33047
					431	23	13	22	33016.75	435	22	47	2	33036.25
					432	23	14	32	33016.5	436	22	47	31	33047
					433	23	15	22	33016.25	437	22	48	0	33035
					434	23	15	49	33015.75	438	22	48	28	33030.75
					435	23	16	25	33016	439	22	49	41	32919.75
					436	23	17	5	33014.25	440	22	50	26	32922
					437	23	17	58	33014.5	441	22	50	55	32913.5
					438	23	19	11	33013	442	22	51	32	32904.5
					439	23	19	42	33012	443	22	52	50	32890.25
					440	23	20	21	33011.25	444	22	53	42	32903.25
					441	23	21	0	33012	445	22	54	32	32900.5
					442	23	21	38	33013	446	22	56	15	32881.75
					443	23	22	30	33011	447	22	57	14	32869.25
					444	23	23	12	33011	448	22	58	5	32870
					445	23	23	34	33008.75	449	22	58	56	32850.25
					446	23	24	31	33005	450	23	1	50	32848.25
					447	23	25	43	33000	BS	23	3	15	33038

					448	23	26	48	32999					
					449	23	27	31	32998					
					450	23	28	30	32998.5					
					451	23	29	44	32994.5					
					452	23	31	6	32991					
					453	23	31	52	32987.25					
					454	23	32	43	32985.75					
					455	23	33	27	32984.5					
					456	23	34	0	32980					
					457	23	36	20	32983					
					458	23	36	52	32977					
					459	23	37	47	32978					
					BS15	23	41	15	33035					
					BS16	24	21	6	33034					
					460	24	23	0	32972					
					461	24	24	33	32969.5					
					462	24	29	14	32969					
					463	24	31	2	32969					
					464	24	34	27	32969					
					465	24	38	7	32970					
					466	24	39	30	32971.5					
					BS17	24	41	29	33030					
					BS18	1	57	52	33022					
					466	1	59	18	32958					
					467	1	59	55	32958.75					
					468	2	0	22	32963					
					469	2	1	3	32969					
					470	2	1	46	32974					
					471	2	2	12	32977					
					472	2	2	45	32978.75					
					473	2	3	11	32983					
					474	2	4	1	32986.75					
					475	2	4	33	32993.25					
					476	2	5	43	32999					
					477	2	6	19	33000					
					478	2	7	0	33003					
					479	2	7	23	33007					
					480	2	8	37	33013					
					481	2	9	4	33015					

					482	2	9	28	33017.75					
					483	2	11	2	33020					
					484	2	11	23	33023					
					485	2	12	9	33024.25					
					486	2	12	58	33024.25					
					487	2	13	27	33024.75					
					488	2	14	3	33023.5					
					489	2	15	3	33026.75					
					490	2	15	25	33025.75					
					491	2	16	19	33027					
					492	2	17	1	33023.75					
					493	2	17	34	33024					
					494	2	18	12	33022					
					495	2	18	56	33022.75					
					496	2	20	2	33022					
					497	2	20	35	33020.25					
					498	2	20	57	33020.25					
					499	2	21	53	33019					
					500	2	22	21	33019					
					501	2	23	29	33017.25					
					502	2	24	0	33017					
					503	2	24	50	33016.5					
					504	2	25	18	33015.75					
					505	2	25	40	33012.75					
					506	2	26	11	33013					
					507	2	26	45	33012.75					
					508	2	27	30	33015					
					509	2	27	49	33010.5					
					510	2	28	17	33010					
					BS19	2	29	14	33024					
					511	2	30	18	33010					
					512	2	30	39	33010					
					513	2	31	9	33009					
					514	2	31	44	33008.25					
					515	2	32	26	33010					
					516	2	33	8	33008.75					
					517	2	33	33	33011					
					518	2	34	9	33036					
					BS20	2	34	59	33023					

					BS21	3	34	44	33022					
					518	3	37	9	33002					
					519	3	37	41	33002.5					
					520	3	38	33	33002					
					521	3	38	54	33001					
					522	3	39	31	33001.25					
					523	3	40	22	33001					
					524	3	41	28	33000					
					525	3	42	11	33001.5					
					526	3	43	18	33001.75					
					527	3	43	40	33000.25					
					528	3	44	33	33000.25					
					529	3	45	35	33000					
					530	3	46	49	32999					
					531	3	47	49	32999.75					
					532	3	48	34	32998.25					
					533	3	49	47	32998					
					534	3	50	26	32997.25					
					535	3	51	16	32995.25					
					536	3	51	34	32994.25					
					537	3	52	4	32994.25					
					538	3	52	32	32994					
					539	3	53	9	32995					
					540	3	53	36	32994.25					
					541	3	53	58	32995					
					542	3	54	34	32994					
					543	3	55	3	32994					
					544	3	55	58	32995					
					545	3	56	31	32994					
					546	3	57	0	32993.5					
					547	3	57	29	32992.25					
					548	3	58	0	32994					
					549	3	58	29	32992					
					550	3	58	50	32992					
					551	3	59	17	32992					
					552	4	0	17	32993					
					553	4	1	27	32994					
					554	4	2	11	32992.75					
					555	4	2	43	32992.75					

					556	4	3	8	32992.25					
					557	4	3	47	32991.5					
					558	4	4	21	32991					
					559	4	4	56	32992					
					BS22	4	6	2	33020					
					560	4	7	34	32991.75					
					561	4	8	17	32990.5					
					562	4	8	58	32990.75					
					563	4	10	41	32990					
					564	4	11	18	32990					
					565	4	11	46	32989					
					566	4	12	15	32988.5					
					567	4	12	48	32988					
					568	4	13	21	32987					
					569	4	13	46	32986					
					570	4	14	18	32986					
					571	4	14	54	32986.5					
					572	4	15	34	32985					
					573	4	16	0	32985					
					574	4	16	30	32984.25					
					575	4	16	52	32984.75					
					576	4	17	24	32985					
					577	4	17	48	32983.75					
					578	4	18	12	32983.75					
					579	4	18	38	32983					
					580	4	18	57	32983					
					581	4	19	22	32982					
					582	4	20	12	32982.75					
					583	4	20	37	32983					
					584	4	21	10	32982					
					585	4	21	30	32981					
					586	4	22	6	32981					
					587	4	22	29	32980.75					
					BS23	4	23	34	33018					
					BS24	4	56	10	33013					
					587	4	57	37	32975.75					
					588	4	58	22	32975.25					
					589	4	59	20	32975					
					590	4	59	49	32974					

					591	5	0	53	32973					
					592	5	1	16	32973					
					593	5	1	36	32972					
					594	5	1	58	32972					
					595	5	2	46	32973					
					596	5	3	7	32972					
					597	5	3	30	32971.5					
					598	5	4	10	32970					
					599	5	4	37	32970					
					600	5	5	7	32969					
					601	5	5	32	32969					
					602	5	5	54	32969					
					603	5	6	38	32970.25					
					604	5	6	57	32969					
					605	5	7	27	32969					
					606	5	7	55	32971.25					
					607	5	8	54	32969.75					
					608	5	9	26	32970.25					
					609	5	10	27	32970					
					610	5	10	48	32970.75					
					611	5	11	13	32969.5					
					612	5	11	43	32968					
					613	5	12	25	32968					
					614	5	12	52	32970					
					615	5	13	24	32971					
					616	5	13	49	32970					
					617	5	14	27	32970					
					618	5	15	9	32970					
					619	5	15	39	32970					
					620	5	16	26	32968					
					621	5	17	17	32968.75					
					622	5	18	8	32972.75					
					623	5	18	46	32972					
					624	5	19	36	32971					
					625	5	20	7	32971					
					626	5	20	44	32971					
					627	5	21	17	32970					
					628	5	21	56	32972.75					
					629	5	23	12	32973					

					630	5	23	33	32973					
					631	5	24	26	32974.75					
					632	5	25	7	32977					
					633	5	25	35	32977					
					634	5	25	57	32977					
					635	5	26	51	32978.75					
					636	5	27	21	32978					
					637	5	28	3	32978					
					638	5	28	38	32981					
					639	5	29	0	32981					
					640	5	29	29	32985					
					641	5	30	8	32985					
					642	5	30	29	32985					
					643	5	31	18	32988					
					644	5	31	55	32988					
					645	5	32	24	32988.25					
					646	5	32	39	32993.75					
					647	5	33	54	32996					
					648	5	35	13	32998.25					
					649	5	35	43	32998					
					650	5	36	21	32999					
					BS25	5	39	0	32912					

APPENDIX B

Appendix B: GPR Radargrams

Location 1: 450 MHz

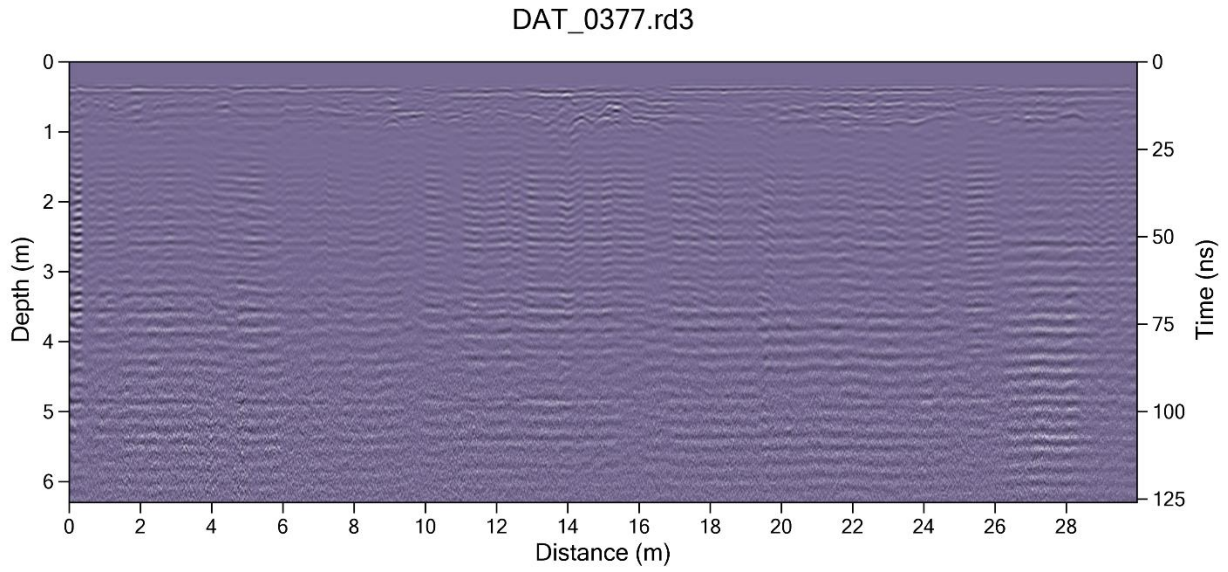


Figure B1: GPR radargram using the 450 MHz antenna along traverse 1

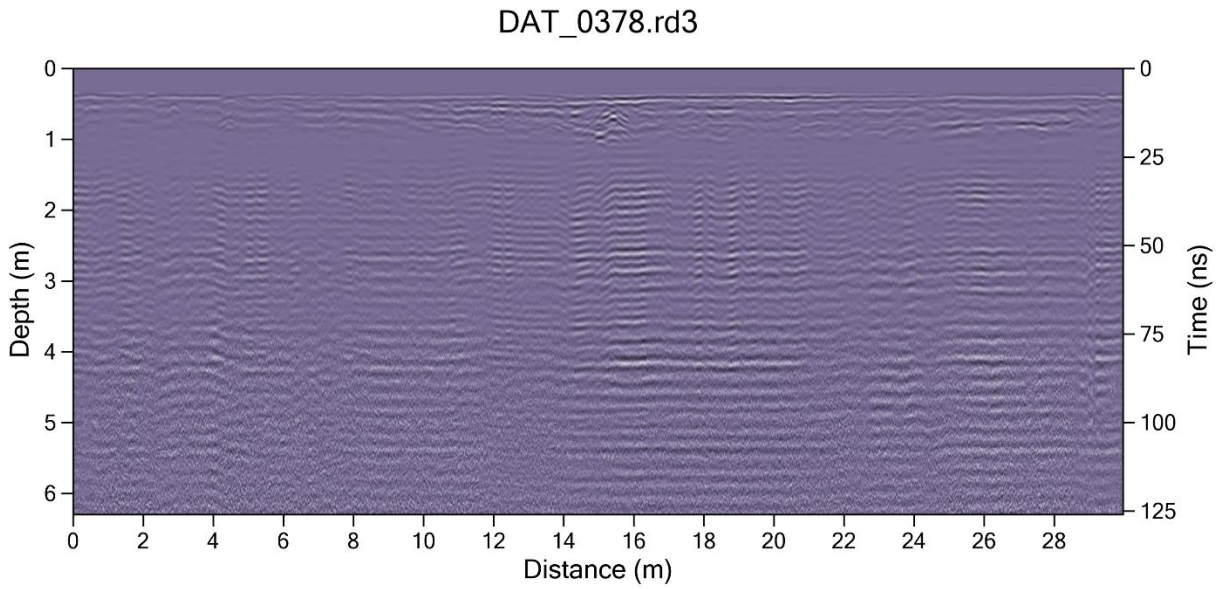


Figure B2: GPR radargram using the 450 MHz antenna along traverse 2

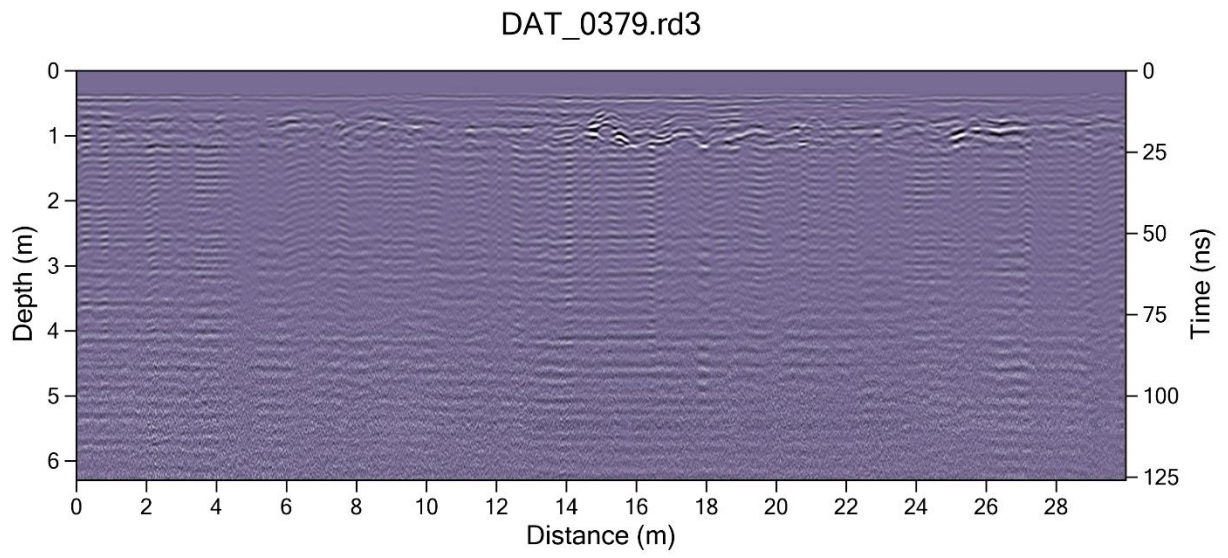


Figure B3: GPR radargram using the 450 MHz antenna along traverse 3

Location 2: 450MHz

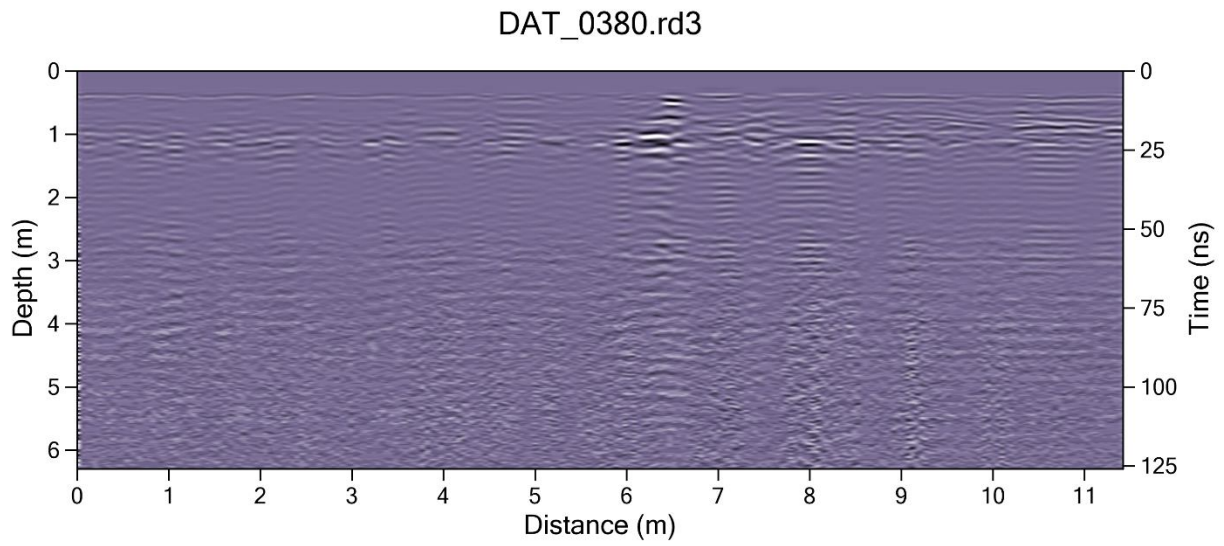


Figure B4: GPR radargram using the 450 MHz antenna along traverse 1

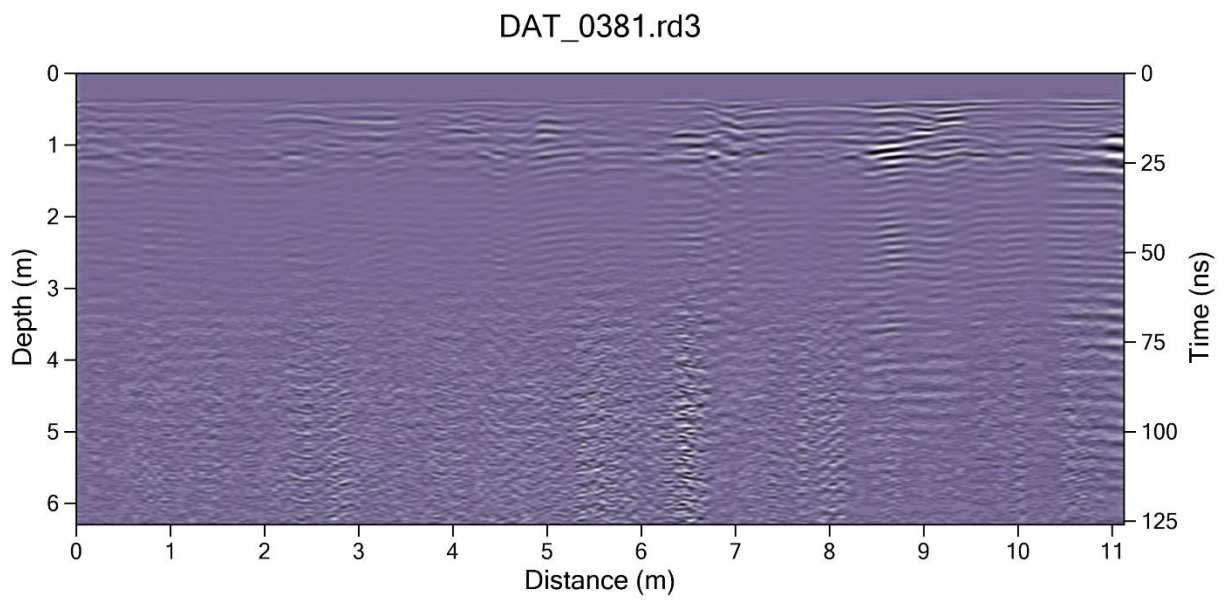


Figure B5: GPR radargram using the 450 MHz antenna along traverse 2

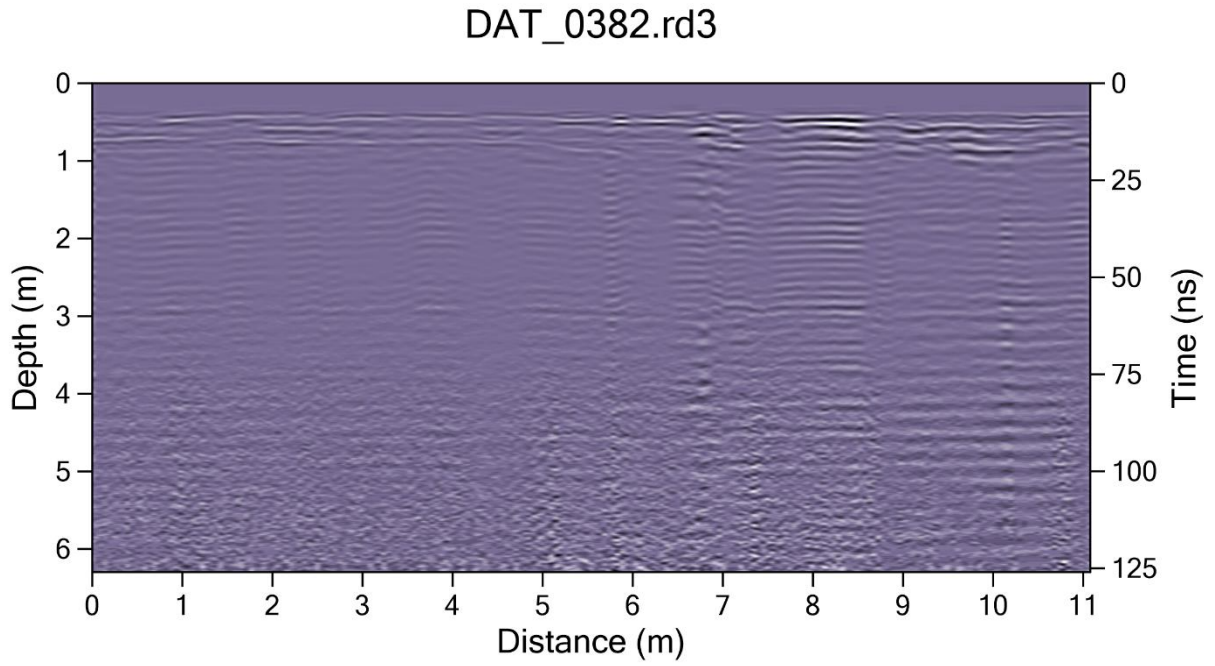


Figure B6: GPR radargram using the 450 MHz antenna along traverse 3

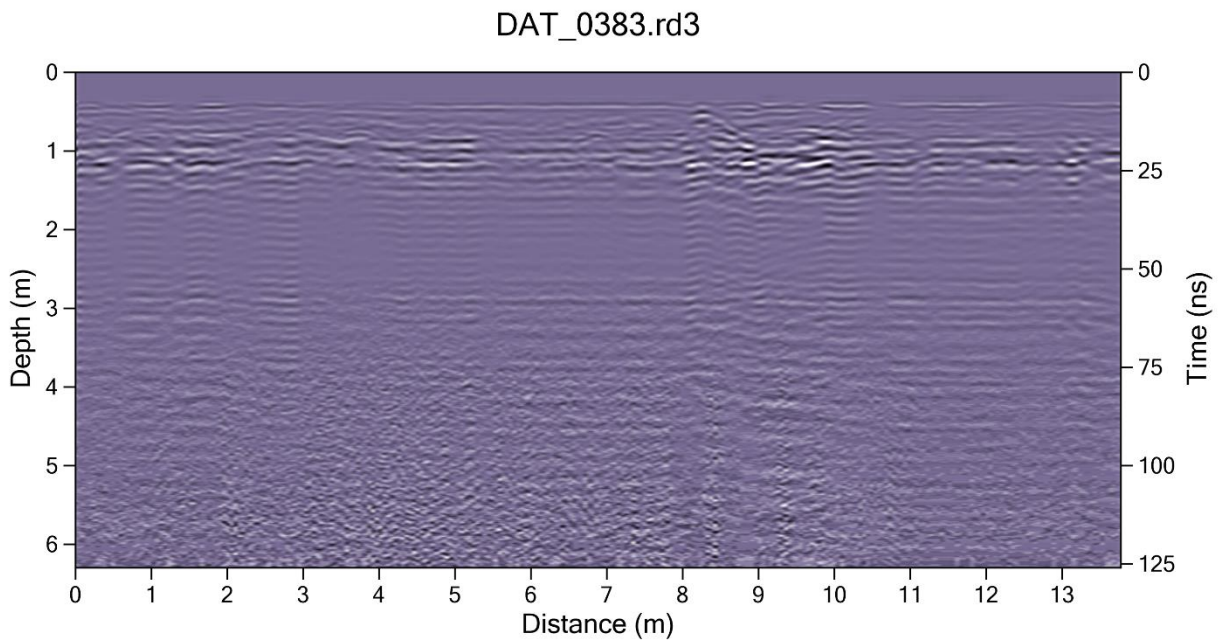


Figure B7: GPR radargram using the 450 MHz antenna along traverse 4

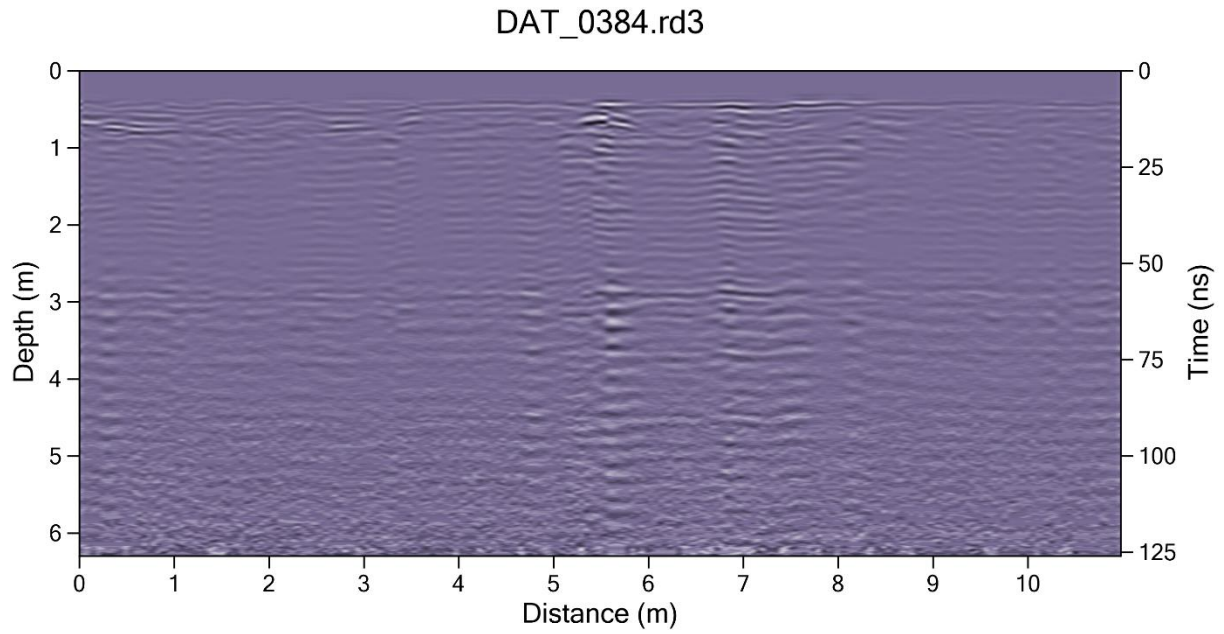


Figure B8: GPR radargram using the 450 MHz antenna along traverse 5

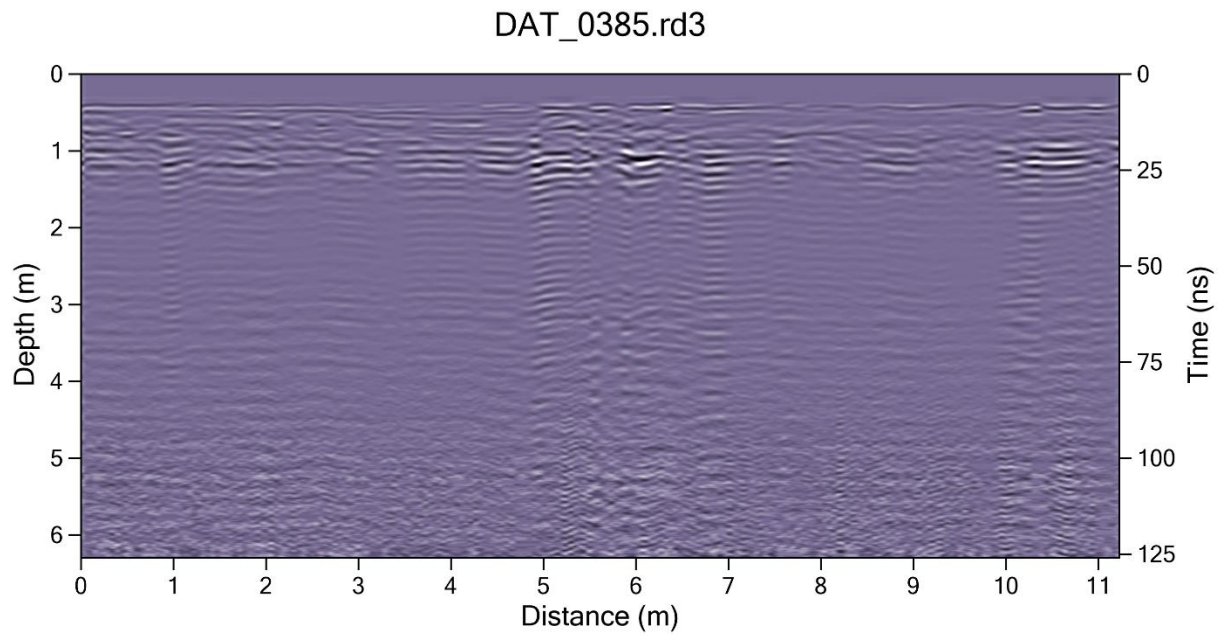


Figure B9: GPR radargram using the 450 MHz antenna along traverse 6

Location 3: 450MHz

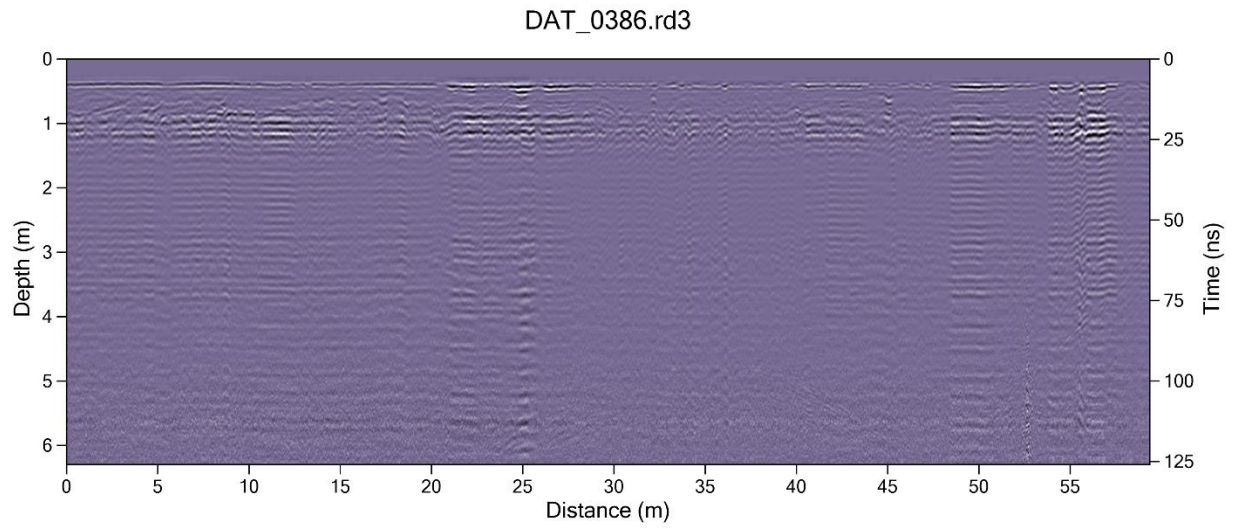


Figure B10: GPR radargram using the 450 MHz antenna along traverse 1

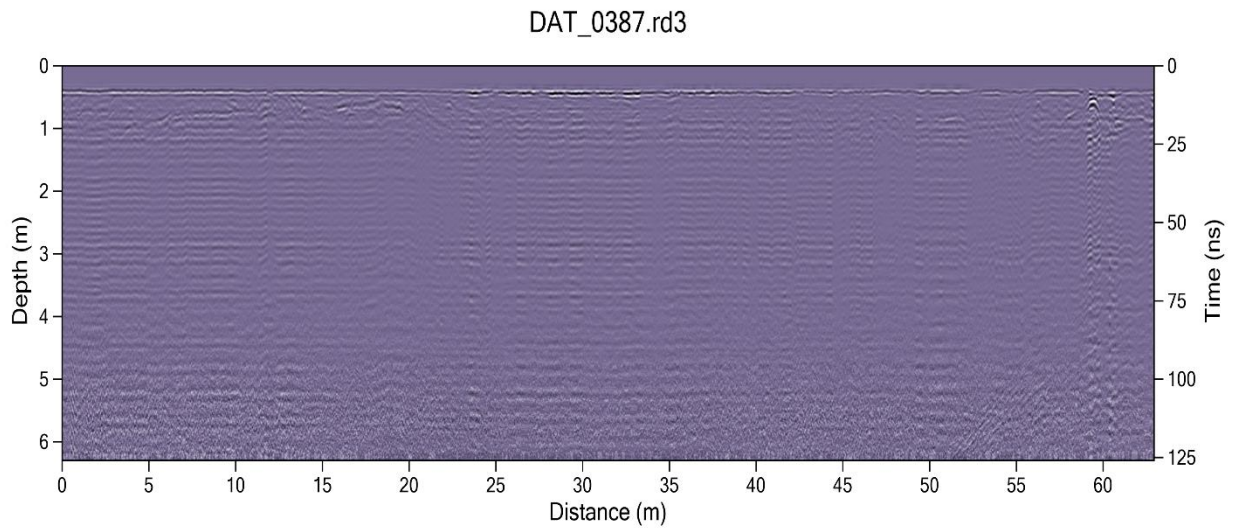


Figure B11: GPR radargram using the 450 MHz antenna along traverse 2

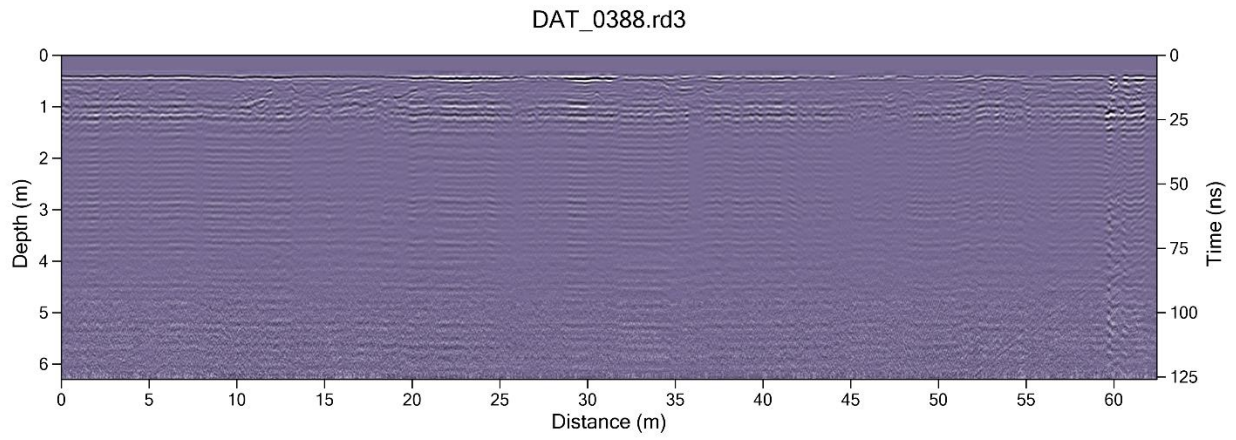


Figure B12: GPR radargram using the 450 MHz antenna along traverse 3

Location 1: 750MHz

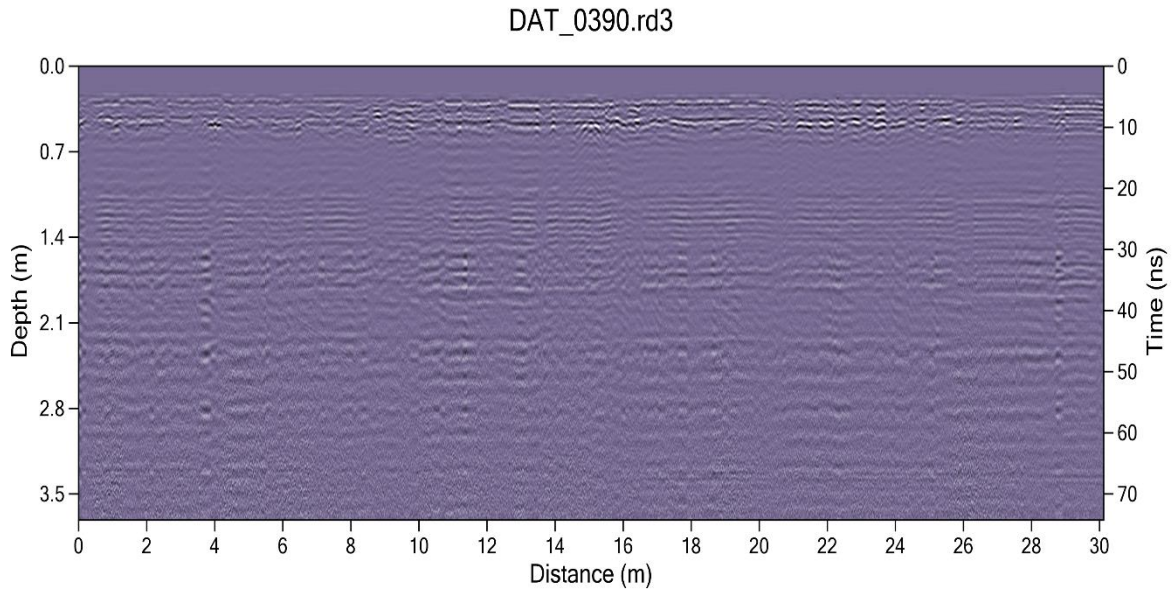


Figure B13: GPR radargram using the 750 MHz antenna along traverse 1

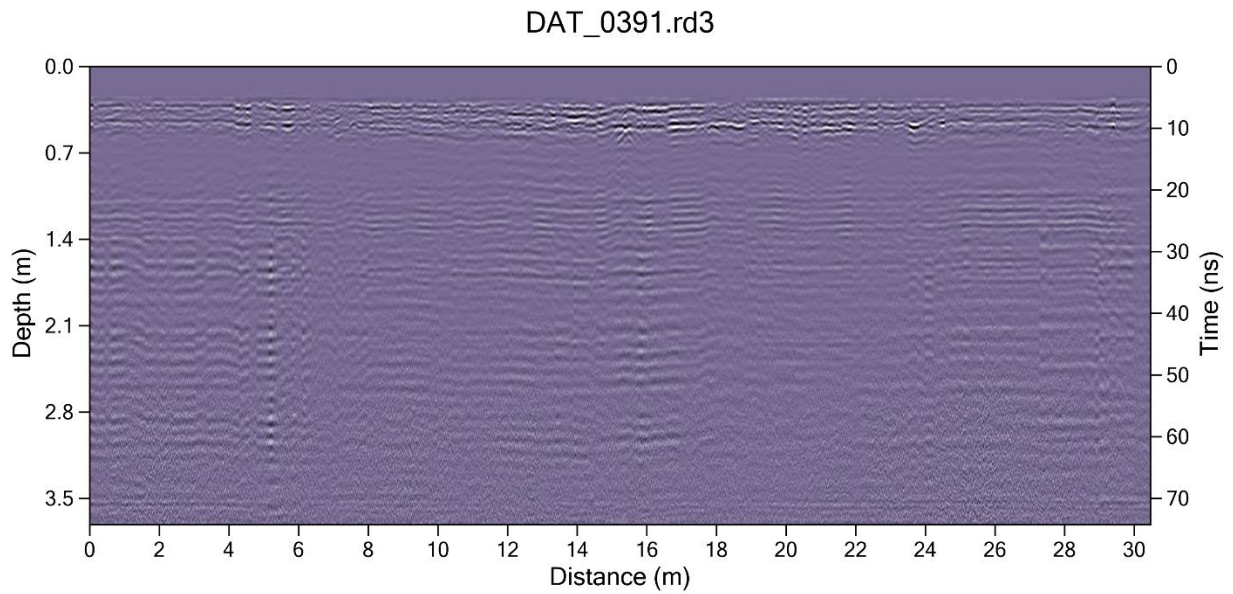


Figure B14: GPR radargram using the 750 MHz antenna along traverse 2

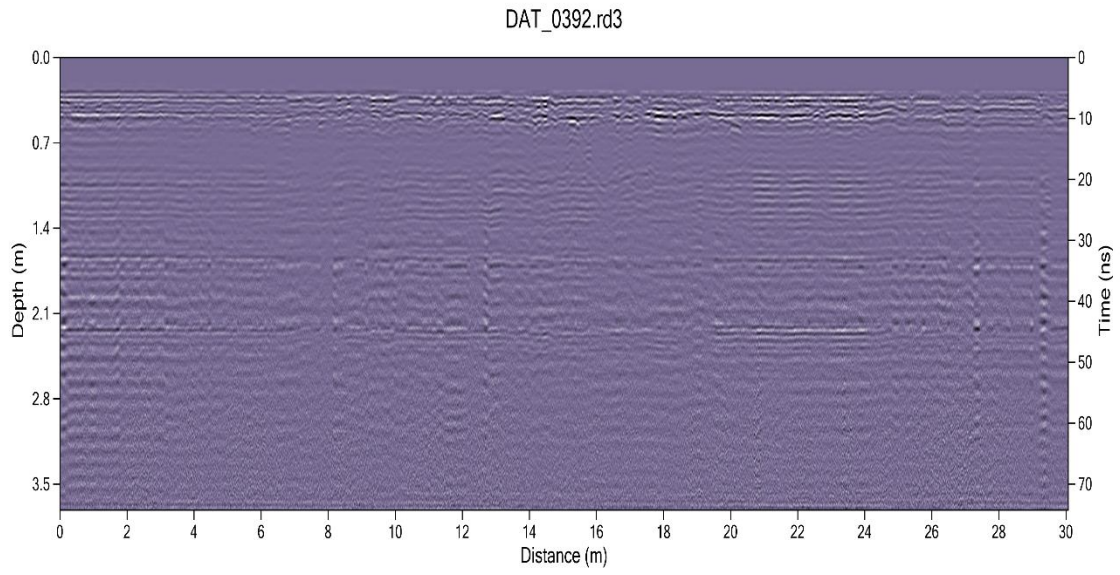


Figure B15: GPR radargram using the 750 MHz antenna along traverse 3

Location 2: 750MHz

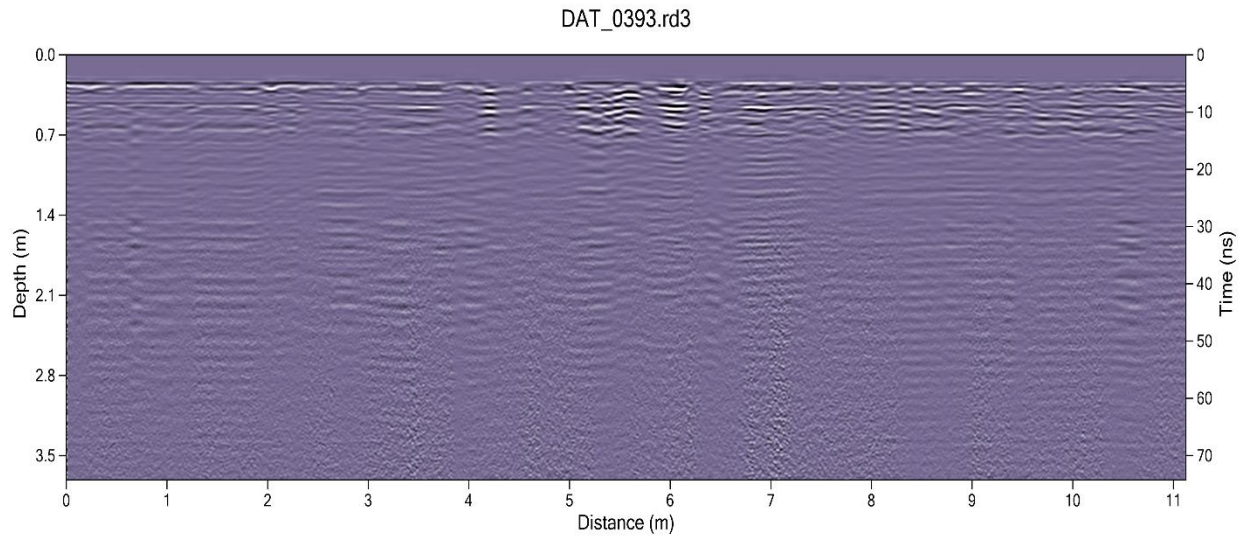


Figure B16: GPR radargram using the 750 MHz antenna along traverse 1

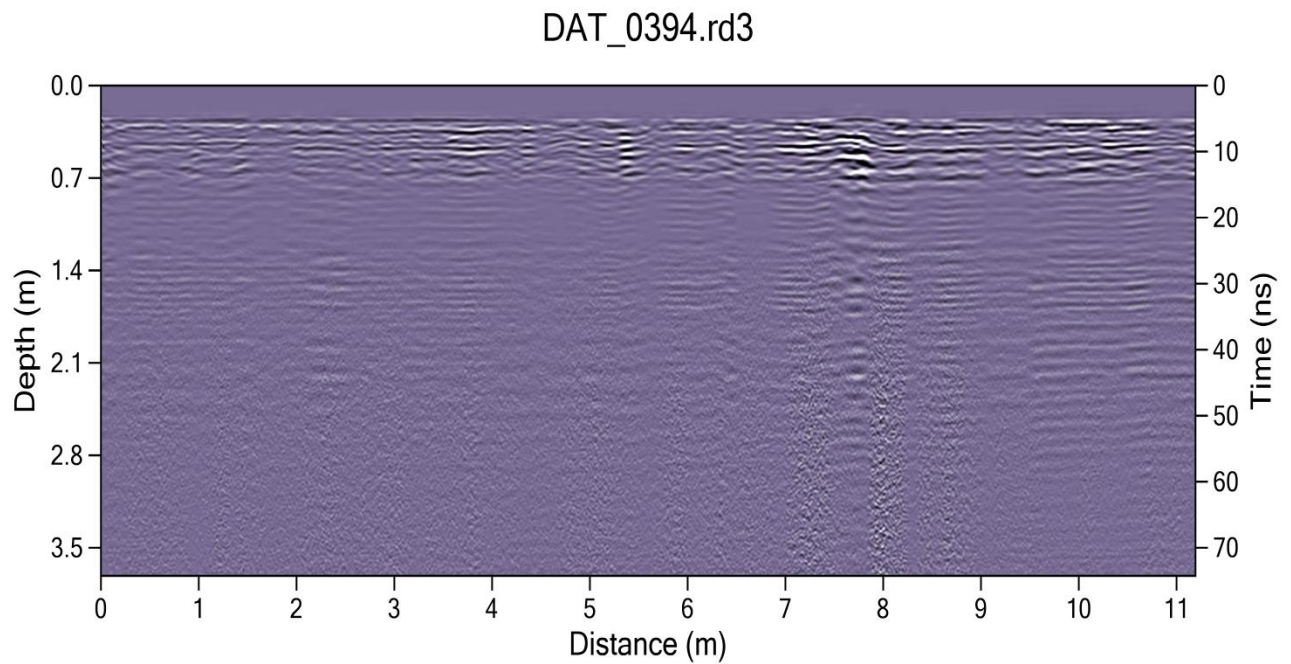


Figure B17: GPR radargram using the 750 MHz antenna along traverse 2

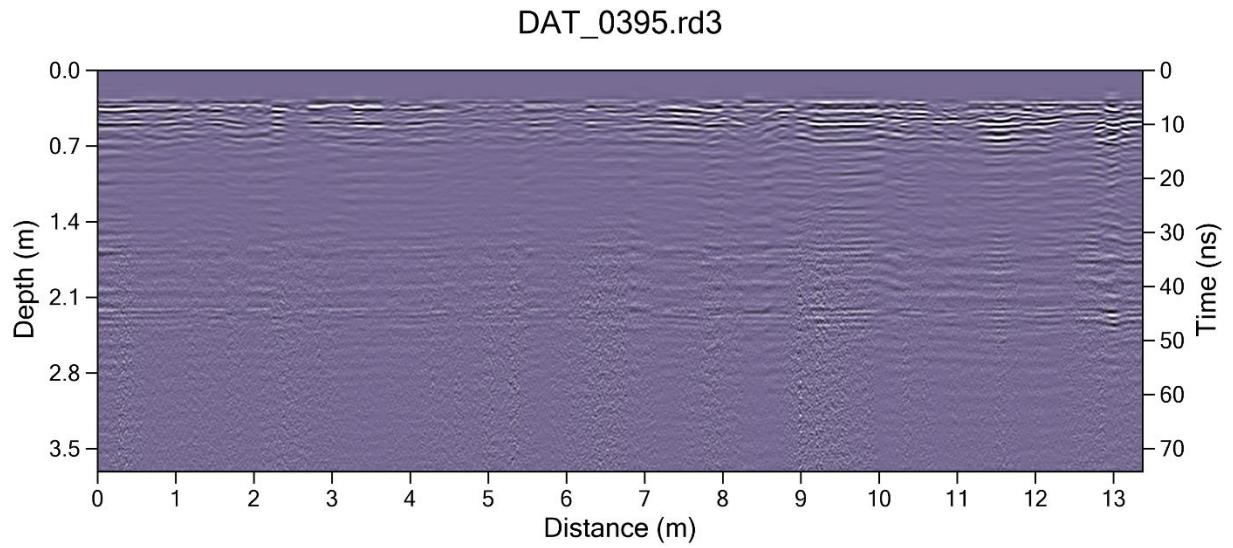


Figure B18: GPR radargram using the 750 MHz antenna along traverse 3

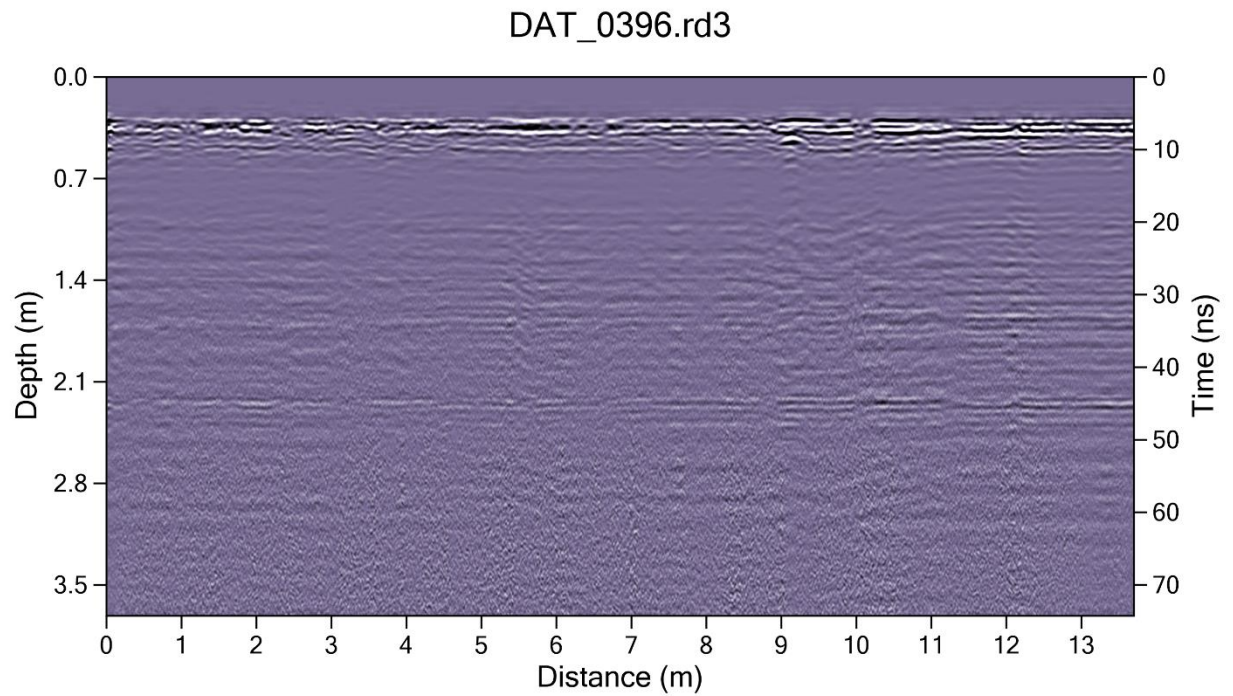


Figure B19: GPR radargram using the 750 MHz antenna along traverse 4

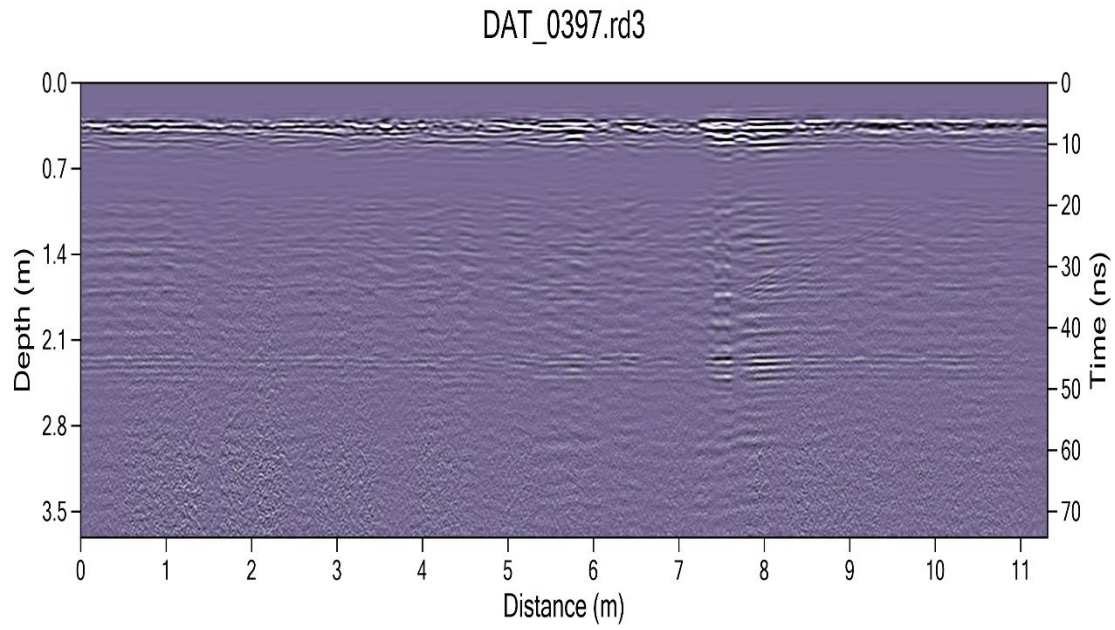


Figure B20: GPR radargram using the 750 MHz antenna along traverse 5

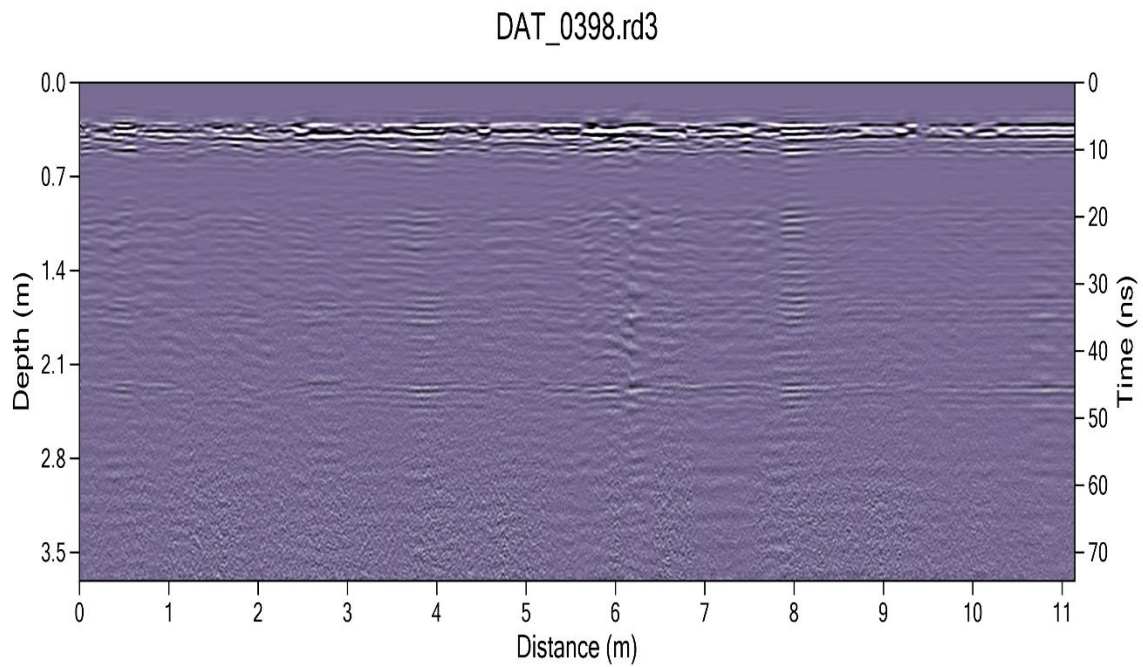


Figure B21: GPR radargram using the 750 MHz antenna along traverse 6

Location 3: 750MHz

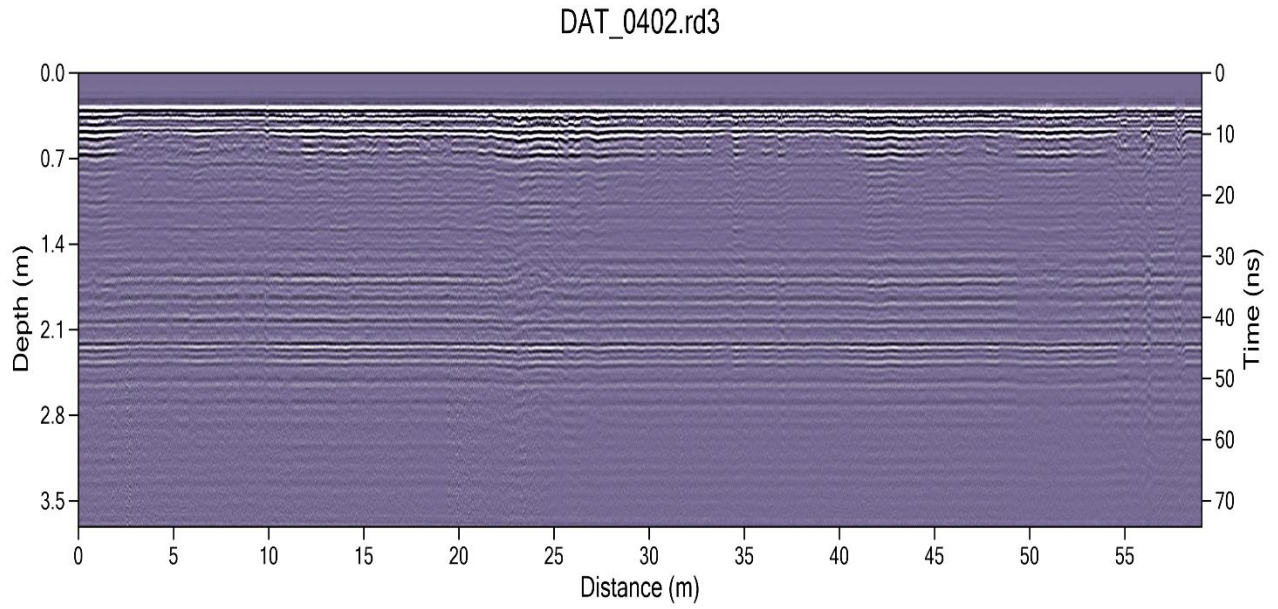


Figure B22: GPR radargram using the 750 MHz antenna along traverse 1

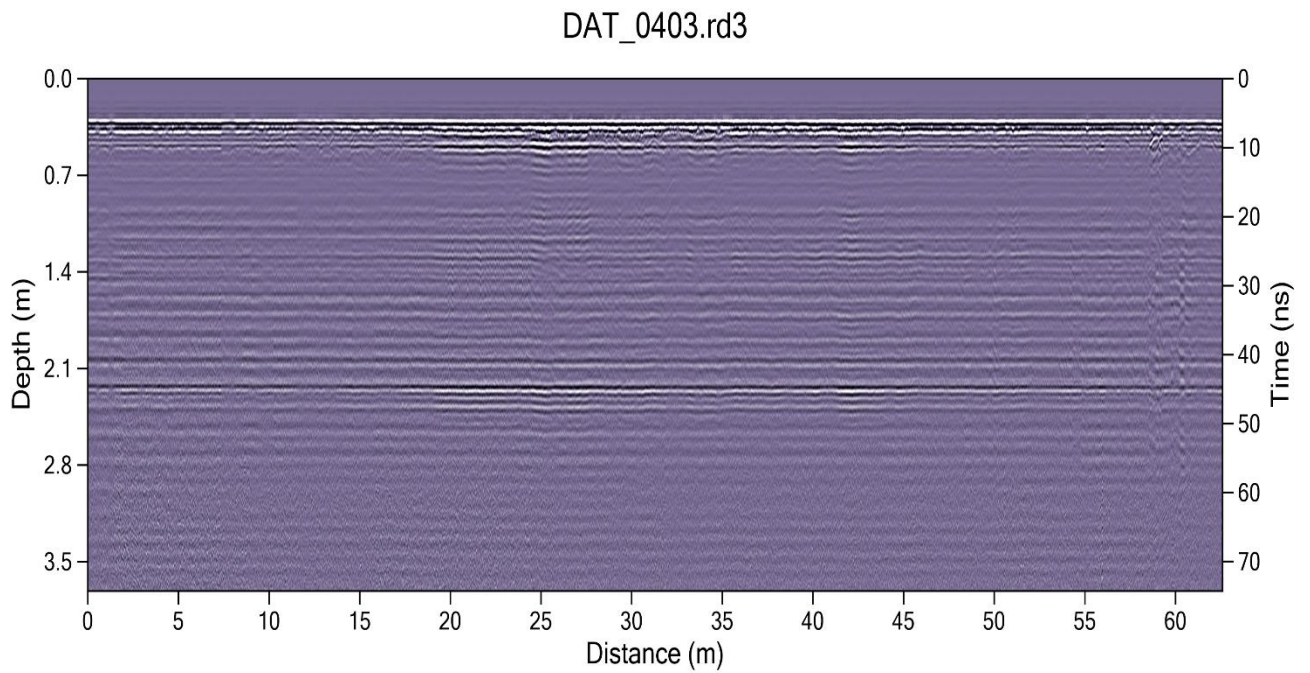


Figure B23: GPR radargram using the 750 MHz antenna along traverse 2

DAT_0404.rd3

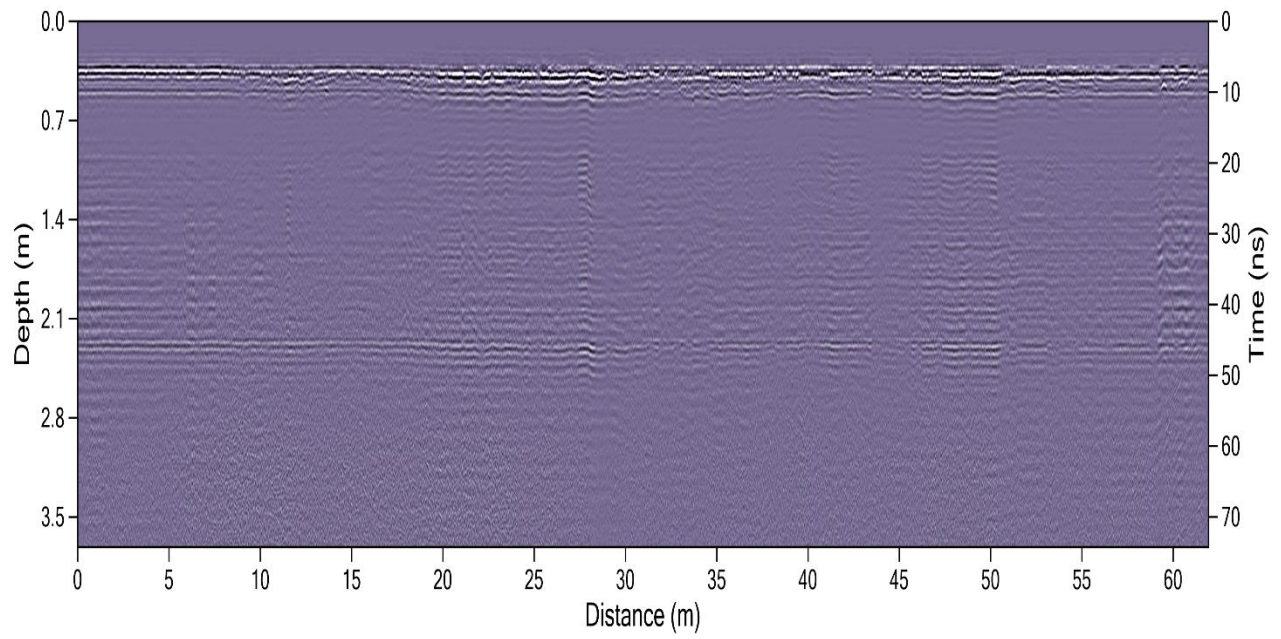


Figure B24: GPR radargram using the 750 MHz antenna along traverse 3